Effects of Photosensitizer Bleaching and Localization on

Photodynamic Oxygen Consumption and Dosimetry

by

Irene Georgakoudi

Submitted in Partial Fulfillment

of the

Requirements for the Degree

Doctor of Philosophy

Supervised by

Professor Thomas H. Foster

Department of Biochemistry & Biophysics

Biophysics Training Program

School of Medicine & Dentistry

University of Rochester

Rochester, New York

1998

To my parents,

Niki and Christos

Curriculum Vitae

Irene Georgakoudi was born in Thessaloniki, Greece on June 7, 1971. In 1983 she earned a full scholarship to attend Anatolia College, a private secondary school with trustees from the U.S.A. There, she took her first courses in science and mathematics and was encouraged to continue her studies in the U.S.A.

In 1989, she enrolled at Dartmouth College in Hanover, New Hampshire. She was fortunate to have Professor Michael Sturge as a freshman advisor. With his help and guidance she pursued her studies with a concentration in physics. By sophomore year, she was already getting her hands dirty in Professor Sturge's laboratory. During her junior year she was selected as a Presidential Scholar and was awarded a research assistantship. As a senior, she completed an honors thesis, "Development of a Short Pulse Commercial Diode Laser", under the supervision of Professor Sturge. She graduated in June 1993, *Magna cum Laude*, and she was awarded the Francis W. Sears Prize by the Department of Physics and Astronomy.

In September of 1993, she embarked on her graduate studies at the Biophysics Training Program of the University of Rochester. Early on, she expressed a keen interest in conducting research in Professor Tom Foster's laboratory in the field of photodynamic therapy. Research in this area led to her formal doctoral thesis work under the supervision of Dr. Foster and as part of a talented and stimulating research team.

In 1994, Irene received a Leonidas Lantzounis grant by the Hellenic Medical Society of New York. In February 1996 she earned the Master of Science in Biophysics

degree. In September 1996, she was awarded the Graduate Alumni Fellowship by the School of Medicine and Dentistry at the University of Rochester. During her last full year, she was privileged to receive the Agnes M. and George Messersmith Fellowship of the University of Rochester. The William F. Neuman Award in Biophysics was given to Irene in May 1998.

Aside from her scientific pursuits, she was actively involved in the Graduate Student Society of the University of Rochester from 1994 until 1997 and served as its President during the 1996-1997 academic year. For her participation in this society she was awarded the Graduate Student Society Leadership Award in May 1997.

As a graduate student, Irene had four papers published and presented her scientific work at meetings in the U.S.A. and in Europe. She is currently a member of the American Society for Photobiology and the Optical Society of America.

Acknowledgements

This thesis could not have been completed without the guidance and assistance of several people. The advice, enthusiasm, and patience of my advisor, Dr. Tom Foster, helped me grow as a scientist. As part of his team, I was exposed to a very stimulating environment. I certainly appreciate the amount of time and effort he devoted to help me meet the challenges I faced during the last five years. Of course, his essential lessons on scientific writing will continue to serve me well.

Most of my project was based on work performed by Mike Nichols, who introduced me to the world of oxygen microelectrodes, the C programming language and Unix. His assistance in helping me begin was vital. I was very fortunate to share office and lab space with Ed Hull over the last three years. Ed was a great resource for discussing all sorts of theoretical and experimental issues, and he always seemed to have the time to offer practical advice. In addition, Ed and I could always stir up good theological discussions, and that was great since most of my research required lots of faith. John Larkin was another great sounding board and offered numerous suggestions for solving problems. During the last few months, Eric Page and Soumya Mitra helped me significantly with the confocal microscope experiments. Eric was also involved in the co-localization studies that we did with EtNBS and the microspheres. Andrey Mezhiba is gratefully acknowledged for writing the Labview code used for operating the confocal microscope. Dave Conover also contributed to this effort. His machining skills, particularly during the construction of the confocal microscope, are greatly appreciated.

As part of Dr. Foster's lab, I had the opportunity to work with several other

investigators in the Medical Center. Dr. Russell Hilf and Mr. Scott Gibson were helpful resources for issues regarding PpIX. Mr. Gibson and Ms. Mylien Nguyen taught me how to use the spectrofluorimeter, while Mr. Jim Havens and Ms. Donna Hartley are gratefully acknowledged for maintaining our tissue cultures. Dr. William Hwang constructed the glass pipettes used for the microelectrode experiments. Dr. Peter Keng and Ms. Regina Harley had significant input in the hypoxia PpIX studies. They taught me about flow cytometry and the intricacies of obtaining cell populations of different growth rates. The hypoxic ALA incubations were performed in Dr. John Ludlow's laboratory. Dr. Nancy Krucher was extremely helpful during the time I spent in that laboratory. Dr. Philip Fay was very kind to lend me a microcell used to perform the PpIX fluorescence spectroscopy measurements. Curtis Harkrider from the Institute of Optics contributed his time and knowledge during the last few months with issues related to the optical design of the confocal microscope. Dr. Louis Cincotta from the Rowland Science Institute generously provided the Nile Blue compounds, and was a great person to talk to regarding Nile Blue localization. Dr. Milind Rajadhyaksha's advice from the Wellman Laboratories was instrumental in the design of the confocal microscope. My thesis committee members have provided valuable insights concerning the paths that my research should follow. Dr. Paul LaCelle and Dr. Rick Waugh have been great mentors.

Finally, I would like to thank my husband, Jim St. John, for the numerous hours he spent proof reading my papers and this thesis and for his support and encouragement during the last nine years.

Abstract

During photodynamic therapy, tumor eradication is achieved by a series of photochemical reactions resulting from the optical excitation of a photosensitive drug (sensitizer) that localizes preferentially in the tumor. The processes of sensitizer photobleaching and localization are investigated in the context of photodynamic therapy and dosimetry.

Theoretical models describing singlet oxygen ($^1O_2$)- and non-$^1O_2$-mediated sensitizer degradation are developed and used for the analysis of ground state oxygen ($^3O_2$) consumption measurements obtained during irradiation of multicell tumor spheroids sensitized with four different drugs: Photofrin®, δ-aminolevulinic acid-induced protoporphyrin IX (PpIX), Nile Blue Sulfur (EtNBS) and Nile Blue Selenium (EtNBSe). We find that while Photofrin® and PpIX photobleach *via* a $^1O_2$-mediated mechanism, EtNBS and EtNBSe are degraded *via* a non-$^1O_2$-mediated process. We demonstrate that incorporation of sensitizer photobleaching in photodynamic dosimetry models is essential, as it affects significantly the production of $^1O_2$. The spatial and temporal progression of $^1O_2$- and non-$^1O_2$-mediated sensitizer degradation occur in distinct ways, influencing the deposition of $^1O_2$ accordingly.

The relationship between sensitizer localization and photodynamic dosimetry is examined on the subcellular level for EtNBS and EtNBSe and on the cellular level for PpIX. Specifically, we present experimental evidence that demonstrates how the subcellular localization and redistribution of EtNBS and EtNBSe might affect $^3O_2$ consumption during irradiation of sensitized spheroids. Our data suggest that sensitizer

redistribution is a fluence dependent event that leads to enhanced photodynamic oxygen consumption.

Studies of the dependence of PpIX synthesis on $^3O_2$ availability in monolayer cultures indicate that hypoxia leads to significant reductions in PpIX production in a manner that is dependent on the cell density and the proliferation status of the population. These results suggest that PpIX could be synthesized in a non-uniform manner in tumors with significant $^3O_2$ gradients, impairing even further the efficacy of PDT in hypoxic regions.

Finally, we present the design and resolution capabilities of a laser beam scanning confocal microscope constructed for the direct study of sensitizer photobleaching and localization during PDT of tumor spheroids. Preliminary images of optical sections through sensitized spheroids demonstrate the feasibility of such studies.

Table of Contents

List of Tables

List of Figures

List of Symbols

D_d = Diffusion coefficient of oxygen in the medium;

D_s = Diffusion coefficient of oxygen in the spheroid;

R_s = Spheroid radius;

R_d = Radius of the oxygen depletion zone, exterior to the spheroid;

Γ = $\Gamma_{met} + \Gamma_{PDT}$;

Γ_{met} = Rate of metabolic oxygen consumption;

Γ_{PDT} = Rate of photodynamic oxygen consumption;

Γ_0 = Maximum rate of photodynamic oxygen consumption;

S_Δ = Fraction of the triplet quenching collisions between ground state oxygen and triplet state sensitizer molecules that results in singlet oxygen formation;

φ_t = Sensitizer triplet yield;

I_a = Rate of photon absorption by the sensitizer;

k_p = Monomolecular decay rate of excited sensitizer triplets to their ground state;

k_{ot} = Bimolecular rate of triplet sensitizer quenching by ground state oxygen;

k_d = Monomolecular decay rate of singlet oxygen to ground state;

D = Fluence ($J\ cm^{-2}$);

α = Constant photobleaching coefficient for simple exponential decay description of photobleaching ($J^{-1}\ cm^2$);

k_m = Sum of the monomolecular radiative and nonradiative decay rates from S_1 to S_0;

k_{isc} = Sensitizer intersystem crossing rate;

k_{as} = Bimolecular rate constant for reaction between cell substrate A and excited singlet sensitizer S;

k_{at} = Bimolecular rate constant for reaction between cell substrate A and excited triplet sensitizer T;

k_{oa} = Bimolecular rate constant for reaction between singlet oxygen and cell substrate A;

k_{os} = Bimolecular rate constant for singlet oxygen reaction with ground state sensitizer;

k_{50} = Oxygen concentration at which Γ_{met} acquires its half-maximum value;

C = Scaling factor describing the relative magnitude of the second $^3O_2$ consumption step;

LIST OF SYMBOLS

t_i = Time at which the second $^3O_2$ consumption phase begins;

t_{50} = Time at which Γ_0 achieves a value half way between the maximum rate of photodynamic $^3O_2$ consumption during the first phase of $^3O_2$ consumption and its final value;

n = Parameter that describes how fast Γ_0 changes during second step of $^3O_2$ consumption;

θ = Constant characteristic of the rate at which EtNBS fluorescence decreases with radial distance from the spheroid edge;

υ_p = Normalized pinhole radius;

λ = Wavelength;

NA = Numerical aperture;

M = Magnification;

List of Abbreviations

ALA   =   δ-aminolevulinic acid;

BME   =   Eagle's basal medium;

CCD   =   Charge coupled device;

CPU   =   Central processing unit;

EtNBA   =   5-ethylamino-9-diethyl-aminobenzo[a]phenoxazinium chloride;

          =   Nile Blue A;

EtNBS   =   5-ethylamino-9-diethyl-aminobenzo[a]phenothiazinium chloride;

          =   Nile Blue Sulfur;

EtNBSe   =   5-ethylamino-9-diethyl-aminobenzo[a]phenoselenazinium

                  chloride;

          =   Nile Blue Selenium;

FBS   =   Fetal bovine serum;

FCS   =   Fetal calf serum;

LIST OF ABBREVIATIONS

FFT	=	Fast fourrier transform
FOV	=	Field of view;
FWHM	=	Full width at half maximum;
HBSS	=	Hank's balanced salt solution;
HpD	=	Hematoporphyrin derivative;
MEM	=	Minimal essential medium;
mTHPC	=	meso-tetra-hydroxyphenyl-chlorin;
NA	=	Numerical aperture;
PC	=	Personal computer;
PDT	=	Photodynamic therapy;
PMT	=	Photomultiplier tube;
PpIX	=	Protoporphyrin IX;
SD	=	Standard deviation;
SEM	=	Standard error of the mean;
$TPPS_4$	=	tetra(4-sulfonatophenyl)porphine;

Chapter 1

Introduction and Overview

1.1   Photodynamic therapy: basic principles and mechanisms of tumor destruction

Photodynamic therapy (PDT) of cancer combines the use of photosensitive drugs that accumulate preferentially in the tumor and irradiation with visible or near-infrared light. Double selectivity for eradicating only the tumor area is conferred by the preferential localization of the sensitizer and the light to the treatment area. Photofrin®, a porphyrin-like sensitizer, has been approved in the U.S.A. as a PDT drug for the treatment of late stage esophageal cancer (1995) and early stage lung cancer (1998). The same drug has been approved in Canada for the treatment of recurrent bladder cancer, in Japan for early stage lung, esophageal, gastric, and cervical cancers as well as cervical dysplasia, in the Netherlands and France for advanced esophageal and lung cancers and in Germany for

early stage lung cancer. These approvals have inspired a considerable amount of enthusiasm in the field, and there are a significant number of clinical trials around the world testing the efficacy of PDT with several new photosensitizers as a primary or an adjuvant therapy for the treatment of a variety of cancers (1), as well as for conditions such as actinic keratosis (2) and macular degeneration (3-5).

Singlet oxygen ($^1O_2$) is considered to be the main cytotoxic species generated during PDT (6-8). The photochemical reactions that lead to its production are depicted as an energy level diagram in Figure 1.1. A dye molecule in the ground state, S_o, is excited to its first singlet state, S_1, upon light irradiation, typically with a laser. PDT drugs have high intersystem crossing rates, and a large fraction of the excited molecules evolve to their triplet state, T_1. Singlet oxygen is one possible outcome of the collision between a ground state oxygen molecule ($^3O_2$) and a triplet state dye molecule. Finally, $^1O_2$ participates in reactions with a variety of cell substrates that ultimately lead to cell death. Hypoxic tumor regions are protected from direct cell death during PDT, since the production of $^1O_2$ will be limited by the availability of $^3O_2$.

A variety of processes are induced during therapy that are believed to affect the outcome of the treatment. While most studies have focused on tumor necrosis, recent studies have shown that an apoptotic cell death pathway is induced also during PDT with certain photosensitizers (9-11). A variety of immune responses are triggered as a result of the treatment as well, possibly affecting the selectivity and long term cures of the therapy (12, 13). Direct tumor cell death and collapse of the tumor and surrounding
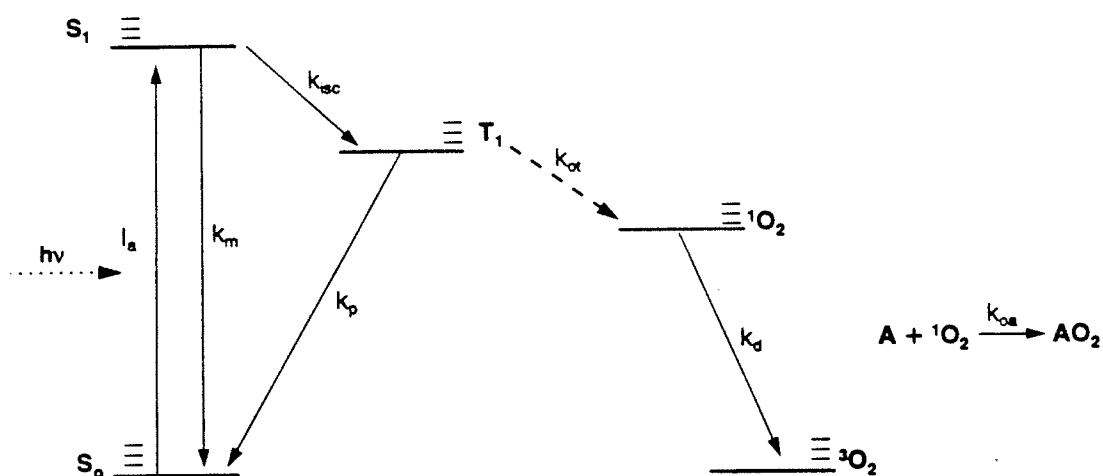
Figure 1.1: Energy level diagram for type II photooxidation reactions occurring during PDT. Upon absorption of the incident light (hv), a sensitizer molecule in its ground state, S_0, is excited to its first singlet state, S_1 (I_a refers to the rate of photon absorption). The excited singlet sensitizer molecule can either decay back to its ground state *via* radiative or non-radiative processes at a rate k_m, or it can be converted to an excited triplet *via* intersystem crossing at a rate k_{isc}. The excited sensitizer molecule at the triplet state, T_1, can either decay to the ground state at a rate k_p or it can be quenched by a ground state oxygen molecule, $^3O_2$, with a bimolecular rate of reaction k_{ot}. The products of this collision are a ground state sensitizer molecule and a singlet oxygen molecule, $^1O_2$. Singlet oxygen can either decay to its ground state at a rate k_d or it can participate in cytotoxic reactions with a variety of cell substrates, denoted collectively as A, at a rate k_{oa}.

healthy tissue vasculature are the main effectors of tumor necrosis. The role each one of these two processes plays on PDT efficacy depends on the sensitizer used and the treatment protocol. With Photofrin®, it was initially thought that vascular damage was the most significant determinant of the therapy's outcome. Histology and fluorescein angiography studies by Henderson *et al.* (14) and Henderson and Fingar (15), using two experimental mouse tumors, showed gross hemorrhage and complete vascular collapse very soon after the commencement of light delivery. Eighty-one percent tumor cure rates were achieved even when only 46.5% of the tumor cells were rendered hypoxic (16). Since these hypoxic cells would be protected from the lethal effects of $^1O_2$, one cannot explain the high tumor cure rates on the basis of direct cell death. Rather, these data suggest that the oxygen and nutrient deprivation resulting from the occlusion of the vessels resulted in tumor cell kill.

However, work by other groups argues that direct cellular effects are related more fundamentally to the treatment's toxicity. The activities of the mitochondrial cytochrome c oxidase and proton-ATPase are inhibited significantly by photodynamic treatment with hematoporphyrin derivative (HpD), a cruder mixture of porphyrins than Photofrin® (8, 17-19). Additionally, ^{31}P-NMR spectroscopy studies demonstrated that damage to the proton-ATPase during PDT *in situ* occurs at an earlier time than changes in the tumor vasculature as observed by ^2H-NMR studies of D_2O uptake (20). The importance of direct cellular effects as opposed to vascular effects has been demonstrated also in studies of the dependence of PDT efficacy on fluence rate. During PDT, a transient type of hypoxia is

induced as a result of photodynamic $^3O_2$ consumption (21-24). This process limits the

tumor regions that have access to enough $^3O_2$ for the production of cytotoxic quantities

of $^1O_2$ to increasingly smaller areas around the capillaries as the fluence rate of irradiation

(light power per unit area) increases (23). Therefore, we expect a larger tumor fraction

to be protected from direct cell damage effects mediated by $^1O_2$ and diminished tumor

cure rates at higher fluence rates than at lower fluence rates of light delivery. Indeed,

protocols with lower fluence rates and/or fractionated irradiations led to considerably

improved treatment outcomes for different types of tumors using a number of different

sensitizers, including Photofrin, 5-ethylamino-9-diethyl-aminobenzo[a]phenothiazinium

chloride (EtNBS) and δ-aminolevulinic acid (ALA)-induced protoporphyrin IX (PpIX)

(22, 25-27). In a recent study, it was shown directly that lower fluence rates corresponded

to higher median tumor oxygen tension values and an improved PDT response with

Photofrin® (28). The photodynamic dosimetry models that we have developed are based

on the assumption that direct tumor cell death mediated by $^1O_2$ is the primary determinant

of the therapy's outcome.

1.2 Dosimetry in photodynamic therapy

1.2.1 Fundamental concepts and considerations

Most photodynamic dosimetry models are founded on the concept of the threshold dose

of $^1O_2$. This threshold dose refers to the minimum cytotoxic concentration of $^1O_2$. In other

words, cells receiving concentrations of $^1O_2$ equal to or higher than the threshold dose will

be damaged irreparably by the therapy, while those receiving less $^1O_2$ than the threshold

dose will be able to survive treatment. The existence of a threshold dose is supported by

the presence of a sharp demarcation between the tissue that is apparently viable and the

tissue that has been rendered necrotic by PDT (29-31). We should note that the threshold

dose of $^1O_2$ will depend on the type of sensitizer and tumor tissue, as the subcellular sites

of primary damage could be different. Initially, it was assumed that the concentration of

$^1O_2$, and, therefore, the threshold dose that is deposited within a tumor, is proportional

to the product of the administered sensitizer concentration and the total delivered optical

density or fluence (32-34). Unfortunately, this simplified dosimetry model was found to

be valid only for a limited range of drug and light doses. This is not surprising, since one

of the basic assumptions for such a model is that sensitizer and oxygen availability as well

as light delivery remain constant throughout treatment. Studies demonstrating the

variability in time and/or space of $^3O_2$ concentration (21, 24), sensitizer availability (35-

43) and light delivery to the treatment area (44-46) during typical therapy protocols

suggest that the dynamic character of these quantities should be incorporated in PDT

dosimetry. Furthermore, the interdependence of light fluence, sensitizer concentration and

oxygen consumption contributes to a very complicated scenario for the definition of

photodynamic dose.

Work performed in our laboratory prior to my arrival emphasized the importance

of photochemical oxygen depletion in limiting the effectiveness of PDT conducted at

relatively high irradiation fluence rates (22, 23, 24, 47). Quantitative measurements of oxygen concentration are extremely difficult *in vivo* due to the complexity of the intact animal tumor system (21). Thus, we used multicell tumor spheroids, approximately 500 μm in diameter. Spheroids are avascular cell aggregates that provide an excellent tumor model for quantitative studies of oxygen diffusion and consumption, as they are characterized by similar nutrient gradients and cell populations as the ones encountered between the edge of a capillary and intercapillary regions (Figure 1.2, refs. 48-50). Studies with photosensitized multicell spheroids had enabled the quantification of certain aspects and consequences of the oxygen consumption problem (24). For purposes of simplification in establishing the theoretical framework that was used to interpret the results, the effects of sensitizer photobleaching were not included initially.

1.2.2 Sensitizer photobleaching in photodynamic dosimetry

Bleaching could play an important role in modifying the effects of photodynamic oxygen consumption because irreversible destruction of the photosensitizer must reduce the rate of photon absorption. Moreover, as it is extremely difficult to monitor changes in oxygen, light and sensitizer simultaneously during therapy, some researchers are considering alternative, implicit methods for defining and/or monitoring dosimetry during PDT (42, 46, 51, 52). These methods focus on the measurement of a quantity which depends on all, or at least most, of the above factors. Sensitizer photobleaching is one of the suggested
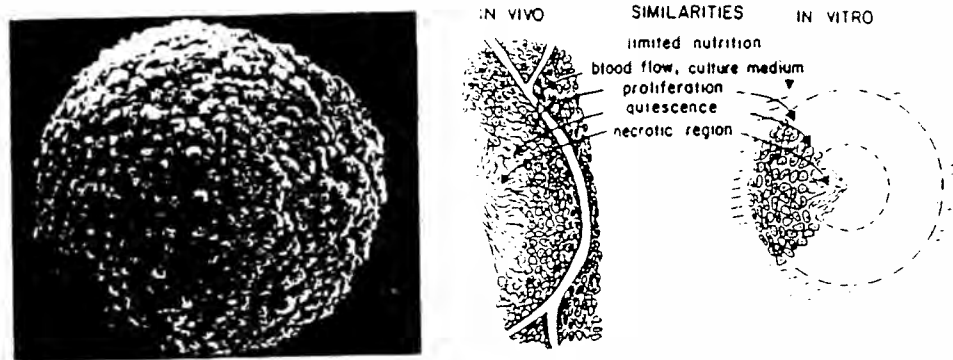
Figure 1.2: A scanning electron micrograph of a multicell tumor spheroid is shown on the left (Reproduced from Hall, E.J. (1994) *Radiobiology for the radiologist*. J.B. Lippincott Company, Philadelphia, PA). Some of the similarities between the *in vivo* tumor regions and the *in vitro* spheroid model are illustrated on the right (Reproduced from Sutherland, R.M. (1986) Importance of critical metabolites and cellular interactions in the biology of microregions of tumors. *Cancer* **58**, 1668-1680).

implicit measurements that could allow determination of the biological response that a specific treatment protocol would evoke (42, 46, 52), while autofluorescence photobleaching has been considered also (42).

To employ sensitizer photobleaching as a dose metric for PDT or to simply incorporate it into a dosimetry model, it is essential to understand how the different mechanisms that could be involved in this process affect the production and deposition of $^1O_2$. With important recent exceptions (42, 53), photobleaching has been treated in the PDT literature as a process that can be described *via* first order fluence-dependent simple exponential decay kinetics (45, 54-57). The implicit assumption underlying this phenomenological treatment is that the chemical species responsible for photobleaching does not depend on the sensitizer itself for its formation. Moreover, the concentration of the sensitizer species (*i.e.* the specific state) that undergoes degradation is assumed to be independent of oxygen concentration. Work performed by several investigators demonstrates that in some cases first order exponential decay kinetics do not adequately describe the observed sensitizer fluorescence changes during treatment (42, 43, 58-60). In other cases, $^1O_2$, whose production depends on the sensitizer population, has been identified directly or indirectly as the agent that mediates sensitizer degradation (61-67), demonstrating the importance of incorporating the dynamics of $^3O_2$ availability in photobleaching models.

A model of oxygen diffusion with consumption that incorporates the effects of photobleaching in order to analyze $^3O_2$ concentration measurements performed at the

edge of photosensitized spheroids during irradiation is presented in chapter 2. We consider initially a $^1O_2$-mediated photobleaching mechanism and one that can be described as a fluence-dependent simple exponential decay. The basic equations of the oxygen diffusion with consumption model and the photobleaching expressions presented in this chapter were developed by M.G. Nichols and T.H. Foster, while the oxygen concentration data were obtained by M.G. Nichols. However, modifications to the treatment of the metabolic rate of oxygen consumption and the saturation radius developed upon my arrival resulted in more accurate analysis of the oxygen concentration measurements. More importantly, changes related to the implementation of the numerical solutions to the diffusion equations rendered possible the analysis of oxygen concentration measurements more than a few tens of seconds in duration. The final analysis of the experimental data was performed by the author. For Photofrin®-sensitized spheroids, we find that the $^1O_2$-mediated photobleaching model accurately describes the observed changes in $^3O_2$ concentration that result from sensitizer degradation. We demonstrate that the two photobleaching descriptions affect in distinct ways the deposition of $^1O_2$ during therapy and that their effects are not equivalent even under conditions of abundant oxygen. Moreover, we show that dose distributions corrected for the effects of bleaching produce a new, significantly higher estimate for the threshold dose of reacting singlet oxygen in the multicell tumor spheroid system than previous estimates. [Most sections of this chapter have been published previously (53). Joint authorship with M.G. Nichols and T.H. Foster is gratefully acknowledged.]

In chapter 3 we develop expressions for two non-$^1O_2$-mediated photobleaching mechanisms and evaluate their effects on dosimetry. We report $^3O_2$ concentration measurements and cell survival assays with 5-ethylamino-9-diethyl-aminobenzo[a]-phenoselenazinium chloride (EtNBSe)- and ALA induced PpIX-sensitized spheroids and analyze the data using a model of oxygen diffusion with consumption that incorporates the effects of various possible photobleaching mechanisms. We consider a $^1O_2$-mediated photobleaching mechanism, mechanisms that involve reactions of excited singlet or triplet sensitizer molecules with cell substrates, and a description of photobleaching based on simple exponential decay kinetics dependent on the incident fluence. For the particular case of EtNBSe-PDT, we find that the photobleaching mechanism involving reaction of the excited triplet sensitizer with cell substrate is in best agreement with the measured $^3O_2$ distributions. Moreover, we show that the fluence-dependent simple exponential decay description of photobleaching is not consistent with any of the mechanisms that could lead to sensitizer degradation that we have considered. For analysis of the EtNBSe-sensitized spheroids we account for non-uniform drug distribution, as characterized by analysis of fluorescence measurements performed with thin (6 µm) frozen spheroid sections. Finally, we consider the effects of non-$^1O_2$-mediated photobleaching on the deposition of $^1O_2$ in our system. [Sections of this chapter have been published previously (68) and joint authorship with T.H. Foster is gratefully acknowledged.]

1.2.3 Sensitizer localization in photodynamic dosimetry

The relationship between the subcellular localization of several photosensitizers and their efficacy as PDT drugs has been the subject of extensive studies (69, 70 and references therein). Depending on incubation conditions, cell type and attributes such as ionic character, aggregation state and lipophilicity, some sensitizers were shown to localize preferentially in membranes, cytoplasmic organelles such as mitochondria and lysosomes, or the nucleus, while others exhibited diffuse localization throughout the cell (71-79). Researchers have studied for several sensitizers the effects of lysosomal localization on the cytotoxic ability of PDT (80-84). Most reports examined whether the permeabilization of the lysosomal membrane during PDT, as assayed by sensitizer and lysosomal enzyme redistribution, is an event that significantly affects cell viability. Lin *et al.* addressed this issue in human bladder carcinoma monolayer cultures sensitized with several Nile Blue derivatives, which were shown to localize mainly in the lysosomes (85-88).

In chapter 4 we present experimental evidence that demonstrates how the subcellular localization and redistribution of two Nile Blue derivatives, EtNBS and EtNBSe, might affect oxygen consumption during irradiation of sensitized multicell EMT6 spheroids. Specifically, two well-defined phases of oxygen consumption are observed during treatment, with the onset of the second phase being a fluence dependent event. Fluorescence microscopy during irradiation of EtNBS-sensitized EMT6 monolayer cultures indicates that sensitizer redistribution from intracellular organelles, presumably

lysosomes, to the cytosol can explain the onset of the second oxygen consumption phase.

This event requires eight times fewer photons for EtNBSe than for EtNBS, consistent

with the higher singlet oxygen yield of the former dye. The existence of a second oxygen

consumption phase suggests that the aggregated form of the dye is a less efficient

photodynamic agent. [Most sections of this chapter have been published previously (89).

Joint authorship with T.H. Foster is gratefully acknowledged.]

In chapter 5, we present a study that could have immediate relevance to the

localization of PpIX within a tumor on a more macroscopic scale and, therefore, on the

design of efficient protocols for tumor eradication. While most PDT photosensitizers are

exogenously administered drugs, PpIX is an effective endogenous sensitizer (90). PpIX

is one of the intermediates in the heme biosynthetic pathway, and it has been shown that

administration of excess ALA overrides one of the rate limiting steps in this pathway and

leads to accumulation of PpIX in the cells (91, 92). For reasons that are not yet com-

pletely understood, PpIX is often produced in higher amounts by malignant cells confer-

ring selective photodynamic damage to the tumor area. Although most researchers have

taken advantage of the selective PpIX accumulation in the tumor to treat the malignancy

by means of photodynamic therapy, others have employed PpIX fluorescence detection

as a tool for the diagnosis of disease (93, 94).

The effectiveness of PpIX as a PDT sensitizer and as a diagnostic agent has

prompted a significant amount of research on the factors that affect PpIX synthesis. Such

studies have explored the role of ALA incubation time (95-97) and concentration (96-98),

cell type (99-101), cell cycle (98), proliferation status (102-104), serum presence (105, 106), iron availability (101, 106, 107, 108), pH (97, 109, 110, 111), glucose (95), and temperature (95). More detailed studies examined the effect of some of these factors on specific enzymes of the heme biosynthetic pathway (112, 113). In chapter 5, we report on the effects of hypoxia on ALA-induced PpIX synthesis in EMT6 monolayer cultures characterized by different cell densities and proliferation rates. Specifically, following ALA incubation under hypoxic or normoxic conditions we detect spectrofluorometrically the PpIX content of the following populations: a) low density exponentially growing cells, b) high density fed-plateau cells, and c) high density unfed-plateau cells. These populations are selected either for the purpose of comparison with other *in vitro* studies (low density exponentially growing cells) or as representatives of tumor regions adjacent to (high density fed-plateau cells) and further away from (high density unfed-plateau cells) capillaries. We find that the amount of PpIX per cell produced by each one of these populations is higher after normoxic ALA incubation, while the magnitude of the effect of hypoxia on PpIX synthesis is dependent on cell density and proliferation rate. [This chapter has been accepted for publication in the British Journal of Cancer (114). Joint authorship with P.C. Keng and T.H. Foster is gratefully acknowledged.]

1.3   Confocal microscopy as a tool for the direct study of sensitizer photobleaching and localization

The work presented in chapters 2-4 demonstrates that $^3O_2$ consumption is so central to the photochemistry occurring during PDT that we can extract information about sensitizer photobleaching and localization indirectly by analyzing photodynamically induced $^3O_2$ concentration changes. The next step is to study these processes directly and confirm the predictions that our photobleaching models make. Additionally, while the monolayer culture studies on PpIX synthesis under hypoxia provide an excellent foundation for understanding some of the dependencies of PpIX production, studies in increasingly complicated tumor models should confirm their relevance to the *in vivo* situation. Observing differences in PpIX synthesis within the different populations of a multicell tumor spheroid would provide the next level of complexity. Conventional fluorescence microscopy is not very useful for the study of such processes in thick, highly scattering specimens such as spheroids because of its inability to reject out-of-focus light. However, a technique such as fluorescence confocal microscopy, known for its superior lateral and axial resolution capabilities even in thick biological samples, should allow us to observe sensitizer photobleaching and localization directly in spheroids.

In chapter 6, we describe the design and characterization of a laser beam scanning confocal attachment to an inverted microscope. This fluorescence confocal microscope is designed for the purpose of imaging through optical sections of sensitized multicell

spheroids with a resolution on the cellular level to: a) study the process of sensitizer

photobleaching directly *via* changes in sensitizer fluorescence during irradiation, and b)

observe any non-uniformities in the synthesis of PpIX as a result of the oxygen gradients

and the differences in the cell proliferation rates that exist between the outer, highly

proliferating spheroid regions and the inner, more quiescent populations. A slightly

modified system could provide resolutions on the subcellular level and allow us to study

simultaneously sensitizer redistribution and its effects on oxygen consumption during PDT

of EtNBS-sensitized spheroids. We demonstrate that the lateral and axial resolution of the

system meets our design specifications. Moreover, we present images through EtNBS-

sensitized spheroids, demonstrating the feasibility of the proposed studies. In the final

chapter, we summarize our results and indicate the future directions that this work can

follow.

References

1.   Dougherty, T.J., C.J. Gomer, B.W. Henderson, G. Jori, D. Kessel, M. Korbelik,

      J. Moan and Q. Peng (1998) Photodynamic therapy. *J. Nat. Cancer Inst.* **90**, 889-

      905.

2.   Jeffes, E.W., J.L. McCullough, G.D. Weinstein, P.E. Fergin, J.S. Nelson, T.F.

      Shull, K.R. Simpson, L.M. Bukaty, W.L. Hoffman and N.L. Fong (1997)

      Photodynamic therapy of actinic keratosis with topical 5-aminolevulinic acid. A

pilot dose-ranging study. *Arch. Dermatol.* **133**, 727-732.

3.   Lin, S.C., C.P. Lin, J.R. Feld, J.S. Duker and C.A. Puliafito (1994) The photody-
     namic occlusion of choroidal vessels using benzoporphyrin derivative. *Curr. Eye.
     Res.* **12**, 513-522.

4.   Asrani, S. and R. Zeimer (1995) Feasibility of laser targeted photo-occlusion of
     ocular vessels. *Br. J. Opthalmol.* **79**, 766-770.

5.   Schmidt-Erfurth, U., J. Miller, M. Sickenberg, A. Bunse, H. Laqua, E. Gragou-
     das, L. Zografos, R. Birngruber, H. van den Bergh, A. Strong, U. Manjuris, M.
     Fsadni, A.M. Lane, B. Piguet and N.M. Bressler (1998) Photodynamic therapy
     of subfoveal choroidal neovascularization: clinical and angiographic examples.
     Graefes Arch. Exp. Opthalmol. **236**, 365-374.

6.   Weishaupt, K.R., C.J. Gomer and T.J. Dougherty (1976) Identification of singlet
     oxygen as the cytotoxic agent in photoinactivation of murine tumor. *Cancer Res.*
     36, 2326-2329.

7.   Gibson, S.L., H.J. Cohen and R. Hilf (1984) Evidence against the production of
     superoxide by photoirradiation of hematoporphyrin derivative. *Photochem.
     Photobiol.* **40**, 441-448.

8.   Gibson, S.L. and R. Hilf (1985) Interdependence of fluence, drug dose and
     oxygen on hematoporphyrin derivative induced photosensitization of tumor
     mitochondria. *Photochem. Photobiol.* **42**, 367-373.

9. Agarwal, M.L., M.E. Clay, E.J. Harvey, H.H. Evans, A.R. Antunez and N.L. Oleinick (1991) Photodynamic therapy induces rapid cell death by apoptosis in L5178Y mouse lymphoma cells. *Cancer Res.* **51**, 5993-5996.

10. He, X.Y., R.A. Sikes, S. Thomsen, L.W. Chung and S.L. Jacques (1994) Photodynamic therapy with photofrin II induces programmed cell death in carcinoma cell lines. *Photochem. Photobiol.* **59**, 468-473.

11. Webber, J., Y. Luo, R. Crilly, D. Fromm and D. Kessel (1996) An apoptotic response to photodynamic therapy with endogenous protoporphyrin *in vivo. J. Photochem. Photobiol. B: Biol.* **35**, 209-211.

12. Korbelik, M. (1996) Induction of tumor immunity by photodynamic therapy. *J. Clin. Laser Med. Surg.* **14**, 329-334.

13. Ochsner, M. (1997) Photophysical and photobiological processes in the photodynamic therpay of tumors. *J. Photochem. Photobiol. B: Biol.* **39**, 1-18.

14. Henderson, B.W., S.M. Waldow, T.S. Mang, W.R. Potter, R.B. Malone and T.J. Dougherty (1985) Tumor destruction and kinetics of tumor cell death in two experimental mouse tumors following photodynamic therapy. *Cancer Res.* **45**, 572-576.

15. Henderson, B.W. and V.H. Fingar (1989) Oxygen limitation of direct tumor cell kill during photodynamic treatment of a murine tumor model. *Photochem. Photobiol.* **49**, 299-304.

16. Henderson, B.W. and V.H. Fingar (1987) Relationship of tumor hypoxia and response to photodynamic treatment in an experimental mouse tumor. *Cancer Res.* **47**, 3110-3114.

17. Gibson, S.L. and R. Hilf (1983) Photosensitization of mitochondrial cytochrome c oxidase by hematoporphyrin derivative and related porphyrins *in vitro* and *in vivo*. *Cancer Res.* **43**, 4191-4197.

18. Perlin, D.S., R.S. Murant, S.L. Gibson and R. Hilf (1985) Effects of photosensitization by hematoporphyrin derivative on mitochondrial adenosine triphosphatase-mediated proton transport and membrane integrity of R3230AC mammary adenocarcinoma. *Cancer Res.* **45**, 653-658.

19. Hilf, R., R.S. Murant, U. Narayanan and S.L. Gibson (1986) Relationship of mitochondrial function and cellular adenosine triphosphate levels to hematoporphyrin derivative-induced photosensitization in R3230AC mammary tumors. *Cancer Res.* **46**, 211-217.

20. Hilf, R., S.L. Gibson, D.P. Penney, T.L. Ceckler and R.G. Bryant (1987) Early biochemical responses to photodynamic therapy monitored by NMR spectroscopy. *Photochem. Photobiol.* **46**, 809-817.

21. Tromberg, B.J., A. Orenstein, S. Kimel, S.J. Barker, J. Hyatt, J.S. Nelson and M.W. Berns (1990) *In vivo* oxygen tension measurements for the evaluation of the efficiency of photodynamic therapy. *Photochem. Photobiol.* **52**, 375-385.

22.   Foster, T.H., R.S. Murant, R.G. Bryant, R.S. Knox, S.L. Gibson and R. Hilf

       (1991) Oxygen consumption and diffusion effects in photodynamic therapy.

       Radiat. Res. **126**, 296-303.

23.   Foster, T.H. and L. Gao (1992) Dosimetry in photodynamic therapy: Oxygen and

       the critical importance of capillary density. *Radiat. Res.* **130**, 379-383.

24.   Nichols, M.G. and T.H. Foster (1994) Oxygen diffusion and reaction kinetics in

       photodynamic therapy of multicell tumor spheroids. *Phys. Med. Biol.* **39**, 2161-

       2181.

25.   Feins, R.H., R. Hilf, H. Ross and S.L. Gibson (1990) Photodynamic therapy for

       human malignant mesothelioma in the nude mouse. *J. Surg. Res.* **49**, 311-314.

26.   Cincotta, L., J.W. Foley, T. MacEachern, E. Lampros and A.H. Cincotta (1994)

       Novel photodynamic effects of a benzophenothiazine in two different murine

       sarcomas. *Cancer Res.* **54**, 1249-1259.

27.   Hua, Z., S.L. Gibson, T.H. Foster and R. Hilf (1995) Effectiveness of δ-

       aminolevulinic acid-induced protoporphyrin as a photosensitizer for photodynamic

       therapy *in vivo*. *Cancer Res.* **55**, 1723-1731.

28.   Sitnik, T.M, J.A. Hampton and B.W. Henderson (1998) Reduction of tumor

       oxygenation during and after photodynamic therapy *in vivo*: Effects of fluence

       rate. *Br. J. Cancer* **77**, 1386-1394.

29.   Berenbaum, M.C., R. Bonnett and P.S. Scourides (1982) *In vivo* biological

activity of the components of haematoporphyrin derivative. *Br. J. Cancer* **57**, 571-581.

30. van Gemert, J.C., M.C. Berenbaum and G.H.M. Gijsbers (1985) Wavelength and light-dose dependence in tumour phototherapy with haematoporphyrin derivative. *Br. J. Cancer* **52**, 43-49.

31. Bown, S.G., C.J. Tralau, P.D. Coleridge Smith, D. Akdemir and T.J. Wieman (1986) Photodynamic therapy with porphyrin and phthalocyanine sensitization: Quantitative studies in normal rat liver. *Br. J. Cancer* **54**, 43-52.

32. Fingar, V.H., W.R. Potter and B.W. Henderson (1987) Drug and light dose dependence of photodynamic therapy: A study of tumor cell clonogenicity and histologic changes. *Photochem. Photobiol.* **45**, 643-650.

33. Patterson, M.S., B.C. Wilson and R. Graff (1990) *In vivo* tests of the concept of photodynamic threshold dose in normal rat liver photosensitized by aluminum chlorosulphonated phthalocyanine. *Photochem. Photobiol.* **51**, 343-349.

34. Farrell, T.J., B.C. Wilson, M.S. Patterson and R. Chow (1991) The dependence of photodynamic threshold dose on treatment parameters in normal rat liver *in vivo. Proc. SPIE* **1426**, 146-155.

35. Mang, T.S., T.J. Dougherty, W.R. Potter, D.G. Boyle, S. Somer and J. Moan (1987) Photobleaching of porphyrins used in photodynamic therapy and implications for therapy. *Photochem. Photobiol.* **45**, 501-506.

36. Mang, T.S. and T.J. Wieman (1987) Photodynamic therapy in the treatment of pancreatic carcinoma: dihematoporphyrin ether uptake and photobleaching kinetics. *Photochem. Photobiol.* **46**, 853-858.

37. van der Veen, N., H.L.L.M. van Leengoed and W.M. Star (1994) *In vivo* fluorescence kinetics and photodynamic therapy using 5-aminolaevulinic acid-induced porphyrin: increased damage after multiple irradiations. *Br. J. Cancer* **70**, 867-872.

38. Braichotte, D.R., G.A. Wagnières, R. Bays, P. Monnier and H.E. van den Bergh (1995) Clinical pharmacokinetic studies of Photofrin by fluorescence spectroscopy in the oral cavity, the esophagus, and the bronchi. *Cancer* **75**, 2768-2778.

39. Stringer, M.R., D.J. Robinson, E.J. Hudson and M.A. Smith (1995) *In vivo* monitoring of photosensitizer fluorescence during photodynamic therapy. *Proc. SPIE* **2371**, 104-108.

40. Moesta, K.T, W.R. Greco, S.O. Nurse-Finlay, J.C. Parsons and T.S. Mang (1995) Lack of reciprocity in drug and light dose dependence of photodynamic therapy of pancreatic adenocarcinoma *in vitro*. *Cancer Res.* **55**, 3078-3084.

41. Rück, A., G. Beck, R. Bachor, N. Akgün, M.H. Gschwend and R. Steiner (1996) Dynamic fluorescence changes during photodynamic therapy *in vivo* and *in vitro* of hydrophilic Al(III) phthalocyanine tetrasulphonate and lipophilic Zn(II) phthalocyanine administered in liposomes. *J. Photochem. Photobiol. B: Biol.* **36**,

127-133.

42.   Forrer, M., T. Glanzmann, D. Braichotte, G. Wagnières, H. van den Bergh, J.F.
       Savary and P. Monnier (1995) *In vivo* measurement of fluorescence bleaching of
       meso-tetra hydroxy phenyl chlorin (mTHPC) in the esophagus and the oral cavity.
       Proc. SPIE **2627**, 33-39.

43.   Bezdetnaya, L., N. Zeghari, I. Belitchenko, M. Barberi-Heyob, J.-L. Merlin, A.
       Potapenko and F. Guillemin (1996) Spectroscopic and biological testing of photo-
       bleaching of porphyrins in solutions. *Photochem. Photobiol.* **64**, 382-386.

44.   Wilson, B.C., M.S. Patterson and D.M. Burns (1986) Effect of photosensitizer
       concentration in tissue on the penetration depth of photoactivating light. *Lasers*
       Med. Sci. **1**, 235-244.

45.   Grossweiner, L.I. (1997) PDT light dosimetry revisited. *J. Photochem. Photobiol.*
       B:Biol. **38**, 258-268.

46.   Wilson, B.C., M.S. Patterson and L. Lilge (1997) Implict and explicit dosimetry
       in photodynamic therapy: a new paradigm. *Lasers. Med. Sci.* **12**, 182-199.

47.   Foster, T.H., D.F. Hartley, M.G. Nichols and R. Hilf (1993) Fluence rate effects
       in photodynamic therapy of multicell tumor spheroids. *Cancer Res.* **53**, 1249-
       1254.

48.   Franko, A.J. and R.M. Sutherland (1979) Oxygen diffusion distance and
       development of necrosis in multicell spheroids. *Radiation Res.* **79**, 439-453.

49.   Sutherland, R.M., B. Sordat, J. Bamat, H. Gabbert, B. Bourrat and W. Mueller-
       Klieser (1986) Oxygenation and differentiation in multicellular spheroids of human
       colon carcinoma. *Cancer Res.* **46**, 5320-5329.

50.   Sutherland, R.M. (1988) Cell and environment interactions in tumor micro-
       regions: The multicell spheroid model. *Science* **240**, 177-184.

51.   Braichotte, D.R., J. Savary, P. Monnier and H. van den Bergh (1996) Optimizing
       light dosimetry in photodynamic therapy of early stage carcinomas of the
       esophagus using fluorescence spectroscopy. *Lasers Surg. Med.* **19**, 340-346.

52.   Rhodes, L.E., M.M. Tsoukas, R.R. Anderson and N. Kollias (1997) Iontophoretic
       delivery of ALA provides a quantitative model for ALA pharmacokinetics and
       PpIX phototoxicity in human skin. *J. Invest. Derm.* **108**, 87-91.

53.   Georgakoudi, I., M.G. Nichols and T.H. Foster (1997) The mechanism of
       Photofrin® photobleaching and its consequences for photodynamic dosimetry.
       Photochem. Photobiol. **65**, 135-144.

54.   Potter, W.R., T.S Mang and T.J. Dougherty (1987) The theory of photodynamic
       therapy dosimetry: consequences of photodestruction of sensitizer. *Photochem.*
       Photobiol. **46**, 97-101.

55.   Boyle, D.G. and W.R. Potter (1987) Photobleaching of Photofrin II as a means
       of eliminating skin photosensitivity. *Photochem. Photobiol.* **46**, 997-1001.

56.   Svaasand, L.O., P. Wyss, M. Wyss, Y. Tadir, B.J. Tromberg and M.W. Berns

(1996) Dosimetry model for photodynamic therapy with topically administered photosensitizers. *Lasers Surg. Med.* **18**, 139-149.

57. Rotomskis, R., G. Sreckyte and S. Bagdonas (1997) Phototransformations of sensitizers 1. Significance of the nature of the sensitizer in the photobleaching process and photoproduct formation in aqueous solution. *J. Photochem. Phobiol. B: Biol.* **39**, 167-171.

58. Moan, J. (1986) Effect of bleaching of porphyrin sensitizers during photodynamic therapy. *Cancer Lett.* **33**, 45-53.

59. Moan, J. (1988) A change in the quantum yield of photoinactivation of cells observed during photodynamic treatment. *Lasers Med. Sci.* **3**, 93-97.

60. Moan, J., G. Streckyte, S. Bagdonas, Ø. Bech and K. Berg (1997) Photobleaching of protoporphyrin IX in cells incubated with 5-aminolevulinic acid. *Int. J. Cancer* **70**, 90-97.

61. Krieg, M. and D.G. Whitten (1984) Self-sensitized photooxidation of protoporphyrin IX and related free-base porphyrins in natural and model membrane systems. Evidence for novel photooxidation pathways involving amino acids. *J. Am. Chem. Soc.* **106**, 2477-2479.

62. Krieg, M. and D. G. Whitten (1984) Self-sensitized photo-oxidation of protoporphyrin IX and related porphyrins in erythrocyte ghosts and microemulsions: a novel photo-oxidation pathway involving singlet oxygen. *J. Photochem.* **25**, 235-

252.

63.   Moan, J., C. Rimington and Z. Malik (1988) Photoinduced degradation and modification of Photofrin II in cells *in vitro*. *Photochem. Photobiol.* **47**, 363-367.

64.   Moan, J. and K. Berg (1991) The photodegradation of porphyrins in cells can be used to estimate the lifetime of singlet oxygen. *Photochem. Photobiol.* **53**, 549-553.

65.   Spikes, J.D. (1992) Quantum yields and kinetics of the photobleaching of hematoporphyrin, Photofrin II, tetra(4-sulfonatophenyl-)porphine and uroporphyrin. *Photochem. Photobiol.* **55**, 797-808.

66.   Robinson, J.D., M.R. Stringer and W.R. Crum (1996) A rate-equation analysis of protoporphyrin IX photo-oxidation. *Proc. SPIE* **2625**, 413-418.

67.   van der Veen, N., H.S. de Bruijn and W.M. Star (1997) Photobleaching during and re-appearance after photodynamic therapy of topical ALA-induced fluorescence in UVB-treated mouse skin. *Int. J. Cancer* **72**, 110-118.

68.   Georgakoudi, I. and T.H. Foster (1998) Singlet oxygen- versus nonsinglet oxygen-mediated mechanisms of sensitizer photobleaching and their effects on photodynamic dosimetry. *Photochem. Photobiol.* **67**, 612-625.

69.   Gomer, C.J. (1991) Preclinical examination of first and second generation photosensitizers used in photodynamic therapy. *Photochem. Photobiol.* **54**, 1093-1107.

70. Boyle, R.W. and D. Dolphin (1996) Structure and biodistribution relationships of photodynamic sensitizers. *Photochem. Photobiol.* **64**, 469-485.

71. Georgiou, G.N., M.T. Ahmet, A. Houlton. J. Silver and R.J. Cherry (1994) Measurement of the rate of uptake and subcellular localization of porphyrins in cells using fluorescence digital imaging spectroscopy. *Photochem. Photobiol.* **59**, 419-422.

72. Woodburn, K.W., N.J. Vardaxis, J.S. Hill, A.H. Kaye and D.R. Phillips (1991) Subcellular localization of porphyrins using confocal laser scanning microscopy. *Photochem. Photobiol.* **54**, 725-732.

73. Berg, K., A. Western, J. Bommer and J. Moan (1990) Intracellular localization of sulfonated meso-tetraphenylporphines in a human carcinoma cell line. *Photochem. Photobiol.* **52**, 481-487.

74. Boegheim, J.P.J., H. Scholte, T.M.A.R. Dubbelman, E. Beems, A.K. Raap and J. van Steveninck (1987) Photodynamic effects of hematoporphyrin-derivative on enzyme activities of murine L929 fibroblasts. *J. Photochem. Photobiol. B: Biol.* **1**, 61-73.

75. Peng, Q., G.W. Farrants, K. Madslien, J.C. Bommer, J. Moan, H.E. Danielsen and J.M. Nesland (1991) Subcellular localization, redistribution and photobleaching of sulfonated aluminum phthalocyanines in a human melanoma cell line. *Int. J. Cancer* **49**, 290-295.

76.   Kessel, D. (1986) Sites of photosensitization by derivatives of hematoporphyrin. *Photochem. Photobiol.* **44**, 489-493.

77.   Wood, S.R, J.A. Holroyd and S.B. Brown (1997) The subcellular localization of Zn(II) phthalocyanines and their redistribution on exposure to light. *Photochem. Photobiol.* **65**, 397-402.

78.   Berg, K. and J. Moan (1997) Lysosomes and microtubules as targets for photo-chemotherapy of cancer. *Photochem. Photobiol.* **65**, 403-409.

79.   Gèze, M., P. Morlière, J.C. Mazière, K.M. Smith and R. Santus (1993) Lyso-somes, a key target of hydrophobic photosensitizers proposed for photochemo-therapeutic applications. *J. Photochem. Photobiol. B: Biol.* **20**, 23-25.

80.   Santus., R., C. Kohen, E. Kohen, J.P. Reyftmann, P. Morliere, L. Dubertret and P.M. Tocci (1983) Permeation of lysosomal membranes in the course of photosensitization with methylene blue and hematoporphyrin: study by cellular microspectrofluorometry. *Photochem. Photobiol.* **38**, 71-77.

81.   Berg, K., K. Madslien, J.C. Bommer, R. Oftebro, J.W. Winkelman and J. Moan (1991) Light induced relocalization of sulfonated meso-tetraphenylporphines in NHIK 3025 cells and effects of dose fractionation. *Photochem. Photobiol.* **53**, 203-210.

82.   Berg, K., K. Prydz and J. Moan (1993) Photochemical treatment with the lysosomally localized dye tetra(4-sulfonatophenyl)porphine reults in lysosomal

release of the dye but not of β-N-acetyl-D-glucosaminidase activity. *Biochim. Biophys. Acta* **1158**, 300-306.

83. Berg, K. and J. Moan (1994) Lysosomes as photochemical targets. *Int. J. Cancer* **59**, 814-822.

84. Moan, J., K. Berg, H. Anholt and K. Madslien (1994) Sulfonated aluminium phthalocyanines as sensitizers for photochemotherapy. Effects of small light doses on localization, dye fluorescence and photosensitivity in V79 cells. *Int. J. Cancer* **58**, 865-870.

85. Lin, C., J.R. Shulok, Y. Wong, C.F. Schanbacher, L. Cincotta and J.W. Foley (1991) Photosensitization, uptake, and retention of phenoxazine nile blue derivatives in human bladder carcinoma cells. *Cancer Res.* **51**, 1109-1116.

86. Lin, C., J.R. Shulok, S.D. Kirley, L. Cincotta and J.W. Foley (1991) Lysosomal localization and mechanism of uptake of nile blue photosensitizers in tumor cells. *Cancer Res.* **51**, 2710-2719.

87. Lin, C., J.R. Shulok, S.D. Kirley, C.M. Bachelder, T.J. Flotte, M.E. Sherwood, L. Cincotta and J.W. Foley (1993) Photodynamic destruction of lysosomes mediated by nile blue photosensitizers. *Photochem. Photobiol.* **58**, 81-91.

88. Lin, C. and J.R. Shulok (1994) Enhancement of nile blue derivative-induced photocytotoxicity by nigericin and low cytoplasmic pH. *Photochem. Photobiol.* **60**, 143-146.

89. Georgakoudi, I. and T.H. Foster (1998) Effects of the subcellular redistribution of two nile blue derivatives on photodynamic oxygen consumption. *Photochem. Photobiol.* **68**, 155-122.

90. Kennedy, J.C., R.H. Pottier and D.C. Pross (1990) Photodynamic therapy with endogenous protoporphyrin IX: basic principle and present clinical experience. *J. Photochem. Photobiol. B: Biol.* **6**, 143-148.

91. Kennedy, J.C. and R.H. Pottier (1992) Endogenous protoporphyrin IX, a clinically useful photosensitizer for photodynamic therapy. *J. Photochem. Photobiol. B: Biol.* **14**, 275-292.

92. Peng, Q., T. Warloe, K. Berg, J. Moan, M. Kongshaug, K.-E. Giecksky and J.M. Nesland (1997) 5-aminolevulinic acid-based photodynamic therapy. *Cancer* **79**, 2282-2308.

93. Kennedy, J.C., S.L. Marcus and R.H. Pottier (1996) Photodynamic therapy (PDT) and photodiagnosis (PD) using endogenous photosensitization induced by 5-aminolevulinic acid (ALA): mechanisms and clinical results. *J. Clin. Laser Med. Surg.* **14**, 289-304.

94. Kriegmair, M., R. Baumgartner and R. Knüchel (1994) Fluorescence photodetection of neoplastic urothelial lesions following intravesical instillation of 5-aminolevulinic acid. *Urology* **44**, 836-841.

95. Dietel, W., K. Bolsen, E. Dickson, C. Fritsch, R. Pottier and R. Wendenburg

(1996) Formation of water-soluble porphyrins and protoporphyrin IX in 5-aminolevulinic-acid-incubated carcinoma cells. *J. Photochem. Photobiol. B: Biol.* **33**, 225-231.

96. Gibson, S.L., J.J. Havens, T.H. Foster and R. Hilf (1997) Time-dependent intracellular accumulation of δ-aminolevulinic acid, induction of porphyrin synthesis and subsequent phototoxicity. *Photochem. Photobiol.* **65**, 416-421.

97. Krammer, B. and K. Überriegler (1996) In-vitro investigation of ALA-induced protoporphyrin IX. *J. Photochem. Photobiol. B: Biol.* **36**, 121-126.

98. Moan, J., Ø. Bech, J.-M. Gaullier, T. Stokke, H.B. Steen, L.W. Ma and K. Berg (1998) Protoporphyrin IX accumulation in cells treated with 5-aminolevulinic acid: dependence on cell density, cell size and cell cycle. *Int. J. Cancer* **75**, 134-139.

99. Steinbach, P., H. Weingandt, R. Baumgartner, M. Kriegmair, F. Hofstädter and R. Knüchel (1995) Cellular fluorescence of the endogenous photosensitizer protoporphyrin IX following exposure to 5-aminolevulinic acid. *Photochem. Photobiol.* **62**, 887-895.

100. Wyld, L., J.L. Burn, M.W.R. Reed and N.J. Brown (1997) Factors affecting aminolaevulinic acid-induced generation of protoporphyrin IX. *Br. J. Cancer* **76**, 705-712.

101. Iinuma, S., S.S. Farshi, B. Ortel and T. Hasan (1994) A mechanistic study of cellular photodestruction with 5-aminolevulinic acid-induced porphyrin. *Br. J.*

Cancer **70**, 21-28.

102.   Momma, T., M.R. Hamblin and T. Hasan (1997) Hormonal modulation of the

accumulation of 5-aminolevulinic acid-induced protoporphyrin and phototoxicity

in prostate cancer cells. *Int. J. Cancer* **72**, 1062-1069.

103.   Rebeiz, N., C.C. Rebeiz, S. Arkins, K.W. Kelley and C.A. Rebeiz (1992)

Photodestruction of tumor cells by induction of endogenous accumulation of

protoporphyrin IX: enhancement by 1,10-phenanthroline. *Photochem. Photobiol.*

55, 431-435.

104.   Schick, E., R. Kaufmann, A. Rück, A. Hainzl and W.-H. Boehncke (1995)

Influence of activation and differentiation of cells on the effectiveness of

photodynamic therapy. *Acta Derm. Venereol.* **75**, 276-279.

105.   Fukuda, H., A.M.C. Batlle and P.A. Riley (1993) Kinetics of porphyrin

accumulation in cultured epithelial cells exposed to ALA. *Int. J. Biochem.* **25**,

1407-1410.

106.   Hanania, J. and Z. Malik (1992) The effect of EDTA and serum on endogenous

porphyrin accumulation and photodynamic sensitization of human K562

leukemic cells. *Cancer Letters* **65**, 127-131.

107.   Rittenhouse-Diakun, K., H. van Leengoed, J. Morgan, E. Hryhorenko, G.

Paszkiewicz, J.E. Whitaker and A.R. Oseroff (1995) The role of transferrin

receptor (CD71) in photodynamic therapy of activated and malignant lympho-

cytes using the heme precursor δ-aminolevulinic acid (ALA). *Photochem. Photobiol.* **61**, 523-528.

108. Tan, W.C., N. Krasner, P. O'Toole and M. Lombard (1997) Enhancement of photodynamic therapy in gastric cancer cells by removal of iron. *Gut* **41**, 14-18.

109. Bech, Ø., K. Berg and J. Moan (1997) The pH dependency of protoporphyrin IX formation in cells incubated with 5-aminolevulinic acid. *Cancer Letters* **113**, 25-29.

110. Bermúdez Moretti, M., S. Correa García, C. Stella, E. Ramos and A.M.C. Del C. Batlle (1993) δ-aminolevulinic acid transport in saccharomyces cerevisiae. *Int. J. Biochem.* **25**, 1917-1924.

111. Wyld, L., M.W.R. Reed and N.J. Brown (1998) The influence of hypoxia and pH on aminolaevulinic acid-induced photodynamic therapy in bladder cancer cells *in vitro. Br. J. Cancer* **77**, 1621-1627.

112. Gibson, S.L., D.J. Cupriks, J.J. Havens, M.L. Nguyen and R. Hilf (1998) A regulatory role for porphobilinogen deaminase (PBGD) in δ-aminolaevulinic acid (δ-ALA)-induced photosensitization? *Br. J. Cancer* **77**, 235-243.

113. Schoenfeld, N., O. Epstein, M. Lahav, R. Mamer, M. Shaklai and A. Atsmon (1988) The heme biosynthetic pathway in lymphocytes of patients with malignant lymphoproliferative disorders. *Cancer Letters* **43**, 43-48.

114. Georgakoudi, I., P.C. Keng and T.H. Foster (1998) Hypoxia significantly reduces

aminolaevulinic acid-induced protoporphyrin IX synthesis in EMT6 cells. *Br. J.*

Cancer In Press.

Chapter 2

Singlet Oxygen-Mediated Sensitizer Photobleaching and Its Consequences for Photodynamic Dosimetry

2.1   Introduction

As mentioned in chapter 1, there are several factors that can affect dosimetry during photodynamic therapy. Not only do we have to consider the initial interactions involving the photosensitizer, light, oxygen, and the various biological targets within the tissue, but also we have to account for the possible dynamic changes in these parameters during treatment. Therefore, understanding how these factors are modified during therapy is of critical importance for the design of useful dosimetry models.

Previous work in our laboratory examined the effects of photochemical $^3O_2$ depletion on the efficacy of PDT (1). Analysis of photodynamic $^3O_2$ consumption measurements in photosensitized multicell tumor spheroids allowed the study of the oxygen depletion problem and some of its consequences in a quantitative manner (1). The initial analysis of these measurements did not incorporate the effects of sensitizer photobleaching. However, irreversible sensitizer degradation leads to a reduced rate of photon absorption, and, thus, a modified rate of $^3O_2$ consumption and $^1O_2$ production.

In this chapter, we evaluate an extension to the previous analysis of time-dependent $^3O_2$ consumption and diffusion in spheroids to incorporate explicitly the effects of photobleaching. We consider two cases: one in which the sensitizer is bleached through a mechanism that depends only on the total optical energy density delivered to the sample, and a second wherein bleaching is mediated by $^1O_2$ reaction with the ground state of the sensitizer. The former most closely resembles the way in which bleaching has been considered by several authors in the context of PDT (2-5). The latter, $^1O_2$-mediated mechanism is consistent with observations from experiments that have been reported by various investigators (6-10). These two theories are used to analyze data from measurements obtained using $^3O_2$ sensitive microelectrodes during laser irradiation of Photofrin®-sensitized EMT6 spheroids. We find that bleaching is readily observable in the electrode measurements if irradiation is performed for a sufficiently long period of time. Moreover, the data appear to be well described by a model of $^1O_2$-mediated photobleaching but not by a model which is based solely on optical fluence. Finally, we consider

the effects of photobleaching on photodynamic dose distributions in multicell systems and on experimental determinations of the threshold dose.

2.2   Theoretical description of photochemical oxygen consumption with sensitizer photobleaching

A mathematical model of the spatial and temporal distribution of the oxygen concentration, $[^3O_2](r,t)$, within and in the proximity of a photosensitized multicell tumor spheroid during PDT was developed previously (1). Briefly, the following time-dependent diffusion equations are used to describe the kinetics of photochemical $^3O_2$ consumption:

$$\frac{\partial [^3O_2](r,t)}{\partial t} = D_d \nabla^2 [^3O_2](r,t) \qquad\qquad R_s \le r < R_d \qquad\qquad (2.1)$$

$$\frac{\partial [^3O_2](r,t)}{\partial t} = D_s \nabla^2 [^3O_2](r,t) - \Gamma(r,t) \qquad 0 \le r < R_s \qquad\qquad (2.2)$$

where D_d and D_s are the diffusion coefficients of $^3O_2$ in the medium and in the spheroid, respectively, R_s is the spheroid radius, $\Gamma(r,t)$ is the sum of the metabolic, Γ_{met}, and photodynamic, Γ_{PDT}, rates of $^3O_2$ consumption, and R_d is the radius of the $^3O_2$ depletion zone, which is the region immediately exterior to the spheroid where the $^3O_2$ concentration of the medium is affected by the presence of the spheroid. In contrast to the previous model, where the depletion radius was assumed to be constant throughout PDT, the present

treatment allows the boundary at the depletion radius to vary dynamically as a function of the spatially averaged rate of $^3O_2$ consumption (See Appendix A). Specifically, upon the onset of irradiation, the depletion zone boundary is forced to move farther away from the spheroid edge in response to the increased photodynamic $^3O_2$ consumption in the spheroid. As the $^3O_2$ concentrations reach a quasi-equilibrium state, the depletion radius assumes its maximum value. It then decreases gradually as photobleaching effects become significant and the photochemical $^3O_2$ consumption decreases. The incorporation of this change is necessary for the proper analysis of the extended time-dependent $^3O_2$ measurements that demonstrate the effects of bleaching.

In the previous analysis, the metabolic rate of $^3O_2$ consumption, Γ_{met}, was determined from spatially resolved, steady-state measurements of the $^3O_2$ concentration inside and in the vicinity of a spheroid, using a method introduced by Mueller-Klieser (11). These measurements were made in the absence of laser irradiation, but the metabolic rate was assumed to remain constant throughout the spheroid during photodynamic treatment. However, shortly after the onset of PDT the central region of the spheroid becomes anoxic, and a more rigorous treatment should provide for the cessation of metabolic $^3O_2$ consumption in the anoxic region. Therefore, in this chapter we improve upon the previous treatment by incorporating an $^3O_2$-dependent expression for Γ_{met}, which is written,

$$\Gamma_{met} = \Gamma_{met}^{max} \left(\frac{[^3O_2](r,t)]}{k_{50} + [^3O_2](r,t)} \right) \qquad (2.3)$$

where Γ_{met}^{max} is the metabolic rate of $^3O_2$ consumption determined from the steady-state

electrode measurements, and k_{50} is the $^3O_2$ concentration at which Γ_{met} acquires its half-maximum value. On the basis of experimental results obtained by Wilson *et al.* (12, 13) we have adopted a value of 0.5 µM for k_{50}. A lower value for k_{50} (0.04 µM) has been reported by Oshino *et al.* (14). However, our electrode measurements are not sufficiently sensitive to distinguish between these two k_{50}'s.

If photobleaching is neglected, the photodynamic rate of $^3O_2$ consumption, Γ_{PDT}, may be written,

$$\Gamma_{PDT}(t) = \Gamma_0 \left(\frac{k_{ot}[^3O_2](t)}{k_{ot}[^3O_2](t) + k_p} \right) \tag{2.4}$$

where

$$\Gamma_0 = S_\Delta \varphi_t I_a \left(\frac{k_{oa}[A]}{k_d + k_{oa}[A]} \right), \tag{2.5}$$

S_Δ is the fraction of the triplet-quenching collisions between ground state oxygen and triplet state sensitizer molecules that result in singlet oxygen formation, φ_t is the sensitizer triplet yield, I_a is the rate of photon absorption by the sensitizer, k_{ot} is the bimolecular rate of triplet sensitizer quenching by oxygen, k_{oa} is the bimolecular rate of reaction between $^1O_2$ and substrate *[A]*, and k_d and k_p are the rates of monomolecular decay of $^1O_2$ and the sensitizer triplet state, respectively. Since sensitizer degradation will decrease the rate of photon absorption, photobleaching reduces the rate of photodynamic $^3O_2$ consumption. Thus, some modification to Eq. 2.4 is required to include this effect. It should be noted that the fluence rate may be safely assumed to be uniform throughout the spheroid due to its small size (approximately 500 µm in diameter) relative to the size of the irradiating laser beam, which is approximately 0.5 cm in diameter. The specific form of the modified

expression for Γ_{PDT} (Eq. 2.4) will depend on the mechanism of photobleaching. The most

direct first approach would be to reduce the rate of photodynamic $^3O_2$ consumption

according to a simple exponential bleaching term, $e^{-\alpha D}$, where D is the fluence (J cm^{-2}) and

α is the bleaching coefficient (J^{-1} cm^2). In such a case, Eq. 2.4 becomes,

$$\Gamma_{PDT}(t) = \Gamma_0 \left(\frac{k_{ot}[^3O_2](t)}{k_{ot}[^3O_2](t) + k_p} \right) \exp(-\alpha D), \tag{2.6}$$

and the loss of photosensitizer absorption will be uniform throughout the spheroid. While

this form would facilitate comparison with other phenomenological descriptions of

photobleahcing *in vivo* (for example, Potter *et al.* (3)), it is important to emphasize that

the mechanistic assumption implicit in this analysis is that the agent responsible for

bleaching does not depend on the photosensitizer, for only in such an instance can the

bleaching coefficient be constant.

A second possible mechanism implicates $^1O_2$ as the direct mediator of sensitizer

photobleaching. In this self-sensitization scheme, the photosensitizer is degraded by

chemical reaction with $^1O_2$. Therefore, photobleaching is not spatially uniform but

constrained to those regions of the spheroid where $^1O_2$ concentrations are significant. The

derivation of the expression describing $^1O_2$-mediated photobleaching has been presented

in detail elsewhere (1, 15). Briefly, assuming that $^1O_2$ reacts only with the ground state

of the photosensitizer, and noting that: a) in the absence of photobleaching, the sensitizer

concentration will be constant, and b) the loss of ground state absorption proceeds much

slower than the rates associated with the primary photochemical reactions occurring during treatment, we arrive at a simple sensitizer population decay expression,

$$\frac{d[S_0]}{dt} = -k_{os}[S_0][^1O_2],\tag{2.7}$$

where k_{os} is the bimolecular rate constant for $^1O_2$ reaction with ground state photosensitizer. We note that since the $^1O_2$ concentration is dependent on the sensitizer concentration, Eq. 2.7 represents a photobleaching mechanism which cannot be characterized by a constant photobleaching coefficient, such as α in Eq. 2.6. After replacing $[^1O_2](t')$ in the solution of Eq. 2.7 with the steady-state solution to the appropriate rate equation evaluated at a given time, t, and considering that the sensitizer concentration in tissue is much lower than the effective intracellular concentration of targets for $^1O_2$, we arrive at an expression describing $^1O_2$-mediated sensitizer degradation as

$$[S_0](t) = [S_0](0)\exp\left(-\frac{k_{os}}{k_{oa}[A]}\int_0^t S_\Delta \varphi_t I_a(t')\left(\frac{k_{ot}[^3O_2](t')}{k_{ot}[^3O_2](t') + k_p}\right)\left(\frac{k_{oa}[A]}{k_d + k_{oa}[A]}\right)dt'\right).\tag{2.8}$$

Since the rate of photon absorption, $I_a(t)$, is proportional to the ground state sensitizer concentration, $[S_0](t)$, Eq. 2.8 expresses the rate at which light absorption by the sensitizer is lost as a result of the reaction of the latter with $^1O_2$. In this model, the expression for Γ_{PDT} becomes

$$\Gamma_{PDT}(t) = \Gamma_0\left(\frac{k_{ot}[^3O_2](t)}{k_{ot}[^3O_2](t) + k_p}\right)\exp\left(-\frac{k_{os}}{k_{oa}[A]}\int_0^t \Gamma_{PDT}(t')dt'\right).\tag{2.9}$$

It should be re-emphasized that under no condition does a simple exponential decay (*i.e.*, constant bleaching coefficient) describe the loss of light absorption that results from $^1O_2$-mediated photobleaching. Even when bleaching is not limited by $^3O_2$ availability, the rate of photodynamic $^3O_2$ consumption will be a time-dependent function because of the progressive loss of sensitizer concentration. Therefore, Eq. 2.9 cannot be reduced to a form that is equivalent to that of Eq. 2.6, even under conditions of abundant $^3O_2$.

2.3 Experimental results and analysis

2.3.1 Studies examining uniform sensitizer uptake by the spheroids

One of the assumptions that we make when we derive the expression for the photodynamic rate of $^3O_2$ consumption is that the sensitizer is uniformly distributed throughout the spheroid. If that is not the case, then the maximum rate of photodynamic $^3O_2$ consumption, Γ_0, has to be modified to express this non-uniformity. To test the validity of this assumption for the experiments described in this chapter we obtain fluorescence images of thin sections from Photofrin®-sensitized spheroids.

Specifically, EMT6 spheroids are incubated in a 100 mm suspension tissue culture dish containing 15 mL Eagle's basal medium (Gibco-BRL, Grand Island, NY) with 10% fetal calf serum (Gibco-BRL) and 10 µg mL^{-1} Photofrin® at 37°C in a humidified 5% CO_2-95% air atmosphere for approximately 24 h. Then, the spheroids are transferred to a 15 mL centrifuge tube and washed three times with Hank's Balanced Salt Solution (HBSS, Gibco-BRL). Once the spheroids settle at the bottom of the tube, the HBSS is carefully

aspirated with a pasteur pipette. A small amount of aqueous embedding media (Tissue-Tek OCT compound, Sakura Finetek USA Inc., Torrance, CA) is placed at the bottom of a 10mm x 10mm x 5mm cryomold (Sakura Finetek USA Inc.) and allowed to freeze at -23°C. The bare end of a Q-tip is used to scrape the spheroids from the bottom of the centrifuge tube and smear them onto the frozen OCT. More OCT is added to the cryomold so that the spheroids are completely covered, and the cryomold is frozen solid at -23° C. The frozen bloc is mounted on the bloc holder of a Zeiss cryostat (HM505N, Carl Zeiss Inc., Thornwood, NY), and 6 μm sections are cut through the frozen spheroids. These sections are affixed to plain microscope slides and allowed to air dry before observation.

The fluorescence from these Photofrin®-stained sections is imaged with a Nikon Microphot-SA microscope equipped with a Ludl automated stage and filter wheel and a Xillix MicroImager 1400 CCD camera interfaced to a Sun Sparc LX station. The camera and stage are controlled using SCIL-image software and the acquired images (640 x 512 pixels) are converted to TIFF format for further viewing and analysis. An exposure time of 150 ms is used for recording the Photofrin® fluorescence. The field of view in the horizontal direction is 700 μm.

The fluorescence of a typical Photofrin®-stained spheroid section approximately 400 μm in diameter is depicted in Figure 2.1a. Indeed, we find that for the particular incubation protocol Photofrin® is taken up by cells throughout the spheroid in a reasonably uniform manner, with more intense staining observed only for a single cell layer at the outermost rim of the spheroid. This is illustrated in a more quantitative

manner by a fluorescence intensity cross-section through the middle of the sensitized

spheroid in Figure 2.1b. Images obtained with spheroids that were not treated with drug

but prepared and imaged in an identical manner (Figure 2.2) confirm that the signal in

Figure 2.1 is Photofrin® fluorescence. Therefore, our assumption that Γ_0 is uniform

throughout the spheroid is a reasonably good assumption.

2.3.2 Measurements of $^3O_2$ consumption and extraction of sensitizer photobleaching rates

The experimental apparatus used to obtain the $^3O_2$ microelectrode measurements is

depicted in Figure 2.3 and has been described previously (16). After a small number of

spheroids (10-20) is incubated with Photofrin® as described in section 2.3.1, a single

spheroid (~ 500 µm in diameter) is selected and placed in an open dish filled with 20 mL

HBSS. The spheroid is pinned with a thin glass micropipette (8 µm outer diameter) atop

a pedestal that is covered with an $^3O_2$ permeable membrane. Two stereomicroscopes

allow us to control in three dimensions the positioning of the pin and microelectrode with

respect to the spheroid.

In the absence of irradiation, a series of $^3O_2$ concentration measurements are taken

by moving the electrode tip from the depletion zone radius to the center of the spheroid

in 20 µm increments. A typical steady-state profile is shown in Figure 2.4. The solutions

of the steady-state form of Eqs. 2.1 and 2.2 are fitted to this radial $^3O_2$ profile using a

Levenberg-Marquardt non-linear-least-squares fitting algorithm (1, 15). Thus, we obtain

(a)

(b)
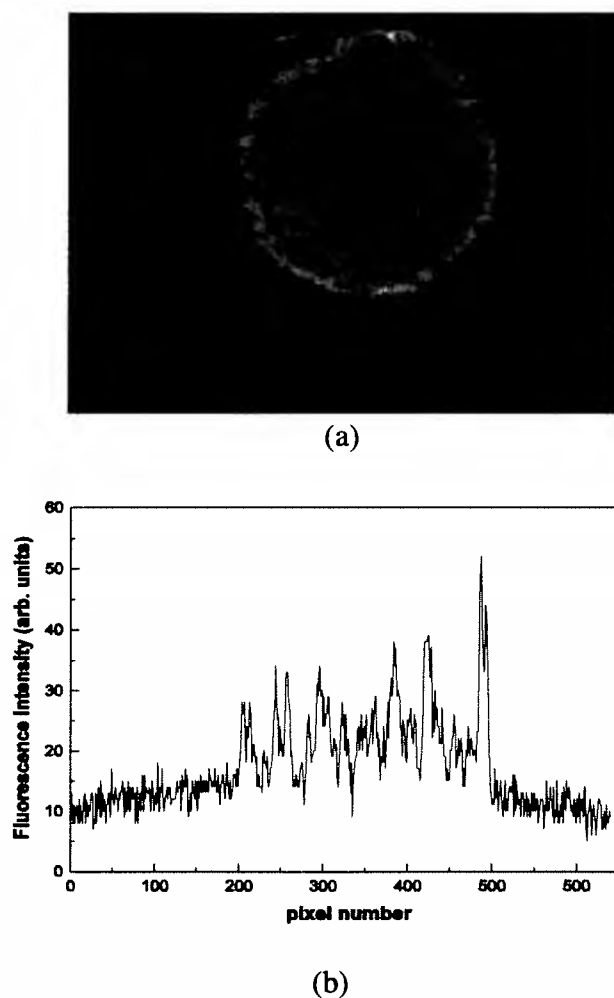
Figure 2.1: Photofrin® is taken up by cells throughout the spheroid in a reasonably uniform manner. (a) Fluorescence image of a 6μm frozen section from a spheroid, approximately 400 μm in diameter, sensitized with 10 μg mL^{-1} Photofrin® for 24 hours. The image consists of 640x512 pixels and is acquired in 150 ms by a CCD camera attached to a fluorescence microscope. (b) Fluorescence intensity profile of cross-section through the center of the spheroid section image shown in (a).

(a)

(b)
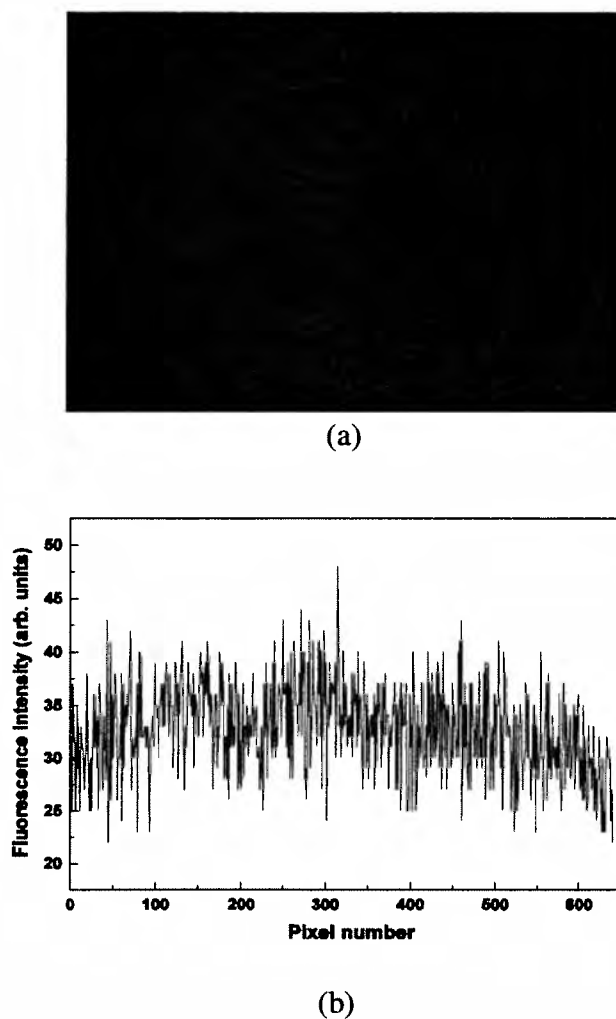
Figure 2.2: (a) No autofluorescence is detectable within a 6 μm section of a spheroid that is not sensitized with Photofrin®. The sections are prepared and imaged using the identical procedure followed for obtaining images of Photofrin®-sensitized spheroid sections. The dark outline of the spheroid is barely noticeable in this case. The fluorescence intensity profile through the center of the spheroid section, shown in (b), illustrates that the detected signal is not distinguishable from background.
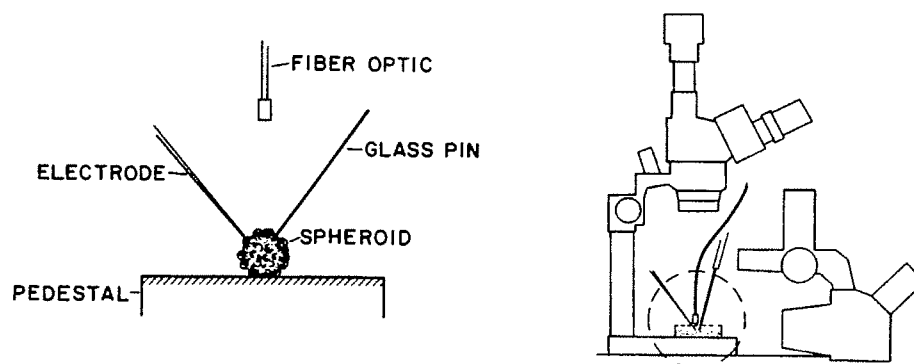
Figure 2.3: Experimental set-up for oxygen microelectrode measurements. In the left

panel, the spheroid is shown on top of the oxygen permeable membrane of the pedestal.

A glass pipette is used to hold the spheroid in place while the microelectrode records ^{3}O$_2$

concentrations within and in the vicinity of the spheroid. During irradiation, light is

delivered to the spheroid *via* an optical fiber. This set up is in an open dish containing 20

mL HBSS and positioned with respect to two stereomicroscopes in such a way so that

we have three-dimensional control of the positioning of the pin and the microelectrode

(right panel). Using this set-up, ^{3}O$_2$ concentration changes can be observed with a spatial

resolution of 10 μm and a temporal resolution of 0.5 s. (Figure reproduced from Nichols

and Foster (16).)
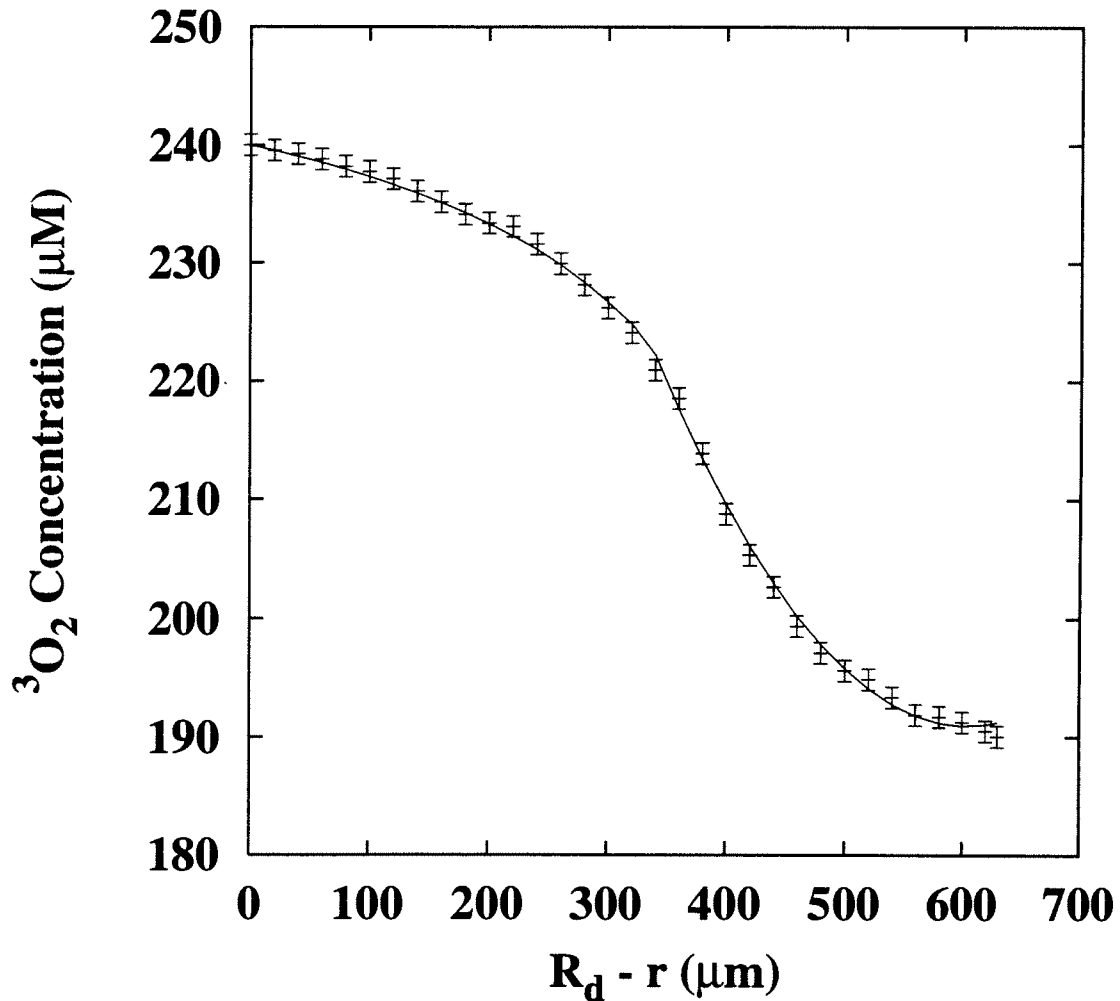
Figure 2.4: Steady-state $^3O_2$ concentration measurements as a function of radial distance

r from the depletion zone radius, R_d, in and around a spheroid. The solid line represents

the best fit to the data achieved with the solutions of the steady-state form of Eqs. 2.1 and

2.2. A Levenberg-Marquardt non-linear-least-squares fitting algorithm is used. A

discontinuity in the $^3O_2$ concentration changes is observed at the spheroid edge, *i.e.* at

R_d-R_s, as a result of the different diffusion coefficients of $^3O_2$ in the medium and in the

spheroid.

values for the $^3O_2$ diffusion constant in the spheroid, D_s, the steady-state metabolic rate

of $^3O_2$ consumption, Γ_{met}^{max}, and the steady-state depletion zone radius, $R_d(t=0)$.

During the next stage of the experiment, the electrode is placed at the edge of the

spheroid. Light from an argon ion laser (514 nm) is delivered to the spheroid, and we

record the electrode current during irradiation. We observe a significant rapid decrease

in $^3O_2$ concentration followed by a gradual increase as the sensitizer photobleaches and

photochemical $^3O_2$ consumption decreases. The solutions of Eqs. 2.1 and 2.2 are fitted

to the initial changes in $^3O_2$ concentration to obtain the photodynamic $^3O_2$ consumption

parameters, Γ_0 and k_p/k_{ot}, of Eq. 2.9. It should be noted that Eqs. 2.1 and 2.2 cannot be

solved analytically. A numerical solution is implemented by discretizing the radial and

temporal components of the problem following a Crank-Nicolson scheme (17) and casting

them onto a radial lattice. The discretized equations can be written in a tridiagonal matrix

form and solved numerically using standard procedures (18). A detailed description of the

procedure can be found in ref. (15). We have confirmed that no detectable photobleaching

occurs during these early transients, which are no longer than 40 s in duration. These

short duration $^3O_2$ concentration profiles are re-analyzed using the modified treatment of

Γ_{met} and the depletion zone radius, since, initially, these parameters were treated as

constants throughout irradiation. No significant changes in the maximum rate of

photodynamic $^3O_2$ consumption, Γ_0, and, therefore in β_{PDT} (the proportionality constant

between Γ_0 and the fluence rate (1)) result from the more rigorous treatment of the

depletion zone boundary. However, this treatment affected appreciably the estimate of

k_p/k_{ot}, the $^3O_2$ concentration at which a triplet state sensitizer molecule is as likely to be

quenched by $^3O_2$ as it is to decay directly to its ground state. Analysis of a set (n=7) of

40 s electrode transients using a constant depletion zone boundary yields a value for k_p/k_{ot}

of 4.9 ± 0.8 μM, while analysis of the same data set using a depletion zone radius that is

coupled to the rate of $^3O_2$ consumption yields a k_p/k_{ot} of 11.9 ± 2.2 μM. Table 2.1

presents a comparison of the values obtained for these parameters for the constant and

variable depletion radius cases. The modification of the expression for the metabolic rate

of $^3O_2$ consumption had a small practical effect in determining Γ_0 and k_p/k_{ot}. Nevertheless,

this correction improves the agreement of fits to microelectrode data recorded for

different lengths of time, as shown in Figure 2.5.

During the final stage of data analysis, we use the values of Γ_0 and k_p/k_{ot} obtained

from the 40 s transients to fit the entire time-dependent data set and obtain either α (Eq.

2.6) or k_{os}/k_{oa} [A] (Eq. 2.9). To analyze these $^3O_2$ concentration profiles that typically

extend over several hundreds of seconds of irradiation it is necessary to modify the

manner in which the numerical solutions to the diffusion equations are implemented. Spe-

cifically, the numerical solutions of Eqs. 2.1 and 2.2 are calculated at time-steps varying

in duration exponentially as a function of time as explained in detail in Appendix B.

Incorporation of sensitizer degradation as expressed in Eq. 2.9 allowed solutions

to the time-dependent diffusion equations to be fit to the electrode data with excellent

agreement. A typical time-dependent distribution of $^3O_2$ concentrations observed at the

edge of a Photofrin®-treated spheroid undergoing 50 mW cm^{-2} irradiation is shown in

Table 2.1: Effects of the moving depletion zone radius on parameter estimates

Parameter	Constant R_d	Moving R_d
β_{PDT}	1.55 ± 0.47 μM s^{-1} mW^{-1} cm^2	1.87 ± 0.75 μM s^{-1} mW^{-1} cm^2
k_p/k_{ot}	4.9 ± 0.8 μM	11.9 ± 2.2 μM
k_{os}/k_{oa} [A]	98 ± 12 M^{-1}	76 ± 12 M^{-1}
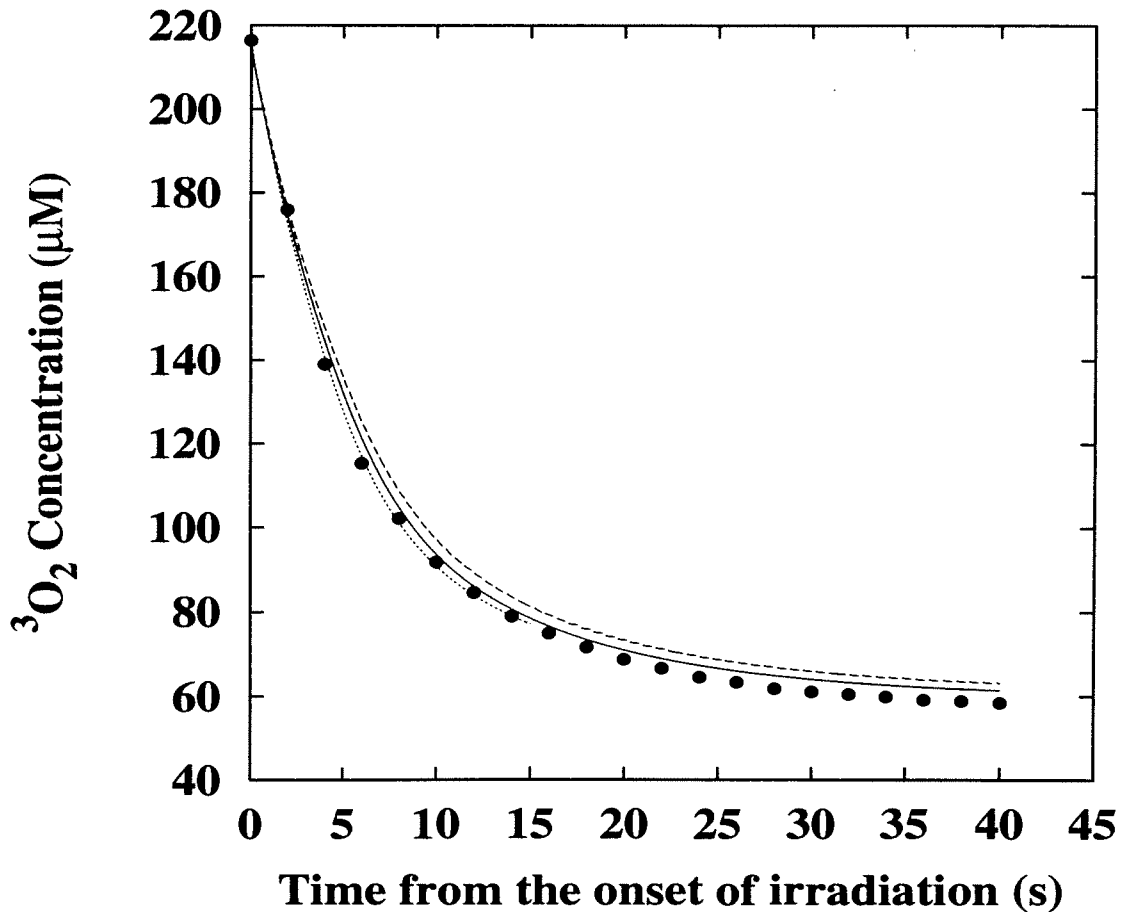
Figure 2.5: The effect of incorporating an $^3O_2$ dependence into the rate of metabolic $^3O_2$

consumption (Γ_{met}). The symbols (●) are samples of the time-dependent $^3O_2$ concentration

measured at the edge of a Photofrin®-sensitized EMT6 spheroid during the first 40 s of

514 nm irradiation (40 mW cm^{-2}). The dashed line (- - -) is the best fit to the data using

a numerical solution to Eqs. 2.1 and 2.2 and a constant Γ_{met}, whereas the solid line

(————) is the fit obtained using the form of Γ_{met} expressed in Eq. 2.3. Shown for

comparison is the fit obtained to only the first 15 s of data (······). The fits for the two

different equations of Γ_{met} overlap in this case.

Figure 2.6. The best fit obtained when Eq. 2.9 is used for Γ_{PDT}, *i.e.*, when photobleaching

is assumed to be a $^1O_2$-mediated process, is depicted in Figure 2.6. This may be compared

to the best fit that is achieved when a constant photobleaching rate is considered, *i.e.*,

when Eq. 2.6 is used (Figure 2.7a). While the $^1O_2$-mediated fit captures all of the

important features of the data, it is evident that the predictions of the simple exponential

description of photobleaching are not in good agreement with the experiment. In Figure

2.7b, a family of simulated $^3O_2$ concentration curves are plotted with constant bleaching

coefficients varying from 0.02 to 0.08 J^{-1} cm^2 to demonstrate that it is impossible to

capture in a satisfactory way both the early and the later parts of the measured $^3O_2$

concentrations. This is a trend that we observe consistently with irradiation fluence rates

of 40, 50, 80, and 100 mW cm^{-2}. Thus, we conclude that Photofrin® bleaches *via* a $^1O_2$-

mediated mechanism.

From seven experiments conducted using the fluence rates mentioned above, we

find that the value of the ratio k_{os}/k_{oa} *[A]* is 76 ± 12 M^{-1} (mean ± standard deviation).

Interestingly, but probably coincidentally, when the $^3O_2$ distributions are analyzed using

the simple exponential photobleaching expression, Eq. 2.6, the average value of the

oxygen independent bleaching coefficient, α, is approximately 0.04 J^{-1} cm^2, a value close

to that reported by others who have estimated Photofrin® photobleaching rates from

analysis of the fluorescence decay measured at the surface of tumors (3). It should be

stressed once more that the constant bleaching coefficient does not represent a limiting

form of the $^1O_2$-mediated bleaching term under conditions of abundant oxygen. The
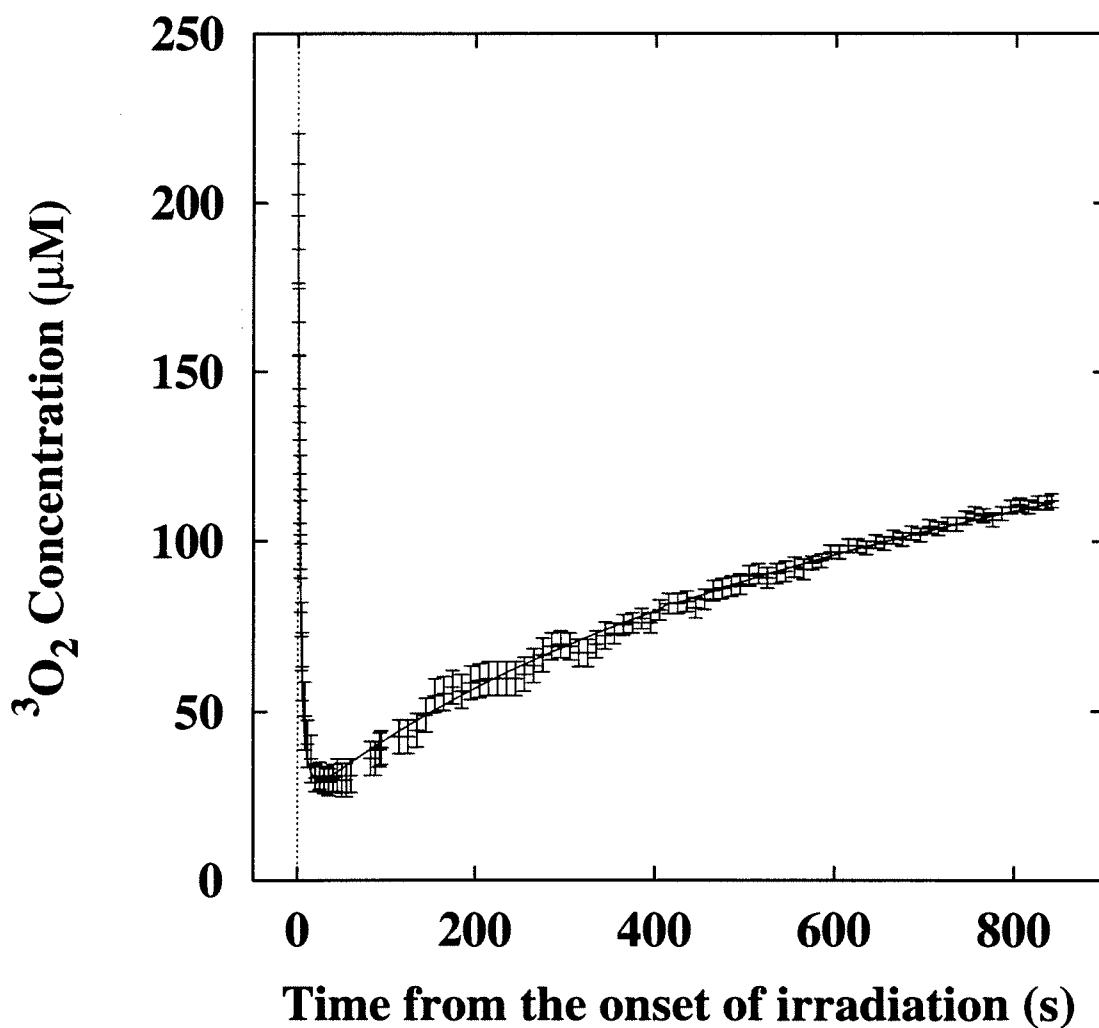
Figure 2.6: Typical time-dependent $^3O_2$ concentration distribution recorded using a microelectrode at the edge of a Photofrin®-sensitized spheroid during 514 nm irradiation at 50 mW cm^{-2}. The solid line is the best fit to the data using the singlet oxygen-mediated theory of sensitizer photobleaching expressed in Eq. 2.9. Error bars indicate estimates of the uncertainty in the oxygen electrode measurements.

(a)

(b)
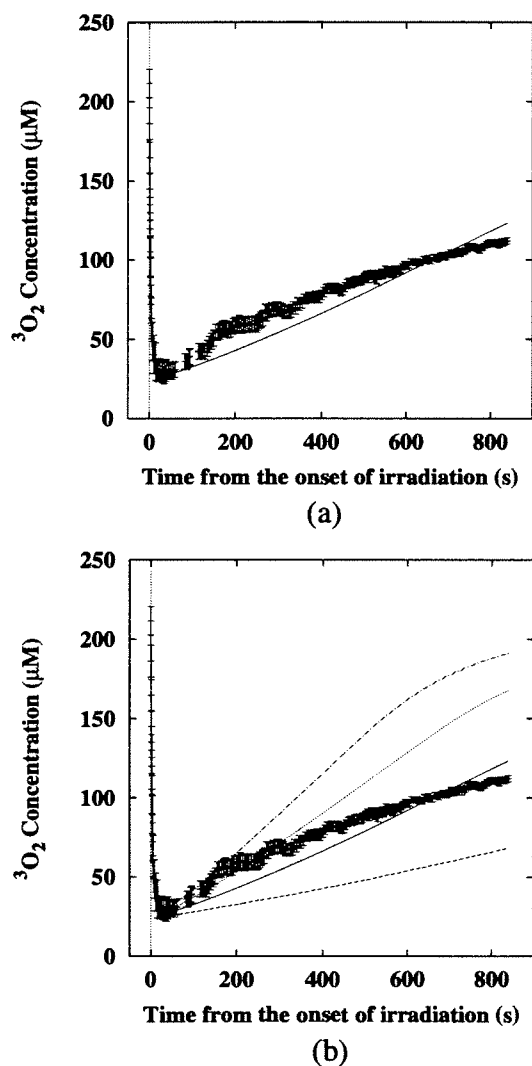
Figure 2.7: The same time-dependent $^3O_2$ concentration distribution as that shown in

Figure 2.6 is included in this figure. The solid line in panel (a) is the best fit to the data

achieved when the fluence dependent constant bleaching coefficient model of Eq. 2.6 is

used. Figure 2.7b shows calculated time-dependent $^3O_2$ distributions using the constant

bleaching coefficient model with α of 0.02 (- - -), 0.04 (————), 0.06 ($\cdots\cdots$), and 0.08

(- $\cdot$ - $\cdot$ -) J^{-1} cm^2.

average value of α is reported only because it is used in the following figures that compare

the consequences of the two different bleaching schemes.

2.3.3 Effects of photobleaching on photodynamic $^3O_2$ consumption and $^1O_2$ deposition

The effects of photobleaching on the spatial and temporal distribution of $^3O_2$ within and

in the immediate vicinity of a spheroid are demonstrated in Figure 2.8. Simulations of $^3O_2$

concentrations in space and time, using parameter values that were obtained from the

analysis of the electrode data, are shown for an optical fluence of 60 J cm^{-1} delivered at

100 mW cm^{-2} for three cases: a) no bleaching, Figure 2.8a; b) $^1O_2$-mediated bleaching

when k_{os}/k_{oa} $[A]$ is 76 M^{-1}, Figure 2.8b; and c) bleaching occurring at a constant rate of

0.04 J^{-1} cm^2, Figure 2.8c. As expected, the extent of anoxia in the central region of the

spheroid decreases significantly when photobleaching is incorporated into the simulations.

Comparison of Figures 2.8a and 2.8b indicates that after 600 s of irradiation at 100 mW

cm^{-2}, the radial distance over which the $^3O_2$ concentration is depleted is reduced from

nearly 200 μm to approximately 100 μm, respectively. This implies that bleaching sustains

$^1O_2$ production over a larger spheroid fraction. Moreover, the distributions corresponding

to the two forms of bleaching are substantially different, suggesting the importance of

correctly identifying the photobleaching mechanism. For example, the constant

photobleaching rate has the effect of eliminating PDT-induced $^3O_2$ depletion throughout

the spheroid after less than 500 s of irradiation under these conditions (Figure 2.8c).
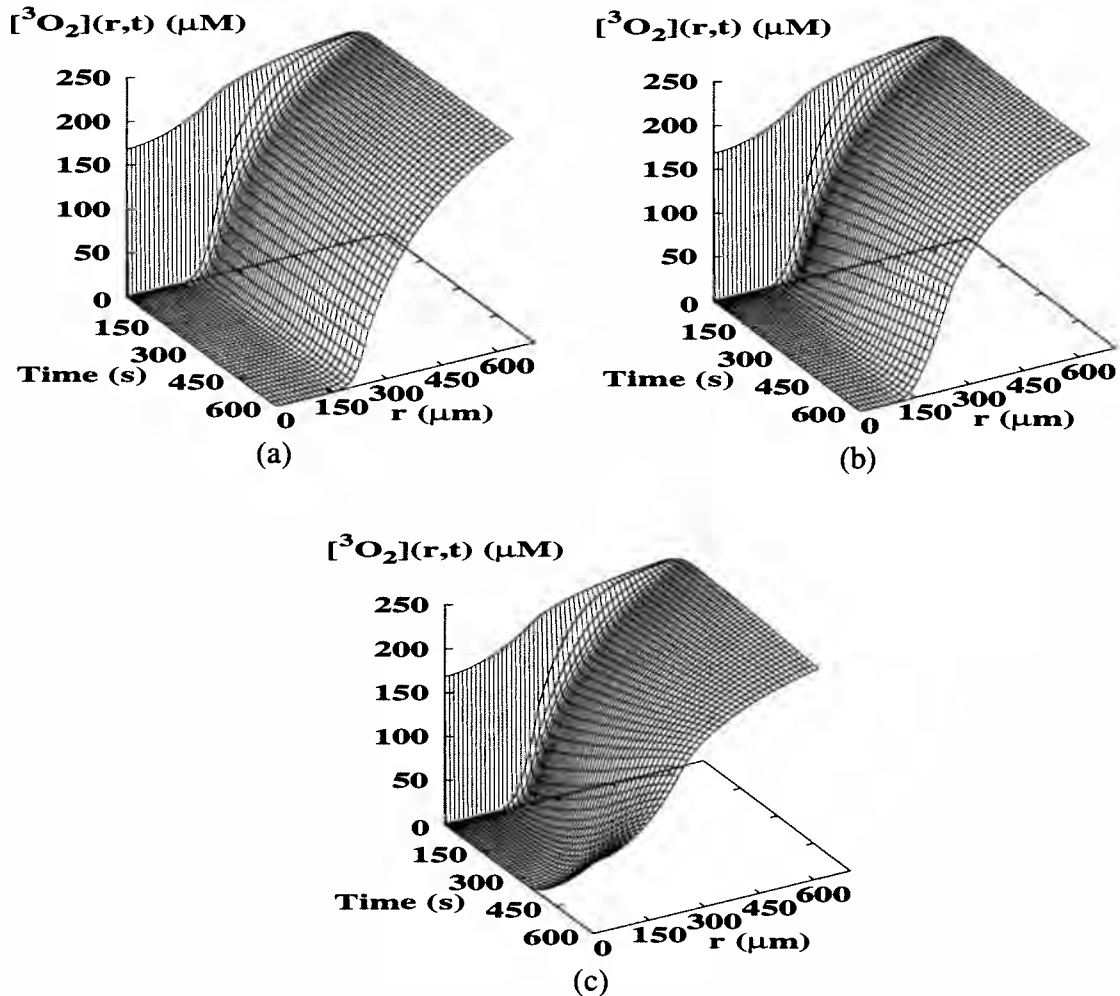
Figure 2.8: Calculated temporal and spatial distributions of the $^3O_2$ concentration in a 250 μm radius spheroid during PDT conducted at 100 mW cm^{-2} (630 nm) when: (a) no photobleaching occurs; (b) $^1O_2$-mediated photobleaching occurs with $k_{os}/k_{oa}[A] = 76$ M^{-1}, and (c) photobleaching occurs at a constant rate of $\alpha = 0.04$ J^{-1} cm^2. The axis label "Time (s)" denotes time upon the onset of irradiation, while "r (μm)" denotes distance from the center of the spheroid (r=0) to the depletion zone radius. The calculations are performed using parameters derived from microelectrode measurements.

The effects of photobleaching on $^1O_2$ production are shown more explicitly in Figure 2.9. The plotted net photochemical $^3O_2$ consumption distributions are the result of calculations conducted for the same irradiation protocols as those used for Figure 2.8 (100 mW cm^{-2}, 60 J cm^{-2}). Considering that once $^1O_2$ is produced, it diffuses less than 70 nm before it reacts with substrate (19), we may equate these $^3O_2$ consumption distributions with patterns of $^1O_2$ deposition. Under conditions of $^1O_2$-mediated photobleaching, photochemical $^3O_2$ consumption is extended further into the center of the spheroid than when no photobleaching occurs. Initially, $^1O_2$ is produced predominantly in the outermost regions of the spheroid where $^3O_2$ is readily available. As sensitizer molecules in the outer rim photobleach *via* their interaction with $^1O_2$, the decrease in photochemical $^3O_2$ consumption allows $^3O_2$ to diffuse further into the spheroid and sustain significant $^1O_2$ production over a larger volume. The simple exponential model of photobleaching extends appreciable photodynamic dose all the way to the center of the spheroid for this set of experimental conditions. Since in this model the photosensitizer is uniformly bleached throughout the spheroid as a function of optical energy density, the rate of photochemical $^3O_2$ consumption is also uniformly diminished, which produces a smoother spatial distribution of reacting $^1O_2$. Consequently, significantly different values will be predicted for the threshold dose of $^1O_2$, depending on the assumptions that are adopted regarding the photobleaching mechanism.
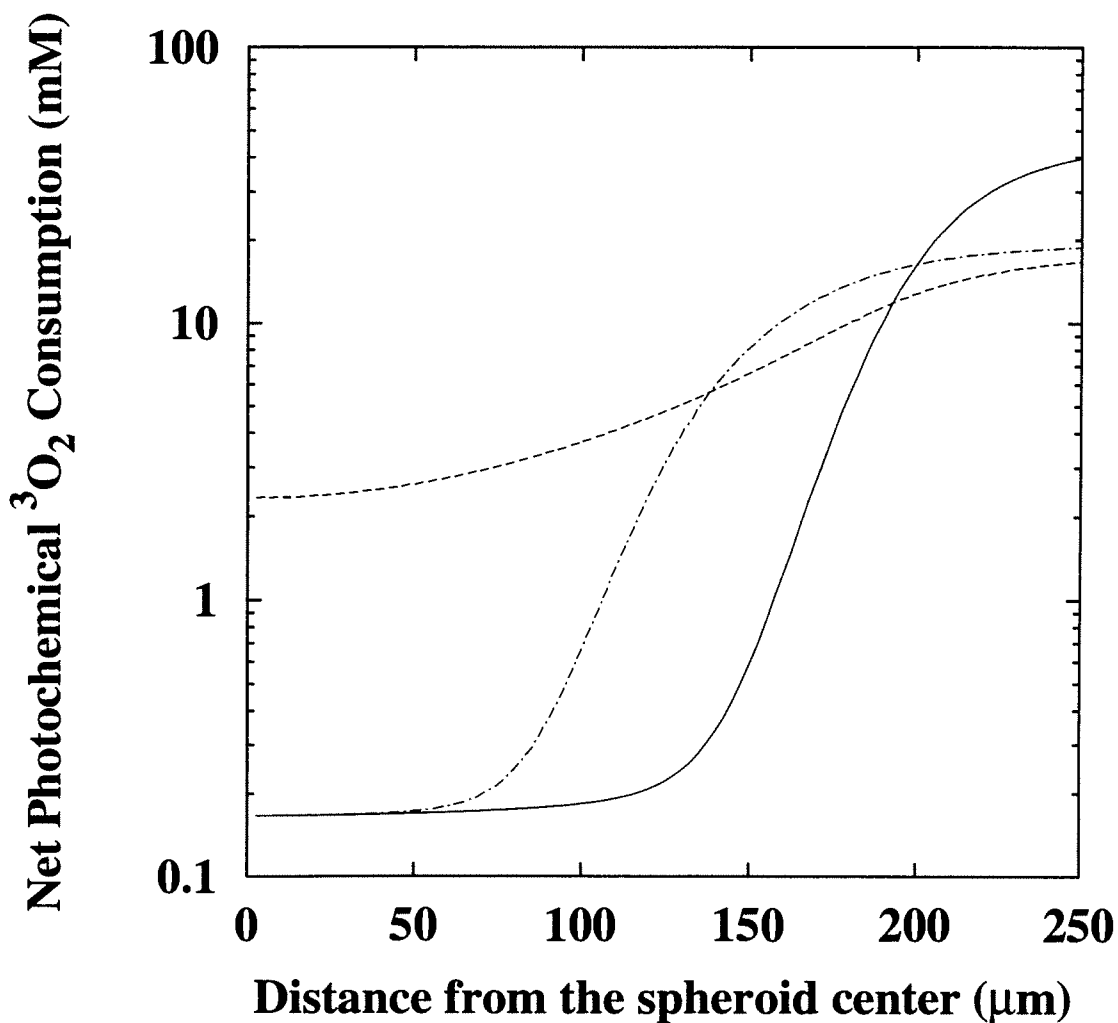
Figure 2.9: Calculated net photochemical $^3O_2$ consumption distributions within a Photofrin®-treated spheroid following a fixed dose of PDT (630 nm, 60 J cm^{-2}, 100 mW cm^{-2}) under the assumption of no photobleaching (———), $^1O_2$-mediated photobleaching with k_{os}/k_{oa} [A] = 76 M^{-1} (- · - · -), and photobleaching at a constant rate with α = 0.04 J^{-1}cm^2 (- - - -).

2.3.4 Effects of photobleaching on threshold dose estimates

The net photochemical $^3O_2$ consumption curves shown in Figure 2.10 depict the effects of fluence rate on $^1O_2$ deposition for irradiations performed using 200, 100, 50, and 25 mW cm^{-2} and a total fluence of 60 J cm^{-2}. For all cases, the photodynamic rate of $^3O_2$ consumption used to compute the dose distributions incorporated parameters derived from the microelectrode experiments, including the experimentally derived value for k_{os}/k_{oa} [A] of 76 M^{-1}. While the presence of sensitizer photobleaching diminishes the severity of the fluence rate-dependent spatial deposition of $^1O_2$, a pronounced fluence rate effect on spheroid cell survival is still predicted for these experimental conditions. However, because the reduced photochemical $^3O_2$ consumption associated with bleaching extends the radial distance over which appreciable $^1O_2$ is produced, the estimate of the threshold dose of reacting $^1O_2$ for this system is significantly increased by the incorporation of photobleaching into the analysis.

The dose distributions of Figure 2.10 were calculated for the conditions specified in order to compare them with previously published results of spheroid cell survival experiments (20). Briefly, spheroids are treated with 10 μg mL^{-1} of Photofrin® for 24 h, and then groups of 50 spheroids are handpicked and treated with a fixed dose of 630 nm light delivered using four different fluence rates. A group of the spheroids that is not irradiated is used for estimating the mean and standard deviation of the spheroid diameter for the particular experiment. After irradiation, the spheroids are dissociated and the fraction of cells that survives PDT is determined by a colony formation assay.
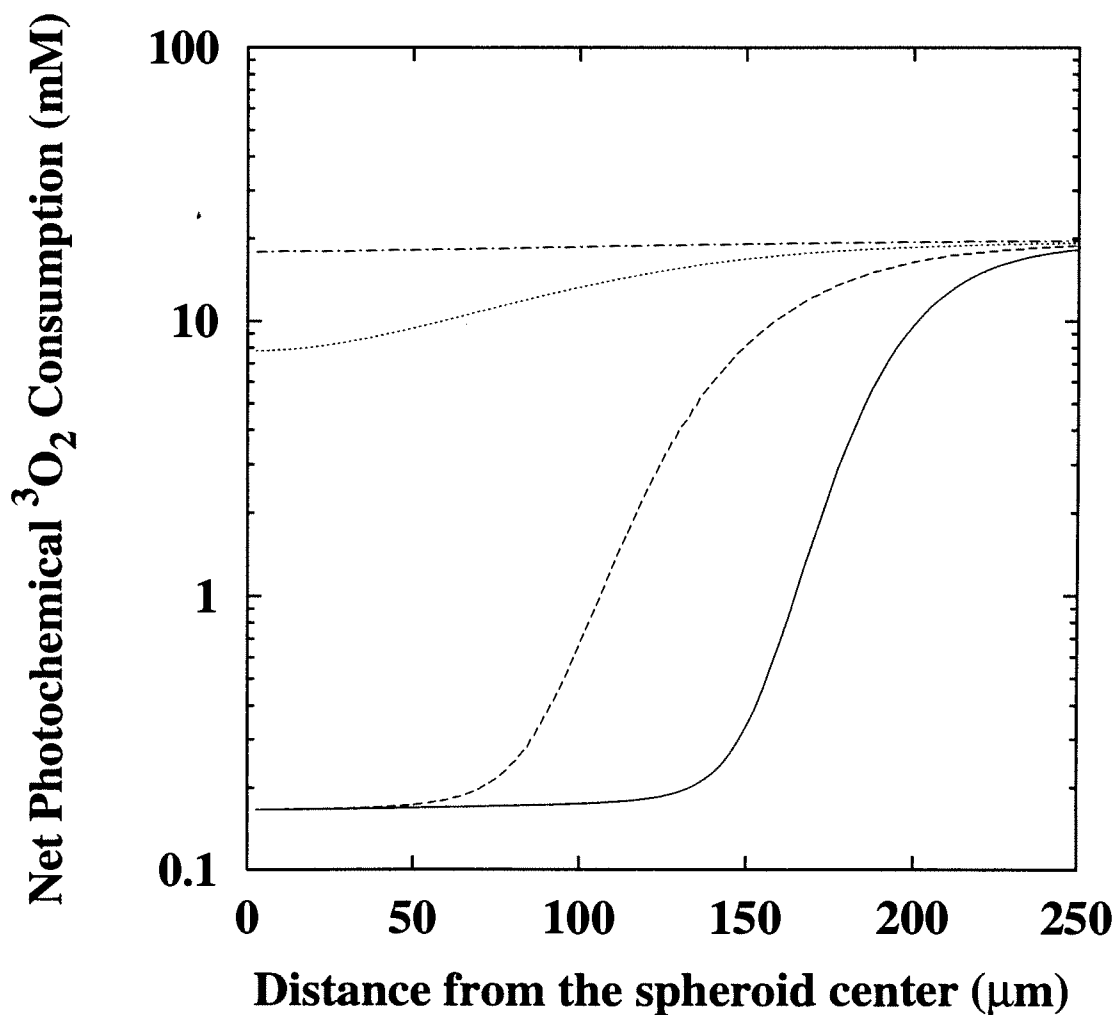
Figure 2.10: Calculated net photochemical $^3O_2$ consumption distributions within a Photofrin®-treated spheroid following a fixed PDT dose (630 nm, 60 J cm^{-2}) administered at four different fluence rates: 25 mW cm^{-2} (- · - · -), 50 mW cm^{-2} (······), 100 mW cm^{-2} (- - -), and 200 mW cm^{-2} (———).

As described previously (1), the threshold dose estimates are derived by assuming that the measured spheroid cell surviving fractions originate within the anoxic central core of the spheroid where minimal $^1O_2$ is formed during PDT. By comparing the volume of this surviving fraction with dose distributions similar to those of Figure 2.10, it is possible to determine the concentration of reacting $^1O_2$ at the border separating those cells that do and do not survive PDT administered using a particular fluence rate. Performing this analysis using the dose distributions that include the effects of $^1O_2$-mediated photo-bleaching of Photofrin® results in a threshold dose estimate of 12.1 ± 1.2 mM (mean ± standard error of the mean). This value is significantly higher than the previous estimate (0.323 mM), which was computed assuming no photobleaching (Eq. 2.4). Differences in the estimates for the threshold dose with and without photobleaching for 14 spheroid cell survival assays are depicted in Figure 2.11.

2.3.5 $^1O_2$-mediated photobleaching and data obtained by others

As shown in Figure 2.12, the expression for the $^1O_2$-mediated photobleaching of Photofrin® is consistent with fluorescence decay data reported previously by Moan (21). These data were obtained from NHIK 3025 cells treated with 0.4 or 12.5 µg mL^{-1} Photofrin® for 18 h and irradiated with 340-420 nm light at 1.2 mW cm^{-2} while the cells were suspended in media in 4 mm cuvettes, i.e., under conditions that were clearly not $^3O_2$-limited (see Figure 3, Moan (21)). While the observed fluorescence decay deviates
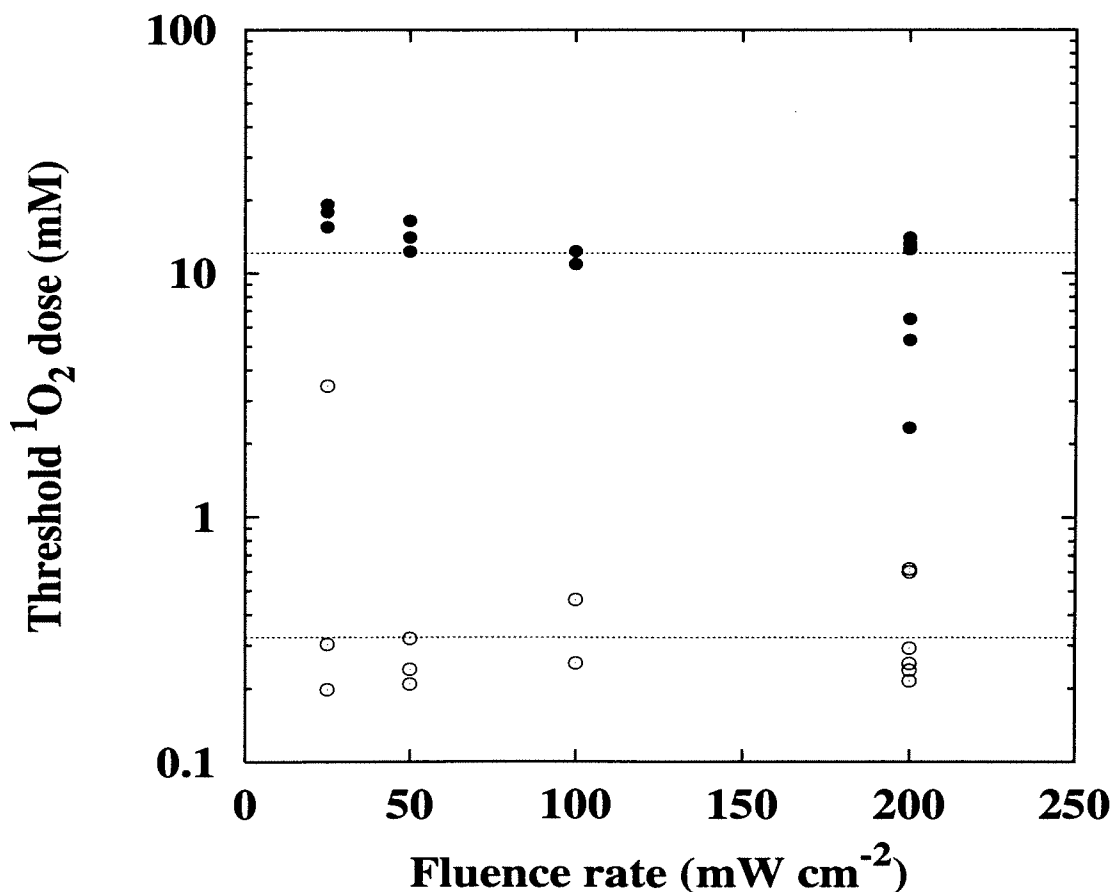
Figure 2.11: Threshold dose estimates for 14 separate spheroid cell survival experiments using a constant fluence (60 J cm^{-2}) delivered at fluence rates of 25, 50, 100, and 200 mW cm^{-2}. The open symbols (o) depict previously reported threshold estimates (0.323 ± 0.038 mM, mean ± SEM), computed without incorporation of photobleaching effects (1). Filled symbols (●) are the revised threshold estimates computed from photodynamic dose distributions like those of Figure 2.10, which are derived from the $^1O_2$-mediated bleaching theory. The mean threshold dose is 12.1 ± 1.2 mM (mean ± SEM). Spheroid surviving fractions and average diameters for these experiments are tabulated in Nichols and Foster (1).
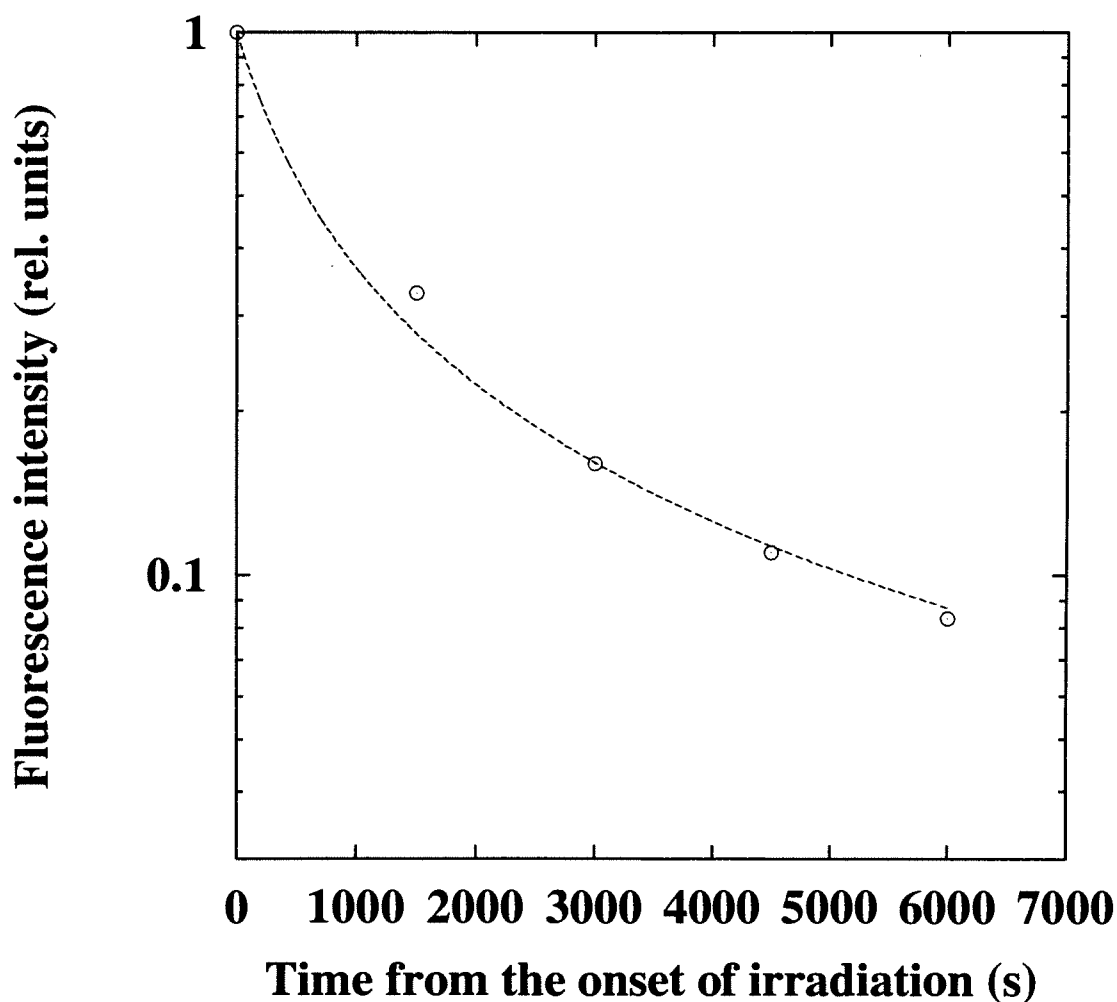
Figure 2.12: Fluorescence (λ_{ex} = 410 nm, λ_{em} = 630 nm) *vs.* time of irradiation (1.2 mW cm^{-2}) from Photofrin®-sensitized NHIK 3025 cells reported by Moan (data from Figure 3 (21)). The dashed line is the fit obtained using Eq. 2.10, which is derived from the $^1O_2$-mediated bleaching theory.

considerably from a simple exponential, it can be modeled by the $^1O_2$-mediated bleaching

expression evaluated in this chapter:

$$\exp\left(-\frac{k_{os}}{k_{oa}[A]}\int_0^t \Gamma_{PDT}(t')dt' \right), \tag{2.10}$$

where $k_{os}/k_{oa}[A]$ is 76 M^{-1}, the value obtained from fitting microelectrode data like those

shown in Figure 2.6, and Γ_{PDT} is given by Eq. 2.9. To obtain a reasonable fit to the

fluorescence data depicted in Figure 2.12 ($\lambda_{ex} = 410$ nm, $\lambda_{em} = 630$ nm), the maximum rate

of photodynamic $^3O_2$ consumption, Γ_0, was varied. The dashed line in the Figure corre-

sponds to a Γ_0 of 24 μM s^{-1}, which in turn corresponds to a proportionality constant

between Γ_0 and the fluence rate of about 20 μM s^{-1} mW^{-1} cm^2. Considering that the

measured proportionality constant at 514 nm is approximately 1.9 μM s^{-1} mW^{-1} cm^2 (1)

and that the absorption coefficient of Photofrin® at 410 nm is more than eight-fold higher

than that at 514 nm, the above value for Γ_0 appears to be reasonable.

2.4   Discussion

2.4.1   A $^1O_2$-mediated mechanism is consistent with Photofrin®

photobleaching data presented by several investigators

The focus of this chapter is the evaluation of a theory of $^1O_2$- mediated photobleaching

that is consistent with direct and indirect experimental evidence presented by ourselves

and by several other investigators. Specifically, we demonstrated that direct microelectrode measurements of the $^3O_2$ concentration near a Photofrin®-sensitized spheroid during PDT are interpretable on the basis of a model in which photosensitizer absorption is diminished as a result of chemical reaction between $^1O_2$ and the sensitizer ground state (Figure 2.6). Further, we showed that the microelectrode data are inconsistent with a simple exponential bleaching model, wherein the sensitizer absorption is lost as a function of optical fluence (Figures 2.7a, b).

Additionally, as we show in Figure 2.12, a model of $^1O_2$-mediated photobleaching is in qualitative agreement with fluorescence decay measurements performed in cuvettes with suspensions of Photofrin®-sensitized cells. Moan demonstrated that the fluorescence decay observed in such experiments was non-exponential (21, 22). This trend was attributed by Moan to either a:) chemical modifications of the sensitizer that do not affect its macrocycle, or b:) a photo-induced relocalization of the sensitizer to a slightly different cellular environment. While the Photofrin® fluorescence emission spectra in those reports were consistent with these explanations, it is interesting to note that the $^1O_2$-mediated photobleaching theory, as expressed in Eq. 2.10, predicts a non-exponential fluorescence decay without invoking the formation of new photoproducts or changes in the sensitizer local environment. Of course, our interpretation does not and cannot exclude the presence of these effects, and it is possible or even likely that all of these factors are contributing to the observed non-exponential behavior.

Our results are also consistent with more recent work performed in cell free media

by Spikes that demonstrates the oxygen dependence of Photofrin® photobleaching (10).

In that study, the photobleaching yield of Photofrin® after 30 min of nitrogen bubbling

decreased to 4% of the yield obtained in air-saturated media. A small effect in the

photobleaching yields was observed when D_2O or azide, a $^1O_2$ quencher, were present in

the medium. Substitution of H_2O with D_2O resulted in an increased photobleaching rate

of Photofrin® in cells as well, suggesting the involvement of $^1O_2$ in this process (5, 8).

Furthermore, it has been shown that when cells are treated with both Photofrin® and tetra

(3-hydroxyphenyl) porphyrin, a diffusive, photosensitized, reactive intermediate, most

probably $^1O_2$, can mediate the photodegradation of either one of the sensitizers when the

other is optically excited (9).

2.4.2 Effects of sensitizer photobleaching on photodynamic dosimetry

The fact that Photofrin® bleaches *via* a $^1O_2$-mediated mechanism means that

photobleaching is restricted to regions of abundant $^1O_2$ production. However, since

sensitizer depletion results in decreased photodynamic $^3O_2$ consumption, diffusion will

supply $^3O_2$ to cells at increasing distances from the source as irradiation proceeds. This

in turn will progressively extend the distance from the $^3O_2$ supply over which appreciable

$^1O_2$ is formed. Thus, a critical conclusion of this study is that sensitizer photobleaching

is fundamentally linked to the spatial distribution of photodynamic dose. Furthermore, as

the plots of Figures 2.8 and 2.9 make clear, the mechanism of photobleaching plays a

significant role in determining the dose distributions, with the simple exponential and $^1O_2$-mediated models predicting very different outcomes.

There are two immediate consequences that follow from the incorporation of photobleaching into the calculations of the net photochemical $^3O_2$ consumption (*i.e.*, reacting $^1O_2$) throughout a spheroid subjected to a particular PDT treatment. The first is a revised and significantly higher estimate of the threshold dose of reacting $^1O_2$ in this experimental system. As described earlier in section 2.3.4, the threshold dose estimates are based on the assumption that spheroid cells which survive PDT originate in the therapy-induced anoxic central region of the spheroid. Since photobleaching acts to increase the photodynamic dose to the inner regions, the calculated threshold dose at the critical radius separating surviving from non-surviving cells will necessarily be higher when photobleaching effects are included than when they are not. The magnitude of the change in the estimate of the threshold emphasizes the importance of including photo-bleaching in the calculation of photodynamic dose distributions. Our revised threshold dose estimate of 12.1 ± 1.2 mM is now significantly higher than the 0.9 mM value for Photofrin® that was published by Farrell *et al.* on the basis of depth of necrosis measurements in normal rat liver (23). In considering this apparent discrepancy, it should be noted that the depth of necrosis *in vivo* probably results from a combination of direct cell and physiological responses to photodynamic insult, whereas only direct cell effects are present in the spheroid. Thus, a lower threshold dose might be anticipated *in vivo*. It is also important to emphasize that the two types of threshold measurements are quite

different and were performed on different tissues. Nevertheless, this discrepancy is grounds for further research.

The second consequence of photobleaching for dosimetry is the fact that bleaching diminishes the extent to which photodynamic dose is spatially confined for a given set of treatment conditions. Thus, the magnitude of the fluence rate effect is diminished in the presence of sensitizer photobleaching. Further, because bleaching continues to decrease the rate of photodynamic $^3O_2$ consumption as treatment progresses, the degree to which the fluence rate effect is lessened depends on the total photodynamic dose. The dose curves of Figure 2.10, which are computed using parameters derived from direct microelectrode measurements and which include the contribution of $^1O_2$-mediated photobleaching, illustrate that, for the case of 500 μm diameter spheroids subjected to 60 J cm^{-2} (630 nm), a fluence rate dependent cell survival is predicted over the range 25-200 mW cm^{-2}. This is consistent with previously published survival results for this system and treatment conditions (20). Calculations performed for the case of a 120 J cm^{-2} treatment (not shown) demonstrate that a pronounced fluence rate effect is preserved for spheroids subjected to 200 vs. 50 mW cm^{-2} irradiations, which has been also observed experimentally (20). However, the revised dose calculations begin to indicate some possible limits to the quantitative predictions that can be made with a model based solely on $^3O_2$ consumption and transport considerations. For example, the dose curve computed for the case of 60 J cm^{-2} and a fluence rate of 25 mW cm^{-2} (Figure 2.10) suggests that a threshold dose of reacting $^1O_2$ is delivered throughout the spheroid, yet our cell survival data

indicate approximately 7% survival. Other factors not incorporated into the analysis, such as nonuniformities in light and/or sensitizer distribution, may contribute to this difference. Even though we have shown that the sensitizer is taken up by cells throughout the spheroid (Figure 2.1), local non-uniformities in drug uptake that would be extremely difficult to model could still exist. It is also critically important to acknowledge that the microelectrode experiments, from which the parameters are obtained that are used in the net photodynamic dose calculations, are performed under conditions that differ from those used in the spheroid cell survival experiments. In the latter, a group of spheroids (50, typically) are irradiated at the bottom of a 16 mm well, while the electrode measurements are performed on a single spheroid symmetrically supplied with $^3O_2$ from the surrounding media. Thus, the asymmetric $^3O_2$ supply and/or modest $^3O_2$ depletion of the bulk medium during irradiation of a group of spheroids could reduce the actual vs. the calculated photodynamic dose.

2.4.3 $^1O_2$-mediated photobleaching and the simple exponential decay description of sensitizer degradation

We have emphasized throughout this chapter that a self-sensitized, $^1O_2$-mediated photobleaching mechanism differs in several important ways from a phenomenological model expressed in terms of a simple exponential with a constant bleaching coefficient. The nature of this difference goes beyond the fact that the former involves an explicit $^3O_2$ dependence while the latter is usually written in terms of the total optical fluence. Indeed,

if this were the only distinction between the two models, one might anticipate that the

^{1}O$_2$- mediated bleaching theory would reduce to the simple exponential expression in the

limit of abundant ^{3}O$_2$. But this is not the case as is shown in the calculated photodynamic

dose plots of Figure 2.9. These results demonstrate that even near the edge of the

spheroid where ^{3}O$_2$ is clearly not limiting the rate of photobleaching, the two models

make different dose predictions. A second example of the qualitative difference between

the two bleaching models is illustrated in Figure 2.12, where again in a situation where

^{3}O$_2$ is not limiting, the self-sensitized, ^{1}O$_2$-mediated theory is able to adequately account

for the observed non-exponential fluorescence decay. The key element that distinguishes

the theory evaluated in this chapter from the simple exponential model is the dependence

of the agent responsible for bleaching on the availability of the photosensitizer itself. This

is apparent in the form of the bleaching term in Eq. 2.10, where the exponential involves

the time integral of the rate of photodynamic ^{3}O$_2$ consumption, which must decrease as

bleaching diminishes the rate of photon absorption. The loss of photosensitzer through

other possible photobleaching mechanisms may be described using a constant bleaching

coefficient. For example, if bleaching were the result of a photo-excited state reaction

with some biological target, the bleaching agent would be independent of the sensitizer

concentration, and the use of a simple exponential would characterize the loss of

sensitizer absorption. In the following chapter, we present an example of a sensitizer that

photobleaches *via* a mechanism that is not ^{1}O$_2$-mediated and can be described by a

constant bleaching coefficient expression. Nevertheless, even in this case, the *fluence-*

dependent simple exponential decay is not consistent with the observed $^3O_2$ concentration

changes.

2.4.4 The moving depletion zone boundary correction

While the emphasis of this study has been the mechanism of Photofrin® photobleaching,

a significant improvement to our model has been the explicit coupling of the depletion

zone radius, R_d, to the spatially averaged $^3O_2$ consumption within a spheroid during PDT.

Initially, we observed that it was not possible to obtain a good fit to the long-duration

(800 s), time-dependent microelectrode data using the depletion zone radius determined

from the steady-state measurement. In practice, it was necessary to treat this radius as a

free parameter during the fitting process. The fitted value of this quantity was always

greater than that measured with the electrode in the absence of irradiation, and this

suggested that the boundary was moving in response to the increased $^3O_2$ consumption

during PDT. The mathematical treatment of this moving boundary, as presented in

Appendix A, has provided a formal solution to this problem. Although excellent fits to the

earliest parts of the microelectrode data had been possible using the fixed depletion zone

radius measured from the steady-state experiment, incorporation of the more rigorous

moving boundary has shown that the previous treatment forced an underestimation of one

of the model parameters, the ratio k_p/k_{ot}, which is extracted from the fits to the early time

data. This parameter, which involves the ratio of the monomolecular sensitizer triplet

decay rate (k_p) to the rate at which the triplets are quenched by $^3O_2$ (k_{ot}), defines the

oxygen sensitivity of PDT. Using the fixed depletion zone radius and analyzing very early

electrode transients ($\leq$ 15 s), the value of this ratio was previously reported to be

approximately 2.2 μM (1). Fitting a larger data set of 40 s transients over a wider range

of fluence rates (40-100 mW cm^{-2}) yields an estimate of k_p/k_{ot} of 4.9 $\pm$ 0.8 μM (Table

2.1). Analysis of the same data under identical conditions except for the improved

treatment of the boundary results in a k_p/k_{ot} of 11.9 $\pm$ 2.2 μM, while the estimate of Γ_0 is

unchanged. The previous underestimation of k_p/k_{ot} probably resulted from the fact that

because the depletion zone boundary during irradiation was actually farther from the

spheroid than the R_d measured prior to the onset of irradiation, the $^3O_2$ concentration

measured by the electrode was lower for a given rate of consumption than it would have

been if R_d were in its original location. Since lowering k_p/k_{ot} will have the effect of

sustaining photochemical $^3O_2$ consumption and depleting the spheroid, the fitting

algorithm achieved the best agreement with the data by artifactually reducing its value.

The revised estimate of 11.9 μM is within experimental uncertainty of the k_p/k_{ot} reported

by Moan and Sommer (24) for HpD (13 μM) and farther from the value reported by

Chapman $et\ al.$ (25) for Photofrin$^{\circledR}$ (0.1% or approximately 1.1 μM).

2.4.5 Concluding remarks

In conclusion, a theory of $^1O_2$-mediated Photofrin$^{\circledR}$ photobleaching is consistent with

observations made in multicell spheroids, cells and cell-free media. The distinction between this theory and a model based on a constant bleaching coefficient has important ramifications on the spatial and temporal distribution of $^1O_2$ in multicell systems, even when $^3O_2$ is abundant. Our results are specific to Photofrin® photobleaching, and, as shown in the next chapter, different sensitizers may photobleach *via* different mechanisms. Finally, this work demonstrates the importance of including photobleaching in quantitative dosimetry models.

References

1.   Nichols, M.G. and T.H. Foster (1994) Oxygen diffusion and reaction kinetics in photodynamic therapy of multicell tumor spheroids. *Phys. Med. Biol.* **39**, 2161-2181.

2.   Mang, T.S., T.J. Dougherty, W.R. Potter, D.G Boyle, S. Somer and J. Moan (1987) Photobleaching of porphyrins used in photodynamic therapy and implications for therapy. *Photochem. Photobiol.* **45**, 501-506.

3.   Potter, W.R., T.S. Mang and T.J. Dougherty (1987) The theory of photodynamic therapy dosimetry: consequences of photodestruction of sensitizer. *Photochem. Photobiol.* **46**, 97-101.

4.   Mang, T.S. and T.J. Wieman (1987) Photodynamic therapy in the treatment of pancreatic carcinoma: dihematoporphyrin ether uptake and photobleaching

kinetics. *Photochem. Photobiol.* **46**, 853-858.

5. Moan, J., C. Rimington and Z. Malik (1988) Photoinduced degradation and
    modification of Photofrin II in cells *in vitro*. *Photochem. Photobiol.* **47**, 363-367.

6. Krieg, M. and D.G. Whitten (1984) Self-sensitized photo-oxidation of
    protoporphyrin IX and related porphyrins in erythrocyte ghosts and micro-
    emulsions: a novel photo-oxidation pathway involving singlet oxygen. *J.
    Photochem.* **25**, 235-252.

7. Krieg, M. and D.G. Whitten (1984) Self-sensitized photooxidation of
    protoporphyrin IX and related free-base porphyrins in natural and model
    membrane systems. Evidence for novel photooxidation pathways involving amino
    acids. *J. Am. Chem. Soc.* **106**, 2477-2479.

8. Moan, J. and D. Kessel (1988) Photoproducts formed from Photofrin II in cells.
    J. Photochem. Photobiol. B: Biol. **1**, 429-436.

9. Moan, J. and K. Berg (1991) The photodegradation of porphyrins in cells can be
    used to estimate the lifetime of singlet oxygen. *Photochem. Photobiol.* **53**,
    549-553.

10. Spikes, J.D. (1992) Quantum yields and kinetics of the photobleaching of hemato-
    porphyrin, Photofrin II, tetra(4-sulfonatophenyl)-porphine and uroporphyrin.
    Photochem. Photobiol. **55**, 797-808.

11. Mueller-Klieser, W. (1984) Method for the determination of oxygen consumption

rates and diffusion coefficients in multicellular spheroids. *Biophys. J.* **46**, 343-348.

12.   Wilson, D.F., C.S. Owen and M. Erecińska (1979) Quantitative dependence of mitochondrial oxidative phosphorylation on oxygen concentration: a mathematical model. *Arch. Biochem. Biophys.* **195**, 494-504.

13.   Wilson, D.F., W.L. Rumsey, T.J. Green and J.M. Vanderkooi (1988) The oxygen dependence of mitochondrial oxidative phosphorylation measured by a new optical method for measuring oxygen concentration. *J. Biol. Chem.* **263**, 2712-2718.

14.   Oshino, N., T. Sugano, R. Oshino and B. Chance (1974) Mitochondrial function under hypoxic conditions: the steady states of cytochrome $a+a_3$ and their relation to mitochondrial energy states. *Biochim. Biophys. Acta* **368**, 298-310.

15.   Nichols, M.G. (1996) *Transport of oxygen and light in model tumor systems.* Doctoral dissertation, University of Rochester, Rochester, NY.

16.   Nichols, M.G. and T.H. Foster (1994) Microelectrode measurements of photochemical oxygen depletion in multicell tumor spheroids during photo-dynamic therapy. *Proc. SPIE* **2133**, 260-271.

17.   Crank, J. (1975) *The mathematics of diffusion.* New York: Oxford University Press, 137-159.

18.   Press, W.H., S.A. Teukolsky, W.T. Vetterling and B.P. Flannery (1992) *Numerical recipes in C.* Cambridge University Press, New York, NY.

19.   Moan, J. (1990) On the diffusion length of singlet oxygen in cells and tissues. *J.*

Photochem. Photobiol. B: Biol. **6**, 343-348.

20. Foster, T.H., D.F. Hartley, M.G. Nichols and R. Hilf (1993) Fluence rate effects in photodynamic therapy of multicell tumor spheroids. *Cancer Res.* **53**, 1249-1254.

21. Moan, J. (1986) Effect of bleaching of porphyrin sensitizers during photodynamic therapy. *Cancer Lett.* **33**, 45-53.

22. Moan, J. (1988) A change in the quantum yield of photoinactivation of cells observed during photodynamic treatment. *Lasers Med. Sci.* **3**, 93-97.

23. Farrell, T.J., B.C. Wilson, M.S. Patterson and R. Chow (1991) The dependence of photodynamic threshold dose on treatment parameters in normal rat liver in vivo. *Proc. SPIE* **1246**, 146-155.

24. Moan, J. and S. Sommer (1985) Oxygen dependence of the photosensitizing effect of hematoporphyrin derivative in NHIK 3025 cells. *Cancer Res.* **45**, 1608-1610.

25. Chapman, J.D., C.C. Stobbe, M.R. Arnfield, R. Santus, J. Lee and M.S. McPhee (1991) Oxygen dependency of tumor cell killing in vitro by light-activated Photofrin II. *Radiat. Res.* **126**, 73-79.

Chapter 3

Singlet Oxygen- Versus Non-Singlet Oxygen-Mediated Mechanisms of Sensitizer Photobleaching and Their Effects on Photodynamic Dosimetry

3.1 Introduction

In the previous chapter we evaluated a theory based on a $^1O_2$-mediated mechanism of sensitizer degradation and compared it to a fluence-dependent phenomenological description of photobleaching. In this chapter we present a theoretical model for the description of non-$^1O_2$-mediated photobleaching resulting from irreversible reactions of

the excited singlet or triplet sensitizer populations with cell substrate. We show that the fluence-dependent simple exponential decay expression of sensitizer degradation is not consistent with these mechanisms and, therefore, with any reasonable mechanism that we consider, since we have shown in the previous chapter that $^1O_2$-mediated photobleaching cannot be described by a simple exponential with a constant photobleaching coefficient. Analysis of $^3O_2$ concentration measurements and cell survival assays with EtNBSe- and δ-aminolevulinic acid (ALA) induced PpIX-sensitized spheroids during PDT demonstrates that the former drug photobleaches *via* a non-$^1O_2$-mediated mechanism, while the latter is degraded *via* a $^1O_2$-mediated mechanism. We discuss the implications of $^1O_2$- and non-$^1O_2$-mediated photobleaching for PDT dosimetry and we demonstrate that the mechanism *via* which the sensitizer degrades can affect the outcome of the therapy significantly in an $^3O_2$-limited environment.

3.2 $^1O_2$- and non-$^1O_2$-mediated descriptions of sensitizer photobleaching

3.2.1 Fluence-dependent simple exponential decay description of sensitizer photobleaching

As mentioned in the previous chapter, for the fluence-dependent simple exponential decay description, photobleaching occurs uniformly throughout the spheroid at a constant rate, α, and the rate of photodynamic oxygen consumption, Γ_{PDT} is written

$$\Gamma_{PDT}(t) = \Gamma_0 \left(\frac{k_{ot}[^3O_2](t)}{k_{ot}[^3O_2](t) + k_p} \right) \exp(-\alpha D).$$ (3.1)

(For term definition please refer to the List of Symbols on page xxi). The constant photobleaching coefficient implies the mechanistic assumption that the chemical species responsible for photobleaching does not depend on the photosensitizer for its formation.

3.2.2 Sensitizer photobleaching resulting from reactions of excited singlets with cell substrate

An energy level diagram depicting the primary photochemical reactions for this type of sensitizer degradation is shown in Figure 3.1a. The rate of change of the sensitizer excited singlet population is written

$$\frac{d[S_1]}{dt} = I_a(t) - k_m[S_1] - k_{isc}[S_1] - k_{as}[A][S_1],$$ (3.2)

where k_{as} is the bimolecular rate constant for the reaction between S_1 and cell substrate A. The observed e-folding light dose for EtNBSe (i.e. the light dose required to decrease the concentration of EtNBSe by approximately 37%) is 28 J cm^{-2} which is delivered in 140 s for a 200 mW cm^{-2} irradiation. Therefore, photobleaching occurs much slower than the primary photochemistry, and only the last term of Eq. 3.2 contributes to the loss of singlet sensitizer concentration on time scales relevant to photobleaching. Thus, Eq. 3.2
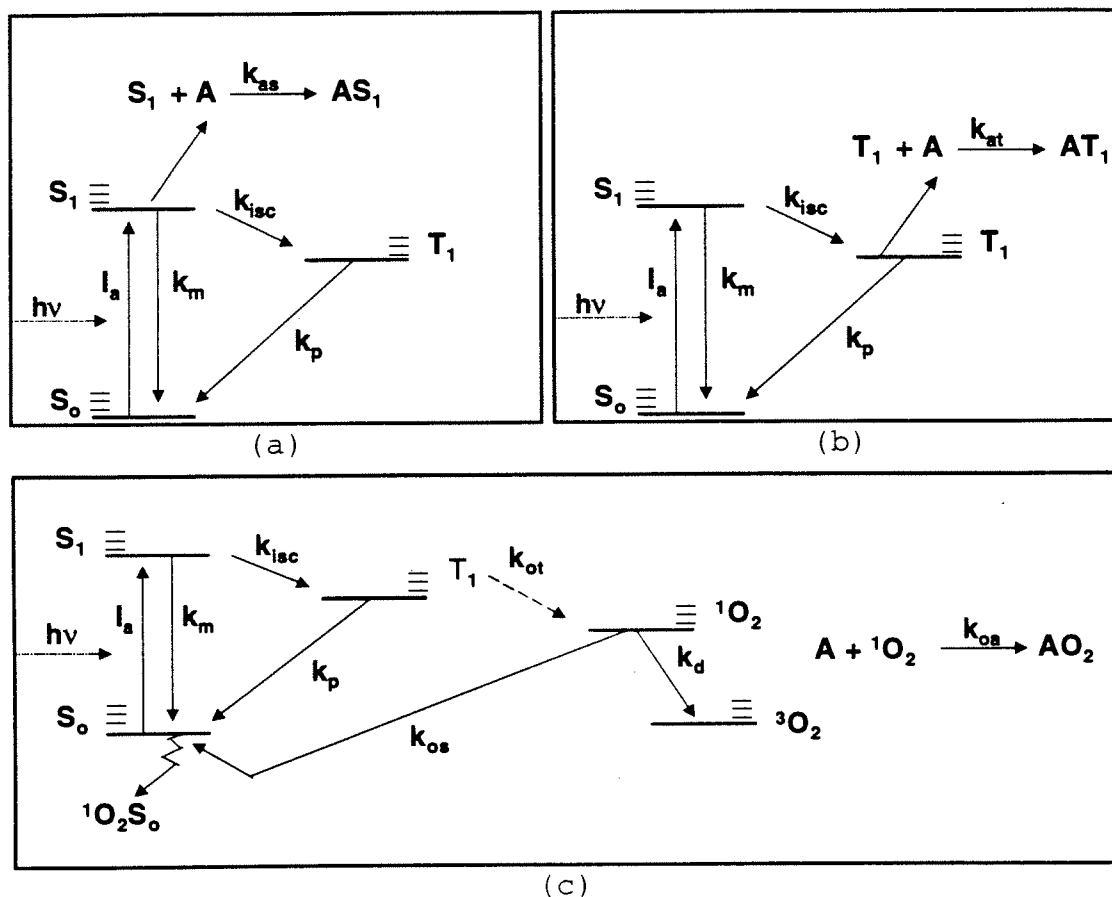
Figure 3.1: Energy level diagrams depicting the three different mechanisms of sensitizer photobleaching that we consider. In panel (a) the sensitizer is degraded *via* interactions between dye molecules in the excited singlet state, S_1, and cell substrates, denoted collectively as A, while in panel (b) sensitizer loss is the result of reactions between dye molecules in the excited triplet state, T_1, and cell substrate, A. These two non-^{1}O$_2$-mediated mechanisms can be compared with the third scheme of sensitizer degradation according to which ^{1}O$_2$ participates in irreversible reactions with sensitizer molecules in the ground state, S_0 (panel (c)).

can be reduced to

$$\frac{d[S_1]}{dt} = -k_{as}[A][S_1],$$
(3.3)

which yields

$$[S_1](t) = [S_1]_{(t=0)}\exp(-k_{as}[A]t).$$
(3.4)

As in the previous case, the loss of sensitizer is expressed as a simple exponential decay with a constant photobleaching coefficient. Here, however, bleaching is exponential in the *time* rather than the *fluence*. Thus, Γ_{PDT} for the case of drug degradation through excited singlet sensitizer reactions with cell substrate is expressed as

$$\Gamma_{PDT}(t) = \Gamma_0\left(\frac{k_{ot}[^3O_2](t)}{k_{ot}[^3O_2](t)+k_p}\right)\exp\left(-k_{as}[A]t\right).$$
(3.5)

Only the exponential term is incorporated in Γ_{PDT}, since $[S_1]_{(t=0)}$ is included indirectly in Γ_0 via I_a.

3.2.3 Sensitizer photobleaching resulting from reactions of excited triplets with cell substrate

The main photochemical processes for this case are depicted in Figure 3.1b. The

derivation of an expression that describes photobleaching resulting from reactions between excited triplet sensitizer molecules and cell substrate requires a modification to include the dependence of $[T]$ on $[^3O_2]$. We begin with the rate equation for the triplet sensitizer population:

$$\frac{d[T]}{dt} = k_{isc}[S_1] - k_p[T] - k_{ot}[T][^3O_2] - k_{at}[T][A],$$
(3.6)

where k_{at} is the bimolecular rate constant for reaction between T and cell substrate, A, that results in loss of sensitizer. The triplet concentration at a given time t can be expressed as

$$[T](t) = \frac{k_{isc}[S_1](t)}{k_{ot}[^3O_2](t) + k_p + k_{at}[A]} .$$
(3.7)

We note that the photobleaching constant $k_{at}[A]$ is considerably smaller than k_p. Thus, we may write Eq. 3.7 as

$$[T](t) = \frac{k_{isc}[S_1](t)}{k_{ot}[^3O_2](t) + k_p} .$$
(3.8)

Further, on time scales relevant to photobleaching, Eq. 3.6 may be written to describe the irreversible loss of triplets as

$$\frac{d[T]}{dt} = -k_{at}[T][A],$$
(3.9)

which yields

$$[T](t) = [T]_{(t=0)}\exp\left(-k_{at}[A]t\right).$$ (3.10)

Unlike the excited singlet situation, the concentration of sensitizer triplets available to participate in bleaching reactions depends on the $^3O_2$ concentration, which in general is changing in space and time. For this reason, it is not possible to express the loss of sensitizer in terms of some initial triplet concentration, $[T]_{(t=0)}$. We can, however, write

$$[T](t) = [T]_{(t-\Delta t)}\exp\left(-k_{at}[A]\Delta t\right),$$ (3.11)

where Δt is a time increment sufficiently short that the $^3O_2$ concentration has not changed significantly (Δt is also the time-step used for the implementation of the numerical solutions to the oxygen diffusion with consumption equations (Appendix B)). After combining Eqs. 3.8 and 3.11 we obtain for the concentration of the triplet population at time t:

$$[T](t) = \frac{k_{isc}[S_1]}{k_{ot}[^3O_2]_{(t-\Delta t)} + k_p}\exp\left(-k_{at}[A](t)\right).$$ (3.12)

To incorporate these time-dependent changes of $[T]$ in our expression for Γ_{PDT}, we need to rewrite Eq. 3.12 in the form

$$[T](t) = [T]_{(t=0)}*X(t),$$ (3.13)

since $[T]_{(t=0)}$ is indirectly incorporated in Γ_0. After dividing $[T](t)$ (Eq. 3.12) by $[T]_{(t=0)}$ (Eq. 3.8) we find that the function $X(t)$ is equal to:

$$X(t) = \frac{k_p + k_{ot}[^3O_2]_{(t=0)}}{k_p + k_{ot}[^3O_2]_{(t-\Delta t)}} \exp\left(-k_{at}[A]t\right). \tag{3.14}$$

Therefore, triplet sensitizer photobleaching resulting from its reaction with ^{1}O$_2$-independent cell substrates is incorporated in Γ_{PDT} in the following way:

$$\Gamma_{PDT}(t) = \Gamma_0\left(\frac{k_{ot}[^3O_2](t)}{k_{ot}[^3O_2](t) + k_p}\right)\left(\frac{k_p + k_{ot}[^3O_2]_{(t=0)}}{k_p + k_{ot}[^3O_2]_{(t-\Delta t)}}\right) \exp\left(-k_{at}[A]t\right). \tag{3.15}$$

3.2.4 ^{1}O$_2$-mediated sensitizer photobleaching

Under the fourth scheme that we consider, depicted as an energy level diagram in Figure 3.1c, sensitizer degradation is the result of direct reaction between ground state sensitizer and ^{1}O$_2$. As such, photobleaching is a non-uniform process, confined to the spheroid regions where significant amounts of ^{1}O$_2$ are produced. In this case, Γ_{PDT} is

$$\Gamma_{PDT}(t) = \Gamma_0\left(\frac{k_{ot}[^3O_2](t)}{k_{ot}[^3O_2](t) + k_p}\right)\exp\left(-\frac{k_{os}}{k_{oa}[A]}\int_0^t \Gamma_{PDT}(t')dt'\right). \tag{3.16}$$

The derivation of this expression was described briefly in the previous chapter. The ^{1}O$_2$-mediated photobleaching theory is developed in detail elsewhere (1, 2).

3.3 Effects of sensitizer localization and redistribution on

the maximum rate of photodynamic ^{3}O$_2$ consumption

The uniformity of sensitizer uptake by EMT6 spheroids is tested using the procedure

described for Photofrin®-sensitized spheroids (section 2.3.1). In this case, spheroids are

incubated with 1.5 μM EtNBS for 30 minutes. This incubation protocol is based on

sensitizer uptake and toxicity studies performed with monolayer cultures (3) and EMT6

spheroids (Appendix C). Following incubation, the spheroids are washed, frozen, and

sectioned as described previously. The exposure time for obtaining the fluorescence

images of the EtNBS-sensitized spheroid sections with the CCD camera is only 50 ms.

As shown in Figure 3.2a, the uptake of EtNBS is not uniform across a spheroid

section. Specifically, we observe that the fluorescence intensity decreases significantly

from the edge to the center of a spheroid. No fluorescence is observed when unsensitized

spheroid sections are imaged under identical conditions, indicating that the fluorescence

signal that we observe originates from EtNBS (Figure 3.2b). In an attempt to quantify this

non-uniformity we analyze fluorescence intensity cross-sections through the center of 12

spheroid sections varying from 230 to 470 μm in diameter, similar to the one shown in

Figure 3.3. A monoexponential decay function ($y=A*exp(-x/\theta)$) is fit to the left half of

each intensity cross-section and a monoexponential growth function ($y=A*exp(x/\theta)$) is

fit to the corresponding right half (y is the fluorescence intensity, x is the radial distance

from the edge or the center of the spheroid for the decay and growth functions,

(a)

(b)

Figure 3.2: Fluorescence images (640x512 pixels) of a 6 μm frozen section from a spheroid incubated with 1.5 μM EtNBS for 30 min (a) and a spheroid not sensitized with any drug (b), demonstrating that the signal detected in panel (a) is EtNBS fluorescence. The non-uniformity in EtNBS uptake by the spheroid cells for the particular incubation protocol is evident. The field of view in the horizontal direction is 700 μm. The images are obtained with a CCD camera attached to a fluorescence microscope. The exposure time is 50 ms.
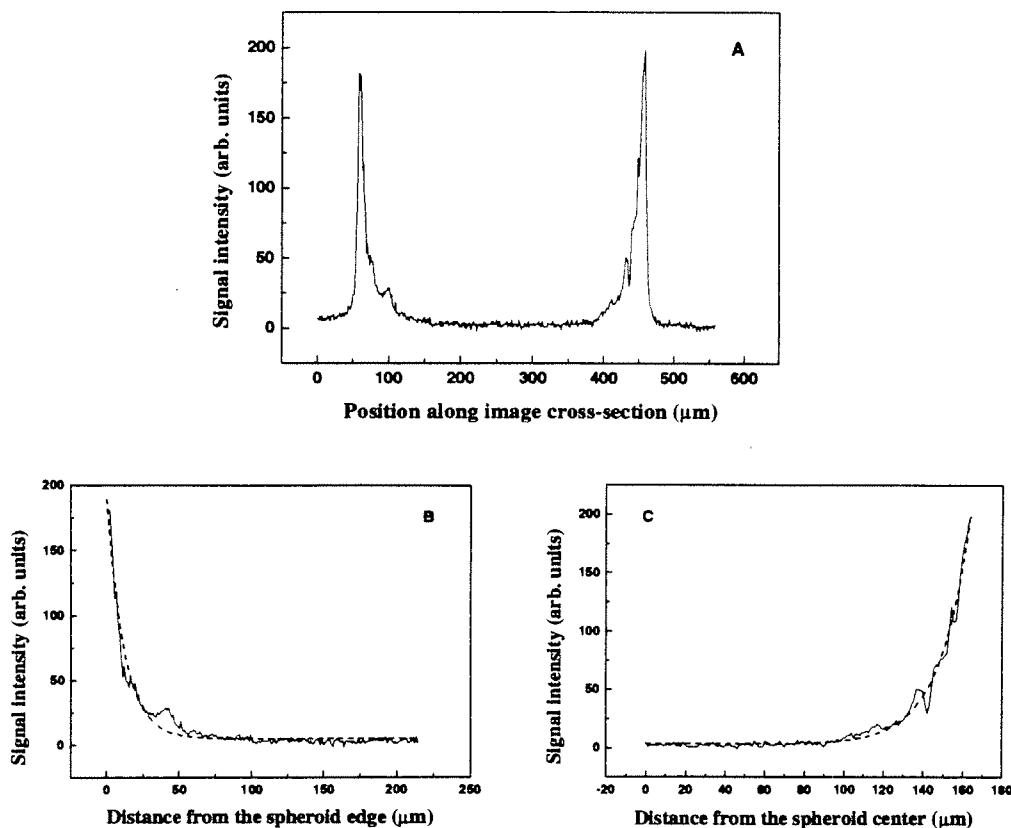
Figure 3.3: The fluorescence intensity cross-section through the image of a 6 μm section

from a spheroid (~ 410 μm in diameter) incubated with 1.5 μM EtNBS for 30 min (panel

(A)) demonstrates that EtNBS is taken up by the spheroid cells non-uniformly. A mono-

exponential decay or growth function is fit to the left or right half of the intensity cross-

section, respectively (panels (B) and (C)). The data are portrayed by the solid lines, while

the dashed lines represent the best fits. After analyzing the intensity cross-sections

through 12 spheroids varying from 230 to 470 μm in diameter, we find that the charac-

teristic constant of the rate at which the intensity varies with distance is 16.8 ± 5.8 μm^{-1}.

respectively, and θ is the constant characteristic of the rate at which the intensity varies

with distance). From these fits we find that the constant θ is 16.8 ± 5.8 μm^{-1}. We note

that monoexponential decay and growth functions describe the fluorescence intensity

profiles better than bi-exponential ones.

These non-uniformities in sensitizer uptake affect the maximum rate of

photodynamic oxygen consumption, Γ_0, that can be achieved for a specific fluence rate

of irradiation at a particular radial distance from the center of the spheroid. Therefore, the

expression for Γ_0 used for analysis of Nile Blue-sensitized spheroids is written

$$\Gamma_0^{mod}(r) = \Gamma_0' \exp\left(-(r-R_s)/\theta\right),$$ (3.17)

where Γ_0' is given by our previous definition for the maximum rate of photodynamic

oxygen consumption,

$$\Gamma_0' = S_\Delta \varphi_t I_a \left(\frac{k_{oa}[A]}{k_d + k_{oa}[A]} \right),$$ (3.18)

and r is radial distance from the center of the spheroid. We use the value of the constant

θ determined for the EtNBS-sensitized frozen spheroid sections when we analyze the

time-dependent ^{3}O$_2$ concentration distributions recorded during irradiation of EtNBSe-

sensitized spheroids, since the two sensitizers are very similar in terms of their size and

hydrophilicity properties. It would be rather difficult to perform uniformity uptake studies

with EtNBSe because the fluorescence yield of this sensitizer is much lower than that of

EtNBS.

As described in detail in the following chapter, the Nile Blue sensitizers undergo

a rapid intracellular redistribution during irradiation. This relocalization process leads to

the observation of two distinct phases of photodynamic ^{3}O$_2$ consumption. To describe the

second oxygen consumption phase, Γ_0 is modified further by a sigmoid function such that

$$\Gamma_0(r) = \Gamma_0^{mod}(r)\left(1 + C\frac{(t-t_i)^n}{(t_{50}-t_i)^n + (t-t_i)^n}\right), \qquad (3.19)$$

where $\Gamma_0^{mod}(r)$ is the radially dependent maximum rate of photodynamic ^{3}O$_2$ consumption

during the first ^{3}O$_2$ consumption step, defined by Eq. 3.17, C is a scaling factor describing

the relative magnitude of the second ^{3}O$_2$ consumption step, t is time from the onset of

irradiation, t_i is the time at which the second ^{3}O$_2$ consumption phase begins, t_{50} is the time

at which $\Gamma_o(r)$ achieves a value that is half way between $\Gamma_0^{mod}(r)$ and its maximum, and

n is a parameter that describes, along with t_{50}, how fast $\Gamma_o(r)$ changes as a function of

time (4).

For the experiments performed with ALA-induced PpIX-sensitized spheroids, we

assume that ALA is taken up uniformly by the spheroid cells, leading to uniform PpIX

synthesis. As ALA is a small molecule that is readily taken up by cells, this assumption

should be valid for the 24 h incubation protocol used in these studies. Since we observe

only one phase of photodynamic ^{3}O$_2$ consumption during PpIX-PDT, we use the time and

space invariant form of Γ_0, given by Eq. 3.18, during analysis of time-dependent ^{3}O$_2$

concentration distributions recorded during irradiation of PpIX-sensitized spheroids.

3.4 Experimental results and analysis

3.4.1 Oxygen microelectrode measurements with EtNBSe-sensitized spheroids

The experimental apparatus used to obtain the $^3O_2$ microelectrode measurements has been described in detail in the previous chapter. For the EtNBSe photobleaching studies, a single EMT6/R$_o$ spheroid (approximately 500 μm in diameter) is incubated for 30 minutes in a 60 mm tissue culture dish with 4 mL of HBSS containing 1.5 μM EtNBSe at 37°C in a humidified 5% CO_2-95% air atmosphere (Stock solutions (30 μM) of EtNBSe and EtNBS are prepared by dilution of the sensitizer, provided in powder lyophilized form, in HBSS). Following incubation, under conditions of minimal illumination, the spheroid is placed atop the oxygen permeable membrane of a pedestal immersed in an open dish that contains 20 mL HBSS. A glass micropipette (8 μm outer diameter) is used to hold the spheroid in place.

In the absence of irradiation, we record the $^3O_2$ concentration from the spheroid center to the depletion zone radius in 20 μm increments, using a Clark-style oxygen microelectrode with an outer tip diameter of 5 μm (Diamond General, Ann Arbor, MI). Subsequently, we position the microelectrode tip at the spheroid edge, and we record the changes in $^3O_2$ concentration that occur at this location during irradiation at 50, 100, or 200 mW cm^{-2} with light from a 662 nm diode laser (Applied Optronics, South Plainfield, NJ). The $^3O_2$ concentration decreases rapidly upon the onset of irradiation; however, as

sensitizer photobleaches, ^{3}O$_2$ consumption is reduced and we observe a concomitant, gradual increase in ^{3}O$_2$ concentration.

To determine the sensitizer photobleaching mechanism and rate, we fit the entire time-dependent electrode recording using one of equations 3.5, 3.15, or 3.16 to determine $k_{as}[A]$, $k_{at}[A]$ or $k_{os}/k_{oa}[A]$, respectively. During these fits, the time invariant component of the maximum rate of photodynamic ^{3}O$_2$ consumption, $\Gamma_0^{mod}(r)$, the ratio k_p/k_{ot}, and one of the parameters describing how fast the ^{3}O$_2$ concentration changes during the second step of ^{3}O$_2$ consumption, t_{50}, are allowed to vary also. The results obtained when the fluence-dependent simple exponential decay description of photobleaching (Eq. 3.1) is used are compared with those of the photobleaching mechanisms involving the excited singlets and triplets.

It is mentioned in section 3.3 that our expression for the maximum rate of photodynamic ^{3}O$_2$ consumption is modified in this report to describe ^{3}O$_2$ consumption occurring in two phases (Eq. 3.19). The relocalization of EtNBSe from the lysosomal to the cytosolic milieu results in a second wave of ^{3}O$_2$ consumption, the onset of which is fluence dependent (chapter 4, ref. (4)). Enhanced photodynamic action upon redistribution to the cytosol has been observed with other lysosomal sensitizers (5-7). The incorporation of this two-step ^{3}O$_2$ consumption event in our model of ^{3}O$_2$ diffusion with consumption leads to significantly improved fits to the recorded time-dependent ^{3}O$_2$ concentrations and to more accurate determination of the photobleaching coefficient. An example of this improvement is shown in Figure 3.4 for a profile obtained during a 100 mW cm^{-2} irradiation.
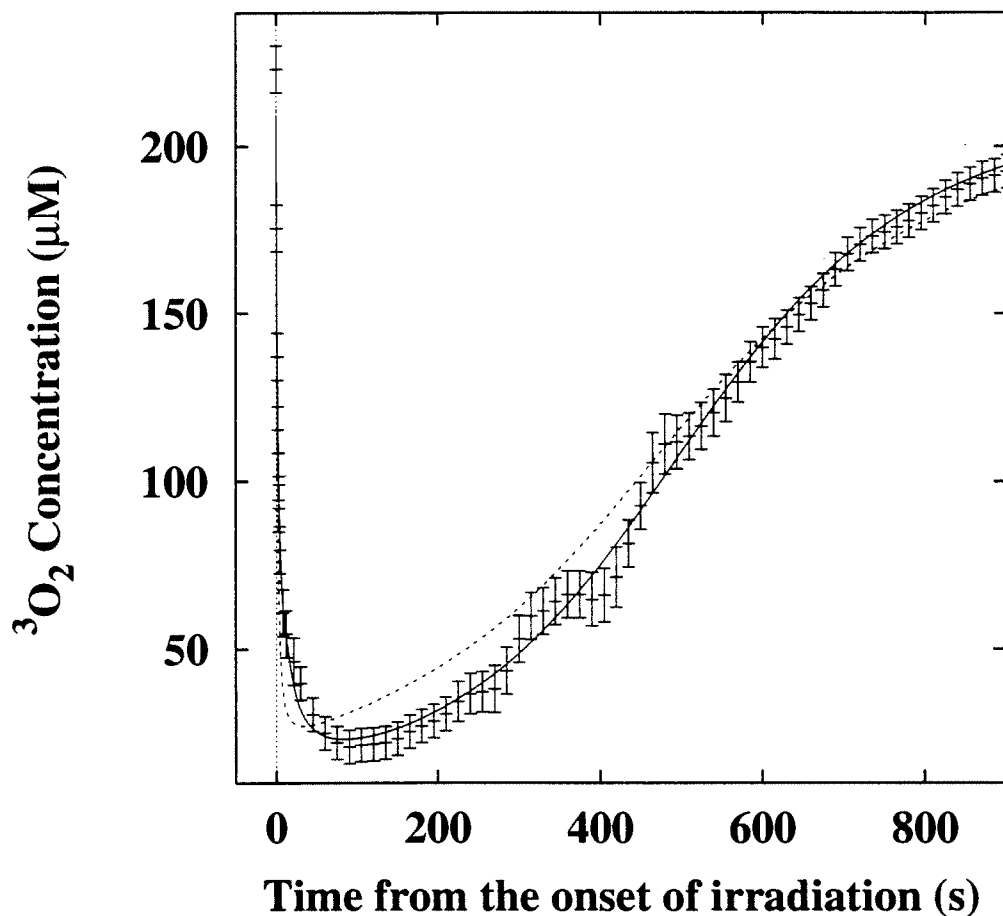
Figure 3.4: Improvement in the fit of Eq. 3.15 to the time-dependent ^{3}O$_2$ concentrations

recorded during PDT of EtNBSe-sensitized spheroids when Γ_0 is modified to account for

the two phases of ^{3}O$_2$ consumption (Eq. 3.19;————); the second phase occurs when

EtNBSe is redistributed from the lysosomes into the cytosol. The best fit achieved when

^{3}O$_2$ consumption is treated as a one-step process (Eq. 3.17) is shown for comparison

(- - - -).

A typical example of the changes in $^3O_2$ concentration that we record at the edge

of an EtNBSe-sensitized spheroid during irradiation delivered at 200 mW cm^{-2} is shown

in Figure 3.5. The solid line in Figure 3.5a represents the best fit obtained when

photobleaching kinetics are described by Eq. 3.15, $i.e.$ by photobleaching that involves

the triplet sensitizer. In this case, the theoretical model describes with excellent agreement

the changes in $^3O_2$ consumption that we observe as a result of sensitizer degradation. In

contrast, when we assume a $^1O_2$-mediated photobleaching mechanism (Equation 3.16) the

theory cannot describe adequately the experimentally determined time-dependent $^3O_2$

concentrations, as can be seen in Figure 3.5b. Along with the best fit achieved when

Equation 3.16 is used for data analysis (k_{os}/k_{oa} [A] = 118 ± 1 M^{-1}), we plot a family of

simulated curves for values of k_{os}/k_{oa} [A] equal to 50, 250, and 450 M^{-1} to demonstrate

the inability of this expression to describe the measured $^3O_2$ concentration changes over

a wide range of this parameter. The expression based on a triplet sensitizer reaction

mechanism describes the recorded $^3O_2$ distributions more accurately than the $^1O_2$-mediated

photobleaching expression consistently for EtNBSe-sensitized spheroids irradiated with

200, 100 and 50 mW cm^{-2}. From eight experiments performed at the above mentioned

fluence rates we find that the photobleaching coefficient, k_{at} [A], is 0.0058 ± 0.0009 s^{-1}.

As shown in Figure 3.6a, the expression for Γ_{PDT} (t) describing sensitizer loss

resulting from the reactions of excited singlet drug molecules with cell substrate, Eq. 3.5,

is equally successful in describing the same data. Therefore, analysis of the time-

dependent $^3O_2$ concentration distributions does not allow discrimination between the

(a)

(b)
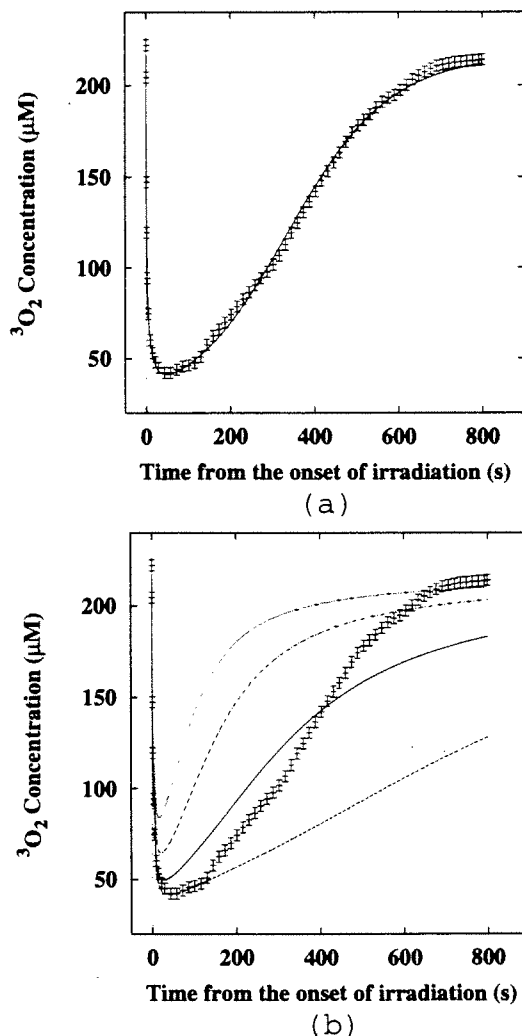
Figure 3.5: Comparison of ^{1}O$_2$- and non-^{1}O$_2$-mediated photobleaching mechanisms for

the analysis of time-dependent ^{3}O$_2$ concentrations recorded during irradiation of EtNBSe-

sensitized spheroids (200 mW cm^{-2}, 662 nm). Shown are the best fits (———) achieved

when photobleaching is the result of (a) triplet reactions with cell substrate (Eq. 3.15) or

(b) ^{1}O$_2$ reactions with ground-state sensitizer (Eq. 3.16). To emphasize the inability of the

^{1}O$_2$-mediated expression to describe the data, a family of curves is shown in (b) for

k_{os}/k_{oa}[A] of 50 (- - -), 118 (——— ; best fit), 250 (- · · · -), and 450 (· · · ·) M^{-1}.

photobleaching mechanisms that involve excited singlet and triplet sensitizer reactions. However, when we compare the changes in $^3O_2$ concentration that occur during 200 mW cm^{-2} irradiation of EtNBSe- and EtNBS-sensitized spheroids we observe that EtNBSe degradation occurs much faster for a comparable number of absorbed photons (Figure 3.6b). The two dyes have similar extinction coefficients at 662 nm (ε_{NBSe} = 79,824; ε_{NBS} = 65,130), and dye extraction studies indicate that similar amounts of EtNBSe and EtNBS are taken up by the spheroid cells when treated with the same sensitizer incubation protocol (4). However, the heavy atom effect produces higher triplet yields for EtNBSe than for EtNBS. These differences are reported indirectly by the $^1O_2$ yields for the two compounds (0.025 for EtNBS and 0.65 for EtNBSe) (3). Therefore, we expect lower excited singlet and higher excited triplet populations for EtNBSe than for EtNBS. The significantly larger photobleaching constant for EtNBSe than for EtNBS is consistent with the hypothesis that it is mainly the triplet sensitizer population that participates in irreversible photobleaching reactions with cell substrate.

As shown in Figure 3.7, preliminary studies demonstrate that a non-$^1O_2$-mediated photobleaching mechanism is consistent with the $^3O_2$ concentration changes recorded during irradiation of EtNBS-sensitized spheroids also. The best fit to the data achieved when we consider the mechanism involving reactions of excited triplets with cell substrate, Eq. 3.15, is shown. In this case, the fitted value for the bleaching coefficient, $k_{at}[A]$, is 0.0038 s^{-1}, significantly lower than that for EtNBSe.
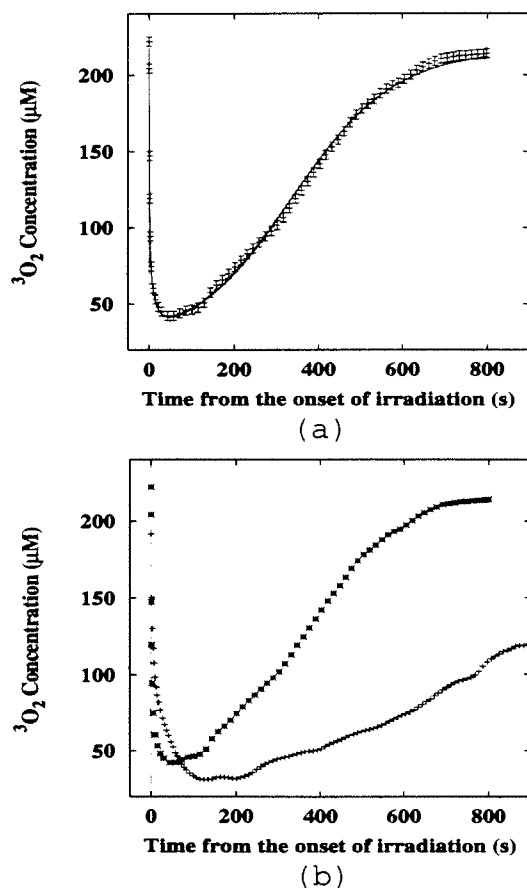
Figure 3.6: Differences between the sensitizer photobleaching mechanisms that involve

excited singlets (Eq. 3.5; - - -) and triplets (Eq. 3.15; ——) cannot be discerned simply

by analysis of photodynamically induced ^{3}O$_2$ concentration changes. In (a) are the best fits

to an ^{3}O$_2$ distribution recorded during a 200 mW cm^{-2} irradiation (662 nm) when the two

mechanisms are considered (Lines overlap). In (b), the changes in ^{3}O$_2$ concentration

resulting from sensitizer photobleaching during PDT (200 mW cm^{-2}) of spheroids

sensitized with the same concentrations of EtNBSe (✳ ✳ ✳) and EtNBS (+ + +) show

that EtNBSe is degraded at a significantly faster rate than EtNBS, consistent with the

hypothesis that the excited triplet population is the principal species involved in sensitizer

degradation.
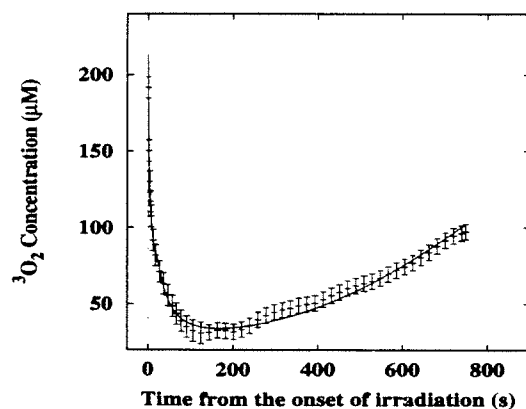
Figure 3.7: A non-^{1}O$_2$-mediated photobleaching mechanism is consistent with the changes in ^{3}O$_2$ concentration observed during irradiation of EtNBS-sensitized spheroids (200 mW cm^{-2}, 662 nm). Shown is the best fit (———) achieved when photobleaching is the result of triplet reactions with cell substrate (Eq. 3.15).

3.4.2 Oxygen microelectrode measurements with PpIX-sensitized spheroids

Results are also reported from microelectrode experiments performed with spheroids incubated for approximately 24 h with 4 mL BME (Gibco-BRL) containing 1 mM δ-ALA (Sigma Chemical Co., St. Louis, MO). The protocol followed was similar to the one described above; however, in this case, irradiation was performed with 514 nm light from an argon-ion laser (Ion Laser Technology, Salt Lake City, UT) delivered to the spheroids at 82 mW cm^{-2} *via* an optical fiber.

To illustrate the fundamental differences in the patterns of ^{3}O$_2$ consumption that result when sensitizer photobleaches *via* a ^{1}O$_2$-mediated mechanism, we show in Figure 3.8 the time-dependent ^{3}O$_2$ distributions recorded at the edge of a δ-ALA induced PpIX-sensitized spheroid irradiated with 514 nm light at 82 mW cm^{-2}. In this case, while the ^{1}O$_2$-mediated photobleaching expression (Equation 3.16) describes with excellent agreement the observed ^{3}O$_2$ concentration changes (Figure 3.8a), the photobleaching expressions involving excited singlet and triplet sensitizer fail to do so. This is demonstrated by a family of curves, shown in Figure 3.8b, generated using Equation 3.5 with k_{as} [A] equal to 0.0016, 0.0025, 0.0033, and 0.0041 s^{-1}. Similar ^{3}O$_2$ concentration profiles are obtained when we use the expression describing sensitizer loss as a result of triplet sensitizer interactions (Equation 3.15) (Data not shown). From five experiments we find that k_{os}/k_{oa} [A] = 90 ± 15.9 M^{-1} for δ-ALA induced PpIX photobleaching, a value not statistically different from that of Photofrin® (k_{os}/k_{oa} [A] = 76 ± 12 M^{-1}; (2)).
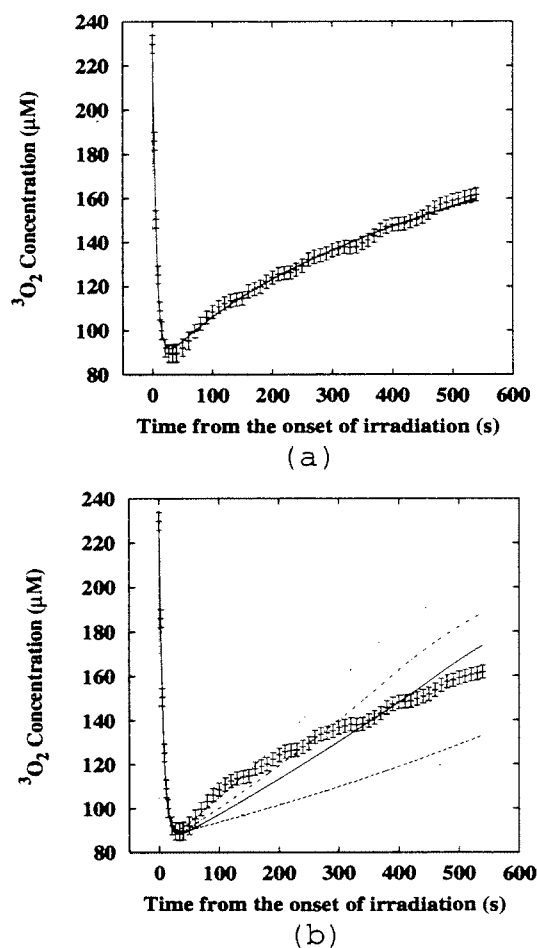
Figure 3.8: In contrast to EtNBSe, ALA-induced PpIX photobleaches *via* a ^{1}O$_2$-mediated

mechanism. Shown is a typical ^{3}O$_2$ concentration distribution recorded during an 82 mW

cm^{-2} irradiation (514 nm) of a spheroid incubated with 1 mM ALA for 24 h with the best

fits (solid lines) achieved when we consider photobleaching involving (a) ^{1}O$_2$ reactions

with ground-state sensitizer (Eq. 3.16) and (b) excited singlet sensitizer reactions with cell

substrate (Eq. 3.5). A family of curves for k_{as} [A] of 0.0016 (- - -), 0.0025 (———— ; best

fit), 0.0033 (- · - · -), and 0.0041 s^{-1} (· · · ·) is shown to demonstrate the fundamental

differences between the data and the non-^{1}O$_2$-mediated photobleaching model.

3.4.3 ^{1}O$_2$- and non-^{1}O$_2$-mediated sensitizer photobleaching in photodynamic dosimetry

In Figure 3.9 we demonstrate the importance of distinguishing between ^{1}O$_2$- and non-^{1}O$_2$-mediated photobleaching mechanisms for photodynamic dosimetry. Plotted are simulated net photochemical ^{3}O$_2$ consumption curves throughout an EtNBSe-sensitized spheroid irradiated with 100 J cm^{-2} at a rate of 200 mW cm^{-2}. For each one of the simulations, we use the best fit value of α, $k_{as}[A]$, $k_{at}[A]$ or $k_{os}/k_{oa}[A]$ obtained when Eqs. 3.1, 3.5, 3.15, and 3.16 are used, respectively, to analyze an ^{3}O$_2$ distribution acquired for such an irradiation. To illustrate the differences that are fundamental to the photobleaching mechanisms, we assume for these simulations that the drug is distributed uniformly throughout the spheroid and adjust the maximum rate of photodynamic ^{3}O$_2$ consumption accordingly. Given the small distance (less than 70 nm) that ^{1}O$_2$ diffuses before it reacts with substrate (8, 9), the curves shown in Figure 3.9 are equivalent to the ^{1}O$_2$ distributions that would be deposited in the spheroid. For the ^{1}O$_2$-mediated photobleaching case, note the sharp transition between the outermost spheroid region where significant amounts of ^{1}O$_2$ are deposited and the central spheroid core where ^{1}O$_2$ production occurs at a minimal level. This abrupt demarcation can be contrasted to the gradual ^{1}O$_2$ deposition changes observed for the photobleaching mechanisms involving the excited singlet and triplet sensitizer. Even though the ^{1}O$_2$ distributions for the two latter mechanisms are not significantly different, we notice that a smaller amount of ^{1}O$_2$ is deposited at the center of the spheroid for the case of sensitizer degradation involving the
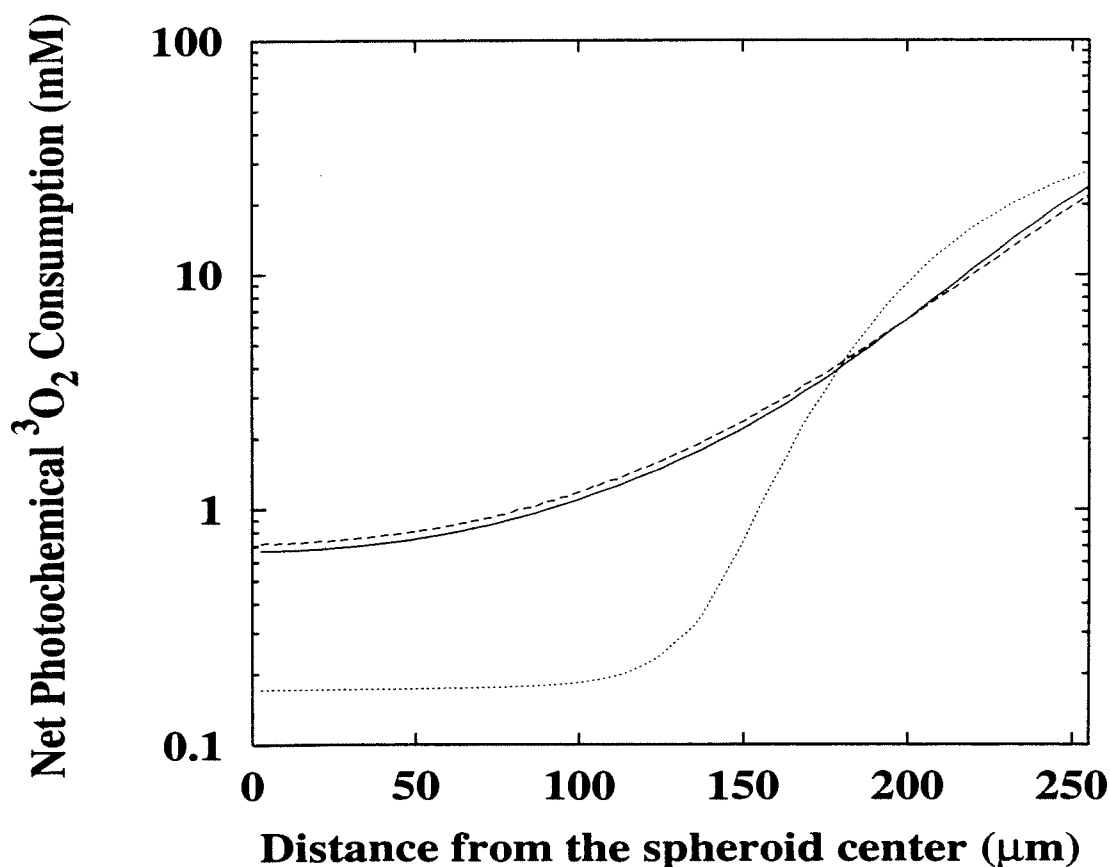
Figure 3.9: Simulated net photochemical ^{3}O$_2$ consumption distributions throughout an

EtNBSe-sensitized spheroid irradiated with 100 J cm^{-2} at a rate of 200 mW cm^{-2} when the

best fit value of the photobleaching constant is used for each of the four sensitizer

degradation descriptions. Simulations are shown for: fluence-dependent simple

exponential decay when α is 0.0355 J^{-1} cm^2 (------); photobleaching involving excited

singlet sensitizer reaction with cell substrate when k_{as} [A] is 0.0071 s^{-1} (------);

photobleaching from reactions of the excited triplets with cell substrate when k_{at} [A] is

0.0074 s^{-1} (——); and the ^{1}O$_2$-mediated mechanism when k_{os}/k_{oa} [A] is 118 M^{-1} (·····). The

curves for the first two descriptions overlap.

excited triplets. This is expected, since the $^3O_2$ concentration is lower at the center of the spheroid, and a larger population of triplets is, therefore, available to participate in photobleaching reactions in this region. Finally, the $^1O_2$ deposition curves corresponding to the best fit values of the singlet sensitizer photobleaching rate, k_{as} [A], and the photobleaching constant describing the fluence-dependent exponential decay, α, are identical.

3.4.4 Comparisons between the empirical fluence dependent and the theoretical time dependent simple exponential decay photobleaching descriptions

The observation that the dose distributions for the $e^{-\alpha D}$ and the $e^{-k_{as}[A]t}$ descriptions of photobleaching are identical could lead one to conclude that the phenomenological fluence-dependent simple exponential decay description of sensitizer loss is equivalent to a photobleaching mechanism involving the excited singlets and similar to the mechanism involving excited triplets. Even though this might appear to be true when one particular fluence rate is considered, we find that the predictions of the fluence-dependent expression are different from those consistent with any reasonable mechanism when evaluated over a range of fluence rates. Specifically, as shown in Figure 3.10a, the rate of the bleaching-induced $^3O_2$ concentration changes as a function of incident fluence is expected to be very similar for different fluence rate irradiations according to the fluence-

dependent photobleaching description (Simulated $^3O_2$ concentration distributions are shown for 200 and 50 mW cm^{-2} irradiations). In contrast, when we consider sensitizer degradation resulting from excited singlet reactions with cell substrate, we find that the $^3O_2$ concentration should increase at a higher rate as the fluence rate decreases for a given fluence. A similar fluence rate dependence for the $^3O_2$ concentration changes is predicted for photobleaching involving the excited sensitizer triplets (data not shown). Oxygen concentration measurements recorded during 200 and 50 mW cm^{-2} irradiations of EtNBSe-sensitized spheroids are shown as a function of fluence in Figure 3.10b to demonstrate that the data are consistent with our theory. The dependence of $^1O_2$-mediated photobleaching on fluence rate has been demonstrated previously (chapter 2, ref. (2)). Therefore, all the mechanisms of sensitizer degradation that we consider, $^1O_2$- and non-$^1O_2$-mediated, affect the rate of photochemical $^3O_2$ consumption for a given fluence in a manner that depends on the fluence rate of irradiation. This effect is not consistent with a fluence-dependent simple exponential decay description of photobleaching.

These differences in the rate of change of the $^3O_2$ concentration as a function of fluence rate correspond to equivalent differences in the rate of change of the sensitizer concentration that one would expect during observation of sensitizer fluorescence decay. This is depicted explicitly in Figure 3.11, which includes the changes in sensitizer concentration as a function of fluence occurring as a result of photobleaching during 200 and 50 mW cm^{-2} irradiations. Note that these changes are normalized to the initial excited sensitizer population. The e^{-aD} description of photobleaching predicts identical rates of
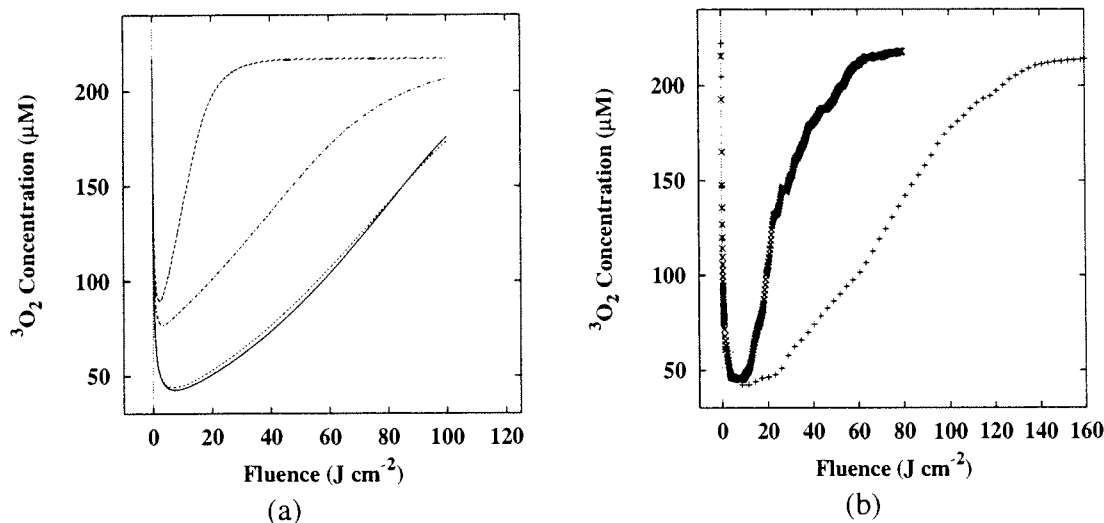
Figure 3.10: The fluence-dependent simple exponential decay is not consistent with predictions of the non-^{1}O$_2$-mediated sensitizer degradation mechanisms. (a) The calculated ^{3}O$_2$ distributions demonstrate that the rate of change of ^{3}O$_2$ concentration $vs.$ fluence as a result of photobleaching is very similar for 200 ($\cdots$) and 50 (- · - · -) mW cm^{-2} irradiations when the $e^{-\beta D}$ description is considered ($\alpha = 0.0395$ J^{-1} cm^2). In contrast, when plotted $vs.$ fluence, ^{3}O$_2$ concentration increases faster during the 50 mW cm^{-2} irradiation (- - -) than during the 200 mW cm^{-2} irradiation (————) when photobleaching involves excited singlet reactions with cell substrates (k_{as} $[A]$ = 0.0079 s^{-1}). (b) ^{3}O$_2$ concentration measurements recorded during 200 (+ + +) and 50 (x x x) mW cm^{-2} irradiations of EtNBSe-sensitized spheroids demonstrate that the data are consistent with the predictions of the non-^{1}O$_2$-mediated photobleaching theories.

sensitizer degradation for a given fluence, irrespective of the irradiation fluence rate (Figure 3.11a). In contrast, when photobleaching results from the reaction of excited singlets with cell substrate, a larger fraction of sensitizer is lost for a specific fluence during the lower fluence rate irradiation, even though the same value of $k_{as}[A]$ is used for both simulations (Figure 3.11b). Similar predictions are made when photobleaching involving the excited triplets is considered. In Figure 3.11c, predicted differences in the rate of fluorescence decay during 50 and 200 mW cm^{-2} irradiations are shown for the ^{1}O$_2$-mediated photobleaching case. Thus, these simulations show in a somewhat more direct way that the phenomenological fluence-dependent simple exponential decay description of photobleaching is not consistent with any reasonable mechanism of sensitizer degradation. For clarification, we show in Figure 3.11d that at any given instant the rate at which the overall (not the normalized) drug concentration is photobleached according to the non-^{1}O$_2$-mediated expressions (Equations 3.5 and 3.15) increases as a function of fluence rate, since the initial excited sensitizer population becomes larger with higher irradiation fluence rates.

3.4.5 Effects of non-^{1}O$_2$-mediated sensitizer photobleaching on dosimetry

Having determined the mechanism of EtNBSe photobleaching, we can study the effects of this non-^{1}O$_2$-mediated process on photodynamic dosimetry, which in turn can be compared to the trends that we observed previously for Photofrin®-PDT (2). To achieve
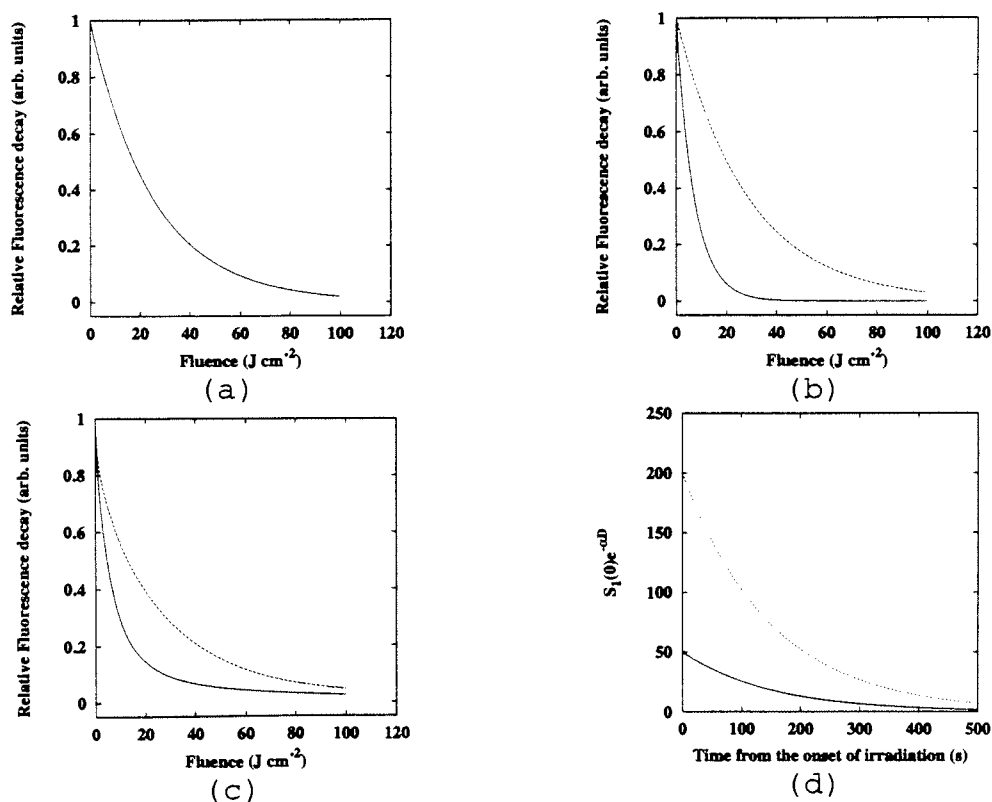
Figure 3. 11: The fluence-dependent simple exponential decay description of sensitizer

loss is consistent with neither the $^1O_2$-mediated nor the non-$^1O_2$-mediated photobleaching

mechanisms. Shown are calculations of the relative fluorescence decay of sensitizer as a

function of fluence for 50 (——) and 200 (- - - -) mW cm^{-2} irradiations for (a) the fluence-

dependent simple exponential decay description of photobleaching, (b) sensitizer degra-

dation as a result of reactions between excited singlets and cell substrate, and (c) $^1O_2$-

mediated photobleaching. Fluorescence decay of the overall sensitizer population is

shown in panel (d) for two irradiation fluence rates, one (- - - -) four times higher than

the other (——), as a function of time for photobleaching involving the excited singlets to

demonstrate that at any given time the rate of the absolute fluorescence decay increases

with increasing fluence rate.

that, we combine information from the analysis of the $^3O_2$ microelectrode measurements

with results from spheroid cell survival studies. From eight experiments performed with

EtNBSe-sensitized spheroids, we find that the ratio k_p/k_{ot} is 238 ± 76 µM. This ratio

expresses the $^3O_2$ concentration at which a triplet-state sensitizer molecule is equally likely

to either decay directly to its ground state or be quenched by a ground state oxygen

molecule. The k_p/k_{ot} of EtNBSe is much higher than that of Photofrin® (11.9 ± 2.2 µM).

The value for β_{PDT}, the proportionality constant between fluence rate and the time and

space invariant component of the maximum photodynamic rate of oxygen consumption,

is 9.6 ± 1 µM s^{-1} mW^{-1} cm^2. Using these values, we produce the net photochemical $^3O_2$

consumption curves shown in Figure 3.12 for a 100 J cm^{-2} irradiation delivered at 50, 100

and 200 mW cm^{-2}. As explained previously, these curves are equivalent to $^1O_2$ deposition

maps. We note that increasingly higher concentrations of $^1O_2$ are deposited at the center

of the spheroid as the fluence rate decreases. However, differences in the $^1O_2$ deposition

patterns are much more significant between 200 and 100 mW cm^{-2} than between 100 and

50 mW cm^{-2} irradiations. The non-uniform drug distribution leads to more pronounced

variations in the amount of $^1O_2$ deposited between the central and outer regions of the

spheroid than would be expected for the case of uniform sensitizer localization.

Nevertheless, these differences occur gradually; no sharp demarcation between regions

receiving high and low concentrations of $^1O_2$ exist. Also, note that the $^1O_2$ dose curves

corresponding to different fluence rates for this type of photobleaching cross each other,

a phenomenon that is not predicted for $^1O_2$-mediated photobleaching (chapter 2, ref. (2)).
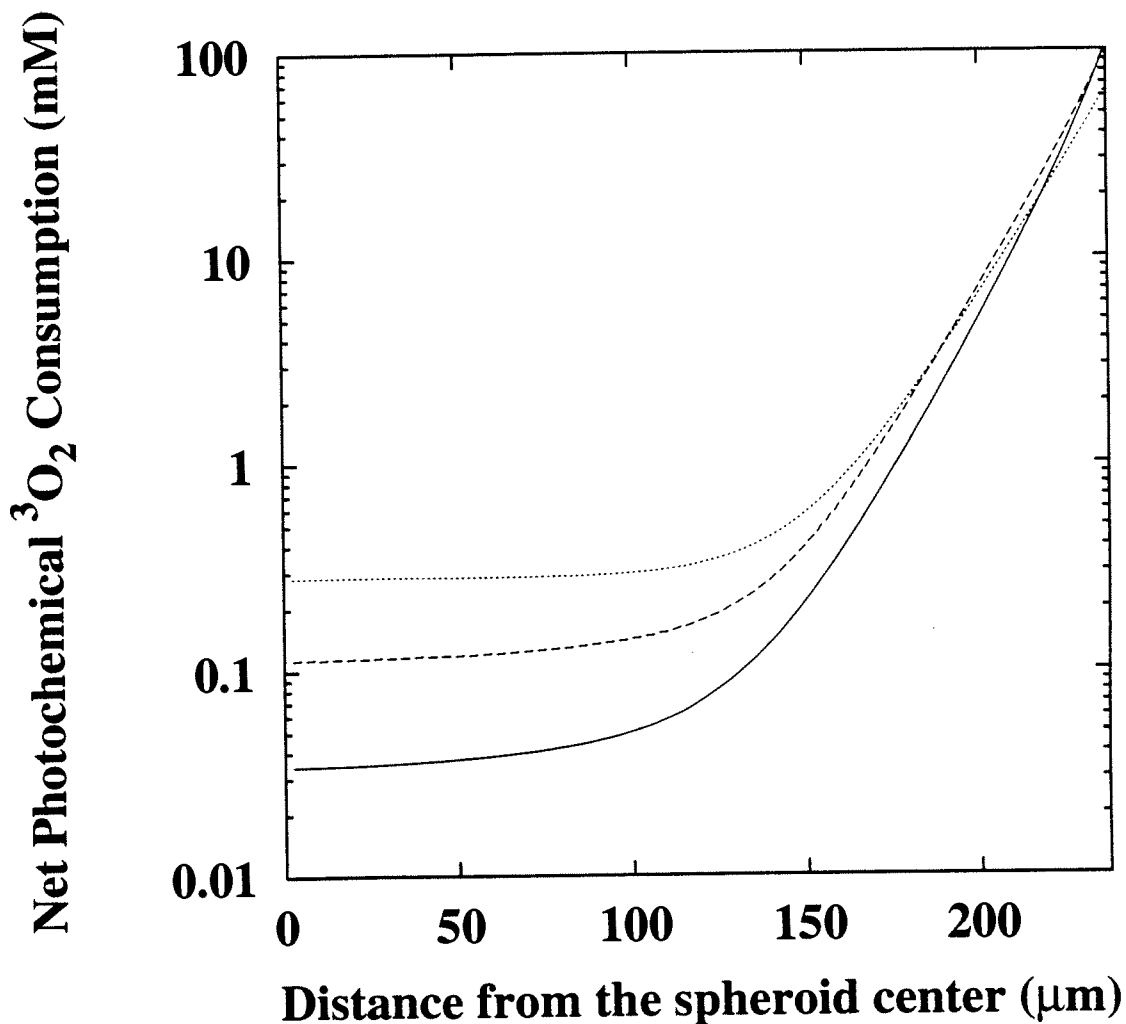
Figure 3.12: Calculated net photochemical ^{3}O$_2$ consumption curves for 100 J cm^{-2} irradiations delivered at 200 (———), 100 (— — — —), and 50 (·······) mW cm^{-2} to EtNBSe-sensitized spheroids. These distributions are equivalent to ^{1}O$_2$ deposition maps for the particular PDT protocols.

Our model's predictions concerning fluence rate effects on ^{1}O$_2$ deposition and, thus, on efficacy of the photodynamic treatment are tested by performing a series of survival assays with spheroids that are subjected to sensitizer incubation and irradiation conditions identical to those upon which our simulations were based. We have described some of the details of the spheroid cell survival assay used to determine the threshold dose of ^{1}O$_2$ in the previous chapter. Briefly, we selected groups of 50 spheroids (approximately 500 μm in diameter) and treated them with 1.5 μM EtNBSe for 30 min. Following incubation, the spheroids were washed four times with HBSS and irradiated with a fixed dose of 662 nm light (100 J cm^{-2}) delivered at 200, 100, or 50 mW cm^{-2}. A group of spheroids that received no light served as the control, while a second sample that received neither sensitizer nor light was used to determine the mean and standard deviation of the spheroids' diameter for the particular experiment. After light treatment, spheroids were dissociated to determine the fraction of cells that survived PDT immediately following irradiation. A specific number of the surviving cells from each group were plated in quintuplicate to calculate the percentage of these cells that had the ability to form colonies. The equal tails Student's t test (10) for examining statistical significance in the difference of means was used to determine the significance level at which the populations of the spheroid cell survival experiments were different.

The normalized cell yields obtained from spheroids dissociated immediately after irradiation are shown in Figure 3.13a. We find that the cell yields from the 200 mW cm^{-2}

irradiations are statistically higher than those from the 100 and 50 mW cm^{-2} groups (P <

0.05), while there is no statistical difference for the 100 and 50 mW cm^{-2} cases even for

P < 0.60. Following spheroid dissociation, we perform a colony-forming assay. As shown

in Figure 3.13b, cells that survive photodynamic treatment and enzymatic dissociation,

irrespective of the fluence rate at which light was delivered, are as capable of forming

colonies as our control population (P < 0.05). The efficiency (product of cell recovery and

plating efficiency) of the various photodynamic treatments is portrayed in Figure 3.13c.

The overall surviving fraction for the 200 mW cm^{-2} irradiations is statistically higher than

it is for the 100 mW cm^{-2} (P < 0.10) and the 50 mW cm^{-2} samples (P < 0.05). The overall

surviving fractions for the 100 and 50 mW cm^{-2} groups are statistically different only for

P < 0.20.

We can combine the results from the microelectrode and spheroid cell survival

experiments to determine the minimum amount of $^1O_2$ required to kill EtNBSe-sensitized

EMT6 cells. We assume that all spheroid cells that survive photodynamic treatment reside

within the central, most $^3O_2$ depleted region of the spheroid, where the lowest

concentrations of $^1O_2$ are deposited. The radius of the spherical volume that these cells

occupy is determined and defined as the critical radius, R_c: cells within the critical radius

survive therapy, while those beyond it are photodynamically destroyed. Finally, we refer

to the net photochemical $^3O_2$ consumption curves shown in Figure 3.12 to determine the

concentration of $^1O_2$ that is deposited at this critical radius for the different treatment

(a)

(b)

(c)
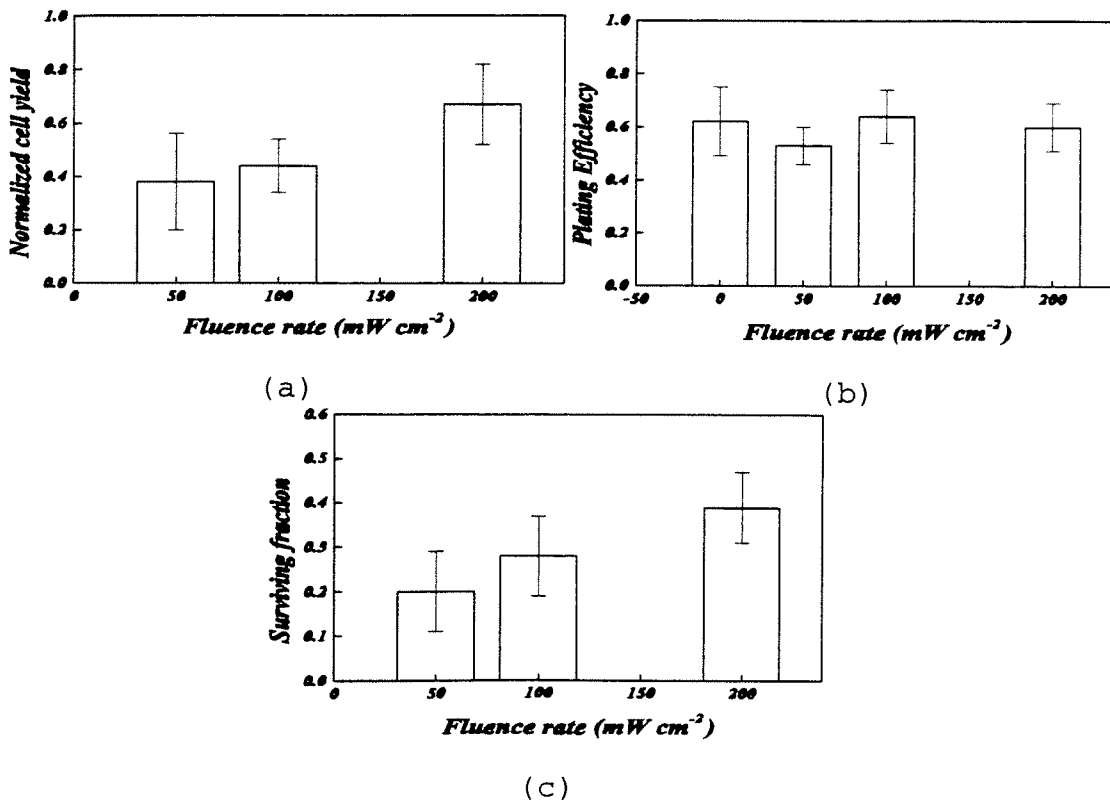
Figure 3.13: (a) The normalized cell yields acquired by chemical dissociation of EtNBSe-sensitized spheroids immediately following 100 J cm^{-2} irradiation delivered at 200, 100, and 50 mW cm^{-2} are 0.67 ± 0.15, 0.44 ± 0.10, and 0.38 ± 0.18, respectively (mean ± SD; n=6). (b) The plating efficiencies of the cells that survived PDT and chemical dissociation immediately after irradiation are 0.62 ± 0.13, 0.60 ± 0.09, 0.64 ± 0.10, and 0.53 ± 0.07 for the control, 200, 100, and 50 mW cm^{-2} groups, respectively (mean ± SD). (c) The products of the normalized cell yields and the plating efficiencies, shown as the overall surviving fraction for each group, are 0.39 ± 0.08, 0.28 ± 0.09, and 0.20 ± 0.09 for the spheroids receiving 200, 100, and 50 mW cm^{-2} irradiations, respectively (mean ± SD). The overall surviving fraction following the 200 mW cm^{-2} irradiation is statistically higher than those following the 100 mW cm^{-2} ($P < 0.10$) and 50 mW cm^{-2} irradiations ($P < 0.05$).

groups. Individual values for the threshold dose of ^{1}O$_2$ determined from six experiments at each of the three fluence rates are depicted in Figure 3.14. The minimum concentration of ^{1}O$_2$ required to kill EtNBSe-sensitized EMT6 spheroids is 0.58 ± 0.1 mM (mean ± SEM), a value significantly lower than that obtained for Photofrin®-treated EMT6 spheroids (12.1 ± 1.2 mM) (2).

3.5 Discussion

3.5.1 Non-^{1}O$_2$-mediated sensitizer photobleaching involving the excited singlets and excited triplets

Non-^{1}O$_2$-mediated photobleaching mechanisms and their effects on photodynamic dosimetry embody the central issues addressed in this chapter. Specifically, we have developed mathematical models for the irreversible degradation of sensitizer through reactions of the excited singlet (Eq. 3.5) and triplet states (Eq. 3.15) with cell substrate, and we study the implications of these mechanisms for ^{1}O$_2$ deposition during PDT of sensitized multicell tumor spheroids. Our experiments are performed primarily with EtNBSe, a photosensitizer that belongs in the benzophenoxazine family and that has a very different structure from that of porphyrins.

The expressions describing non-^{1}O$_2$-mediated sensitizer loss involving excited singlets and triplets are developed in section 3.2. Photobleaching resulting from reactions of the excited singlets with cell substrate is described by first order kinetics and a constant photobleaching rate, $k_{as}[A]$. For a small system like a spheroid, within which the delivered
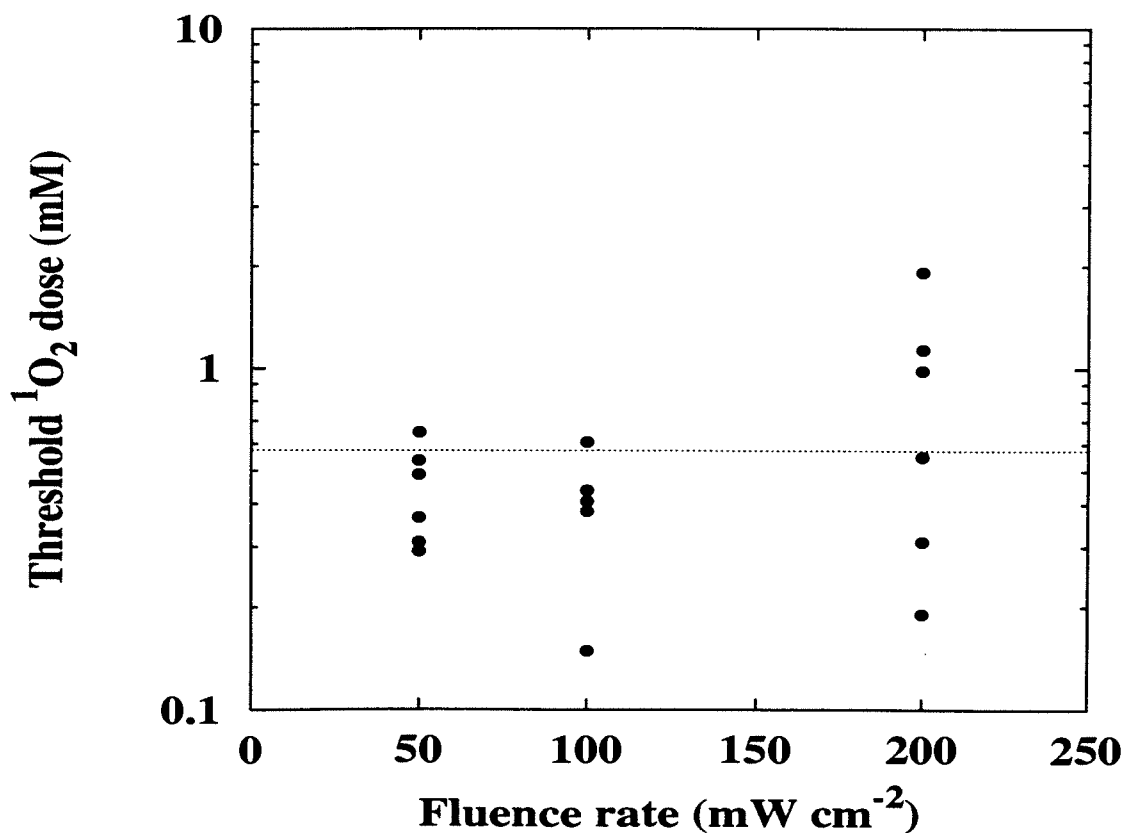
Figure 3.14: Estimates of the threshold ^{1}O$_2$ dose required to kill EtNBSe-sensitized

EMT6 spheroid cells for a 100 J cm^{-2} irradiation delivered at 200, 100, and 50 mW cm^{-2}.

The overall surviving fraction from each spheroid cell survival experiment is assumed to

lie within the central core of the spheroid which receives the least amount of ^{1}O$_2$. The

radius of the volume that these cells occupy is determined and, from photochemical ^{3}O$_2$

consumption maps similar to the ones shown in Fig. 3.12, the amount of ^{1}O$_2$ deposited

at this radius is estimated. The mean threshold dose (·····) thus determined from 18

experiments is 0.58 ± 0.1 mM (mean ± SEM).

light dose does not vary, such a mechanism is consistent with spatially uniform drug inactivation, if the drug is distributed uniformly. Sensitizer degradation involving triplet reactions is also described by a constant photobleaching rate, $k_{at}[A]$; however, in this case the analysis is modified to describe the dependence of the triplet population on the ^{3}O$_2$ concentration. As a result, for a given fluence, the normalized concentration of photoinactivated drug increases gradually from the central, hypoxic core to the ^{3}O$_2$ rich spheroid edge. Thus, if ^{3}O$_2$ gradients are present, photobleaching is not a spatially uniform process, even in the absence of variations in the delivered light dose. In the case of EtNBSe, non-uniformities are introduced also as a result of the manner in which the drug is taken up by the spheroid cells for the particular incubation protocol.

Differences between sensitizer photobleaching involving the excited singlets and triplets are not significant enough to allow us to distinguish between the two mechanisms simply by fitting the corresponding photobleaching expressions to ^{3}O$_2$ concentration changes obtained from microelectrode recordings during PDT of sensitized spheroids (Figure 3.6a). The hypothesis that it is the triplet, not the singlet, form of EtNBSe that reacts irreversibly with cell substrate is based on the observation that for a specific number of absorbed photons EtNBSe photobleaches faster than EtNBS, a sensitizer with similar structure and absorption coefficient, but significantly lower triplet yield (Figure 3.6b). Nevertheless, one cannot exclude the possibility that differences in the detailed localization patterns or the bimolecular rate constant for reaction between cell substrate and excited singlet for EtNBSe and for EtNBS result in the observed differences in the rates of sensitizer degradation.

3.5.2 The empirical fluence-dependent model versus the mechanistic descriptions of sensitizer degradation

One of the main findings of this work is that the phenomenological, fluence-dependent simple exponential decay description of photobleaching is inconsistent with any of the photochemical mechanisms of sensitizer degradation that we have considered. We have reported in the previous chapter on the inability of expressions that consist of a constant photobleaching rate to describe the continuously varying ^{1}O$_2$-mediated sensitizer degradation process (2). Even though, as shown in Figure 3.9, the e^{-aD} description appears to be equivalent to the photobleaching mechanism involving the excited singlets when only one fluence rate is under consideration, we demonstrate in Figures 3.10 and 3.11 that this is not the case when bleaching is evaluated at more than one fluence rate. In Figure 3.10a, we show that the rate of increase in ^{3}O$_2$ concentration as a function of fluence resulting from photobleaching during irradiation at two different fluence rates becomes greater with decreasing fluence rate according to the models that are based on either the excited singlet or the triplet interactions (shown is photobleaching resulting from excited singlet reactions). This can be contrasted to the similar rates of change in ^{3}O$_2$ concentration that are expected with increasing fluence, irrespective of irradiation fluence rate, for the phenomenological, fluence-dependent (e^{-aD}) photobleaching. The increasing rates of change in ^{3}O$_2$ concentration vs. fluence for decreasing fluence rate irradiations correspond to equivalent differences in the rates of change of sensitizer concentration normalized to the initial excited sensitizer population, as shown in Figure 3.11b. Namely,

for sensitizer degradation *via* either excited state reaction mechanism, the normalized rate of irreversible drug modification increases with decreasing fluence rate for a given fluence. This occurs because, in these models, photobleaching is exponential in the *time* rather than in the *fluence*. As the time required to deposit the same number of photons increases for decreasing fluence rates of irradiation, we observe a concomitant increase in the normalized amount of degraded sensitizer. However, note that at any given instant the absolute rate of sensitizer photobleaching (for example, $S_1(0)exp(-k_{as}[A]t)$ for photobleaching involving the excited singlets) increases with increasing fluence rate (Figure 3.11d). Figure 3.11c demonstrates the differences in the amounts of lost sensitizer that are expected when ^{1}O$_2$-mediated photobleaching is considered for a specific fluence delivered at two fluence rates. Since α in the $e^{-\alpha D}$ description expresses constant photobleaching in terms of deposited fluence, this model predicts that equivalent amounts of sensitizer are degraded for a specific fluence, independent of the rate at which this fluence is deposited (Figure 3.11a). Therefore, the fluence-dependent simple exponential decay description of photobleaching is inconsistent, not only with ^{1}O$_2$-mediated photobleaching, but also with non-^{1}O$_2$-mediated mechanisms based on excited singlet or triplet sensitizer reactions. Another significant implication of this finding is that apparent differences in the photobleaching constant as a function of fluence for varying fluence rates do not provide conclusive evidence in support of a ^{1}O$_2$-mediated photobleaching mechanism.

3.5.3 $^1O_2$- *vs.* non-$^1O_2$-mediated sensitizer photobleaching

mechanisms

The distinction between the two non-$^1O_2$-mediated mechanisms is certainly more subtle than the discrepancies that arise when either of these is compared to $^1O_2$-mediated sensitizer inactivation. For example, the differences between $^1O_2$- and non-$^1O_2$-mediated photobleaching are sufficiently great that they are clearly discerned through analysis of photodynamically induced $^3O_2$ concentration changes using the corresponding model expressions (Equations 3.5 or 3.15 and 3.16, respectively). The excellent agreement between microelectrode recordings obtained during irradiation of EtNBSe-sensitized spheroids and the predictions of the sensitizer photobleaching model involving triplet reactions (Figure 3.5a) can be contrasted to the inability of the $^1O_2$-mediated sensitizer degradation scheme to describe the same data (Figure 3.5b). The situation is reversed for the case of Photofrin®- (chapter 2, ref. (2)) and δ-ALA induced PpIX-treated spheroids (Figure 3.8).

Deviation from first order kinetics of the fluorescence decay of excited PpIX has been observed by others (11, 12). Moan *et al.* (12) used a bi-exponential model to analyze measurements of the loss of fluorescence intensity from PpIX during irradiation of WiDr cells. They suggested that the two observed photobleaching rates could correspond to degradation of PpIX in two different environments, for example, PpIX bound to proteins and unbound PpIX. However, they acknowledged that the decay rates obtained from their analysis depend on the initial PpIX concentration in a manner that is not consistent with

first order kinetics. A similar inconsistency appears in the decay rates corresponding to a pure second order kinetics model. The $^3O_2$ dependence of PpIX degradation has been shown by others in environments varying from oil-in-water microemulsions to tumors (13, 14, 15, 16). It was found that the rate of PpIX photobleaching was lower in UVB-irradiated mouse skin than in non-UVB-treated animals whose epidermis is better oxygenated (15). However, no correlation was found in this study between the initial fluorescence intensity of PpIX and its photobleaching rate. Robinson *et al.* (16) found that the rate of photobleaching as a function of total fluence increases with decreasing fluence rate. Oxygen depletion at high fluence rates of irradiation (50-150 mW cm^{-2}) was shown to affect significantly the rate of photobleaching, suggesting that $^1O_2$ is involved in the photobleaching reactions. A $^1O_2$-mediated photobleaching expression that depends on the initial sensitizer concentration has been developed by Forrer *et al.* (17) to describe mTHPC fluorescence decay measurements obtained during PDT of early squamous cell carcinomas in the esophagus. This expression could be valid under conditions of minimal changes in the local $^3O_2$ concentration during therapy and could explain the *in vitro* dependence of PpIX degradation on the initial PpIX content observed by Moan *et al.* (12). However, Forrer's model is not consistent with the *in vivo* results obtained by van der Veen *et al.* (15) and by Robinson *et al.* (16) for high fluence rates of irradiation. The different dependencies of the photobleaching rate for the *in vitro* and *in vivo* systems can be explained by a $^1O_2$-mediated photobleaching expression, such as the one presented in this chapter, that allows the sensitizer degradation rate to vary as a function of the rate

of photodynamic $^3O_2$ consumption. Differences in the photobleaching rate as a function of initial sensitizer concentration observed during irradiation of cells in an environment that is not $^3O_2$-limited is a consequence of the fact that photodynamic $^3O_2$ consumption increases with the available drug concentration. On the other hand, in an environment such as a tumor, both sensitizer concentration and $^3O_2$ availability will influence the rate of sensitizer loss.

Determination of the proper photobleaching mechanism is important because it influences the spatial deposition of $^1O_2$ in a multicell environment, as shown in Figure 3.9 for a 100 J cm^{-2} irradiation delivered at 200 mW cm^{-2} to a EtNBSe-sensitized spheroid. When $^1O_2$ is responsible for photobleaching, sensitizer degradation progresses gradually from the regions closest to the $^3O_2$ source (the outermost rim) towards the center of the spheroid. The irreversible drug inactivation leads to a concomitant decrease in $^3O_2$ consumption, allowing more $^3O_2$ to diffuse (and more $^1O_2$ to be deposited) to spheroid areas further away from the $^3O_2$ source. Thus, in the case of $^1O_2$-mediated photobleaching, sensitizer is degraded mainly in those regions that receive significant amounts of $^1O_2$. In an $^3O_2$-limited environment, bleaching in these regions allows appreciable $^1O_2$ deposition to progressively advance to areas further from the $^3O_2$ source, which would otherwise receive minimal photodynamic dose. Therefore, $^1O_2$-mediated photobleaching has the potential to enhance the photodynamic effect under certain conditions, as long as it does not occur at a rate that diminishes the sensitizer before the threshold dose of $^1O_2$ is deposited. This scenario is very different from the photobleaching progression

corresponding to the non-$^1O_2$-mediated cases. For the mechanisms involving the excited

singlets and triplets, drug is photobleached throughout the spheroid during irradiation.

The rate at which inactivation occurs is spatially uniform when the singlet sensitizer is

involved and slightly modified as a function of distance from the $^3O_2$ source for the triplet

mechanism. However, the spatial variation resulting from the latter mechanism is opposite

in character to that observed during $^1O_2$-mediated photobleaching, since more sensitizer

is photobleached at the center of the spheroid, where the least amount of $^1O_2$ is deposited.

Under these schemes, while sensitizer loss in the most $^3O_2$-rich regions allows $^3O_2$

diffusion to progress to regions that are initially hypoxic, it is possible that enough

photobleaching occurs in the initially hypoxic regions to limit $^1O_2$ production when $^3O_2$

finally diffuses there. This may occur with either excited state mechanism, but it is

especially probable when triplet sensitizer is the moiety participating in photobleaching.

For example, simulations of net photochemical $^3O_2$ consumption incorporating a $^1O_2$-

mediated sensitizer photobleaching mechanism within a Photofrin®-sensitized spheroid

irradiated at 630 nm with 200 J cm^{-2} at a rate of 25 mW cm^{-2} predict that enough $^1O_2$

would be deposited to achieve the threshold $^1O_2$ dose throughout the spheroid. On the

other hand, similar simulations for triplet sensitizer photobleaching, occurring at a rate

equal to the best fit value obtained for $k_{at}[A]$ when Equation 3.15 was used to analyze the

$^3O_2$ distribution recorded during irradiation of a Photofrin®-sensitized spheroid, predict

that only subthreshold values of $^1O_2$ are deposited at the center of a 500 μm spheroid.

Therefore, it would not be possible to destroy photodynamically all the cells under

irradiation conditions that could be implemented during a realistic *in vivo* treatment. Nevertheless, to the extent that excited sensitizer molecules react irreversibly with cell substrate, type I interactions may be expected to enhance the cytotoxic effect of $^1O_2$ (In type I photooxygenation reactions, the sensitizer interacts directly with the substrate leading to radical production). Indeed, type I interactions may play a more significant role during EtNBSe-PDT than during Photofrin®-PDT. Specifically, we find that the threshold dose of $^1O_2$ for EMT6 spheroids is significantly lower when sensitized with EtNBSe (0.58 mM) than when treated with Photofrin® (12.1 mM). It is possible that less $^1O_2$ is required to kill EMT6 cells in the case of EtNBSe because its excited triplets are more likely to participate in reactions that lead to the production of radicals or other radical ion cytotoxic agents. Another possibility is that the sites of subcellular localization and photodamage are different for the two sensitizers, with EtNBSe targeting more sensitive organelles.

Unfortunately, the non-uniform uptake of EtNBSe by EMT6 spheroid cells for the specific incubation protocol that we employed makes comparisons between the cytotoxic efficiency of Photofrin® and of EtNBSe difficult. However, it is obvious from the net photochemical $^3O_2$ consumption simulations corresponding to the different sensitizer photobleaching mechanisms that a non-$^1O_2$-mediated photobleaching mechanism could impair the efficacy of a sensitizer as a photodynamic drug. Moreover, the significantly higher k_p/k_{ot} value for EtNBSe than for Photofrin® might contribute to differences in their

cytotoxic efficiencies, since the energy transfer from triplet sensitizer to ^{3}O$_2$ becomes less

probable for a given ^{3}O$_2$ concentration as k_p/k_{ot} increases. These findings indicate that the

optimal sensitizer for photodynamic therapy is not necessarily the one that has the highest

absorption coefficient and triplet yields. Characteristics such as the probability of the

reaction between ^{3}O$_2$ and triplet sensitizer and the mechanism *via* which the drug is

photobleached should be given serious consideration.

3.5.4 Reversibility of observed photobleaching reactions with

EtNBSe-sensitized spheroids

A very interesting enzymatic photodegradation process has been reported to occur under

hypoxic conditions with EtNBSe-treated EMT6 cells and EtNBSe-containing cell free

systems (3). This enzymatic reaction was found to be reversible when ^{3}O$_2$ was

reintroduced into the experimental system. We have found that this type of reversible

sensitizer photobleaching does not play a significant role during irradiation of sensitized

multicell spheroids. If the photobleaching process that is reported by the increasing ^{3}O$_2$

concentrations in our measurements were reversible upon rediffusion of ^{3}O$_2$, we would

expect that when light delivery is interrupted long enough to allow the restoration of the

^{3}O$_2$ gradient to its pre-irradiation state, ^{3}O$_2$ consumption would resume upon the onset

of each light treatment at the same rate as at the beginning of the initial irradiation. We

find that dark intervals of ten, fifteen, or twenty minutes between two irradiations do not

restore ^{3}O$_2$ consumption rates, i.e. the available sensitizer concentration does not increase

between the end of the first light treatment and the onset of the second irradiation. Thus, the type of EtNBSe photobleaching that we report on is irreversible.

3.5.5 Concluding remarks

In conclusion, this chapter along with the previous chapter represent a model for the description of $^1O_2$- and non-$^1O_2$-mediated sensitizer photobleaching and their effects on photodynamic dosimetry during irradiation of multicell tumor spheroids. We demonstrate that the widely used fluence-dependent simple exponential decay description of sensitizer degradation is not an appropriate model of photobleaching during PDT. We elaborate on the limitations that non-$^1O_2$-mediated photobleaching may pose to the effective treatment of tumor regions that do not have immediate access to $^3O_2$. We show that determination of the proper mechanism *via* which drug can be inactivated during irradiation has important consequences for the prediction of the temporal and spatial deposition of $^1O_2$ and, thus, for the efficacy of a particular treatment protocol. We note that higher extinction coefficients and $^1O_2$ yields for a sensitizer do not necessarily result in improved therapeutic effects. The details of the interactions of sensitizer with light and $^3O_2$ under normal and hypoxic conditions should be considered during the design of effective PDT photosensitizers.

Our spheroid model has served as an excellent system for beginning the study of the details of sensitizer photobleaching during PDT. As the $^3O_2$ and nutrient gradients encountered between the center and the edge of our spheroids are similar to those existing

between capillary walls and intercapillary regions of a tumor, we have been able to observe some of the effects of drug degradation on fluorescence decay and ^{1}O$_2$ deposition that one expects to detect during photodynamic treatment of tumors. Our hope is that the information we have obtained with the spheroid system will be useful in developing an equivalent model of sensitizer photobleaching for the analysis of *in vivo* fluorescence measurements.

References

1.   Nichols, M.G. (1996) *Transport of oxygen and light in model tumor systems.* Doctoral dissertation, University of Rochester, Rochester, NY.

2.   Georgakoudi, I., M.G. Nichols and T.H. Foster (1997) The mechanism of Photofrin® photobleaching and its consequences for photodynamic dosimetry. *Photochem. Photobiol.* **65**, 135-144.

3.   Cincotta, L., J.W. Foley and A.H. Cincotta (1993) Phototoxicity, redox behavior and pharmacokinetics of benzophenoxazine analogues in EMT-6 murine sarcoma cells. *Cancer Res.* **53**, 2571-2580.

4.   Georgakoudi, I. and T.H. Foster. (1998) Effects of the subcellular redistribution of two nile blue derivatives on photodynamic oxygen consumption. *Photochem. Photobiol.* **68**, 115-122.

5.   Berg, K., J.C. Bommer and J. Moan (1989) Evaluation of sulfonated aluminum phthalocyanines for use in photochemotherapy. A study on the relative efficiencies

of photoinactivation. *Photochem. Photobiol.* **49**, 587-594.

6.   Berg, K., K. Madslien, J.C. Bommer, R. Ofterbo, J.W. Winkelman and J. Moan (1991) Light induced relocalization of sulfonated meso-tetraphenylporphines in NHIK 3025 cells and effects of dose fractionation. *Photochem. Photobiol.* **53**, 203-210.

7.   Wood, S.R, J.A. Holroyd and S.B. Brown (1997) The subcellular localization of Zn(II) Phthalocyanines and their redistribution on exposure to light. *Photochem. Photobiol.* **65**, 397-402.

8.   Moan, J. and K. Berg (1991) The photodegradation of porphyrins in cells can be used to estimate the lifetime of singlet oxygen. *Photochem. Photobiol.* **53**, 549-553.

9.   Moan, J. (1990) On the diffusion length of singlet oxygen in cells and tissues. *J. Photochem. Photobiol. B: Biol.* **6**, 343-348.

10. Crow, E.L., F.A. Davis and M.W. Maxfield (1960). *Statistics Manual.* Dover Publications, Inc., New York, NY.

11. Bezdetnaya, L., N. Zeghari, I. Belitchenko, M. Barberi-Heyob, J.-L. Merlin, A. Potapenko and F. Guillemin (1996) Spectroscopic and biological testing of photobleaching of porphyrins in solutions. *Photochem. Photobiol.* **64**, 382-386.

12. Moan, J., G. Streckyte, S. Bagdonas, Ø. Bech and K. Berg (1997) Photobleaching of protoporphyrin IX in cells incubated with 5-aminolevulinic acid. *Int. J. Cancer* **70**, 90-97.

13.   Krieg, M. and D.G. Whitten (1984) Self-sensitized photooxidation of protoporphyrin IX and related free-base porphyrins in natural and model membrane systems. Evidence for novel photooxidation pathways involving amino acids. *J. Am. Chem. Soc.* **106**, 2477-2479.

14.   Krieg, M. and D. G. Whitten (1984) Self-sensitized photo-oxidation of protoporphyrin IX and related porphyrins in erythrocyte ghosts and microemulsions: a novel photo-oxidation pathway involving singlet oxygen. *J. Photochem.* **25**, 235-252.

15.   van der Veen, N., H.S. de Bruijn and W.M. Star (1997) Photobleaching during and re-appearance after photodynamic therapy of topical ALA-induced fluorescence in UVB-treated mouse skin. *Int. J. Cancer* **72**, 110-118.

16.   Robinson, D.J., H.S. de Fruijn, N. van der Veen, M.R. Stringer, S.B. Brown and W. Star (1998) Fluorescence photobleaching of ALA-induced protoporphyin IX during photodynamic therapy of normal hairless mouse skin: The effect of light dose and irradiance and the resulting biological effect. *Photochem. Photobiol.* **67**, 140-149.

17.   Forrer, M., T. Glanzmann, D. Braichotte, G. Wagnières, H. van den Bergh, J.F. Savary and P. Monnier (1995) In vivo measurement of fluorescence bleaching of meso-tetra hydroxy phenyl chlorin (mTHPC) in the esophagus and the oral cavity. *Proc. SPIE* **2627**, 33-39.

Chapter 4

Effects of the Subcellular Redistribution of

Two Nile Blue Derivatives on

Photodynamic Oxygen Consumption

4.1   Introduction

The effects of the subcellular localization of sensitizers on their efficacy as photodynamic

agents have been studied by several investigators (1, 2 and references therein). It has been

of interest to identify the cellular components whose damage as a result of photodynamic

treatment leads to cell death. The effects of lysosomal damage on PDT induced

cytotoxicity has been the focus of several studies, since a number of PDT sensitizers

localize in lysosomes (3-8). These studies are typically performed with monolayer

cultures, so that events such as rupture of the lysosomal membrane and redistribution of

the lysosomal contents can be assayed easily and observed using conventional microscopy

techniques. Several nile blue derivatives have been shown to localize in lysosomes as a

result primarily of the lysosomal pH gradient. The relationship between photodynamically

induced damage to the lysosomal membrane and enzymes and cell viability has been

studied with the MGH-U1 human bladder carcinoma cell line for some of the nile blue

derivatives (9-12).

In this chapter, we report on experiments that demonstrate how localization and

redistribution of two Nile Blue derivatives, EtNBS and EtNBSe, may affect photody-

namic $^3O_2$ consumption. Specifically, during irradiation of Nile Blue-sensitized spheroids

we observe a second phase of $^3O_2$ consumption, the onset of which is probably associated

with sensitizer relocalization from the lysosomes into the cytosol. This enhancement in

$^3O_2$ consumption indicates that the form of the dye present in the lysosomes does not

achieve its maximum potential in terms of photodynamic activity.

4.2   Experimental results and analysis

4.2.1 Fluorescence microscopy studies with EtNBS-sensitized monolayer cultures

The cellular distribution of EtNBS before and during PDT of monolayer cell cultures is

observed directly with fluorescence microscopy. Our imaging system consists of a Nikon

diaphot inverted microscope equipped with a mercury lamp source for epifluorescence

illumination and a Nikon F3 high-eyepoint camera. Fluorescence is detected using a

Nikon 60X (1.4 NA) Plan Apochromat oil immersion objective and a set of filters

appropriate for fluorescence excitation and collection of either EtNBS (600-640 nm

excitation, 655 nm barrier, 650 nm dichroic) or carboxylate-modified microspheres (330-

380 nm excitation, 420 nm barrier, 400 nm dichroic).

EMT6 cells are grown in subconfluent mode on glass coverslips (1 in. diameter)

and incubated for the colocalization studies overnight with 10 mL Eagle's Basal Medium

(Gibco-BRL, Grand Island, NY) containing 0.1 μm blue fluorescent carboxylate-modified

microspheres (λ_{exc} = 350 nm, λ_{em} = 440 nm) at a concentration of 4.5 x 10^9 particles/mL

(Molecular Probes, Eugene, OR). These beads are taken up by cells *via* phagocytosis and,

thus, ultimately localize in the lysosomes/endosomes (13, Janet Morgan, personal

communication). The following day the medium is aspirated and the cells are incubated

for 30 minutes at 37°C in a 60 mm tissue culture dish with 4 mL HBSS containing 0.1 μM

EtNBS in a humidified 5% CO_2—95% air atmosphere. After washing the sensitized cells

three times with HBSS, the coverslip is mounted in a Leiden coverslip dish (Medical

Systems Corp., Greenvale, NY) to allow observation of the sensitizer's subcellular

localization patterns *via* conventional fluorescence microscopy. The Leiden dish allows

a round coverslip to be secured to the bottom of an open centered teflon dish by an

aluminum ring with a bayonet fitting, thereby permitting the use of an oil-immersion

objective to study cells in culture (14). The cells are perfused with 1 mL HBSS during

these observations. 662 nm light from an argon-ion laser pumped dye laser (Coherent, Santa Clara, CA) is delivered to the cells at 50 mW cm^{-2}. Fluorescence photomicrographs (4 s exposures) are taken before and during irradiation. A different field of view is photographed at each time point because of significant EtNBS photobleaching occurring during each 4 s exposure. Light delivery is interrupted briefly during the time required to obtain the photomicrographs. Fluorescence microscopy experiments with EtNBSe-sensitized monolayer cultures were not performed due to very low fluorescence yields for EtNBSe.

Fluorescence photomicrographs taken immediately after sensitization of EMT6 cells with EtNBS indicate that this compound localizes mainly in round intracellular structures; some diffuse cytosolic localization is also observed (Figure 4.1a). A comparison in the fluorescence of cells co-incubated with EtNBS (Figure 4.1a) and carboxylate-modified microspheres (Figure 4.1b) demonstrates similar patterns of localization. Therefore, we presume that EtNBS is present initially at high concentrations in lysosomes.

The fluorescence photomicrographs shown in Figure 4.2 were taken before and during 50 mW cm^{-2} irradiation of EMT6 cells treated with 0.1 μM EtNBS for 30 min. Figure 4.2a shows once more the punctate fluorescence emanating from the lysosomes as well as some diffuse cytosolic localization, observed before the onset of irradiation. After 150 s of irradiation, EtNBS remains localized, as shown in Figure 4.2b. However,
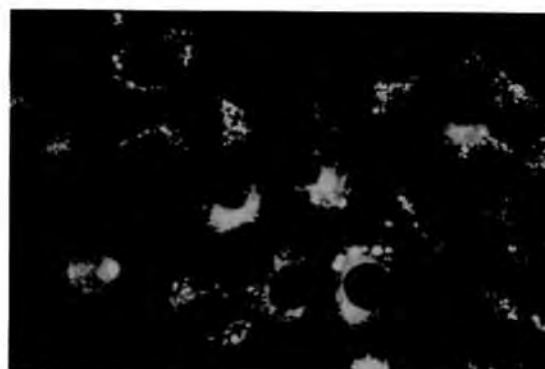
(a)
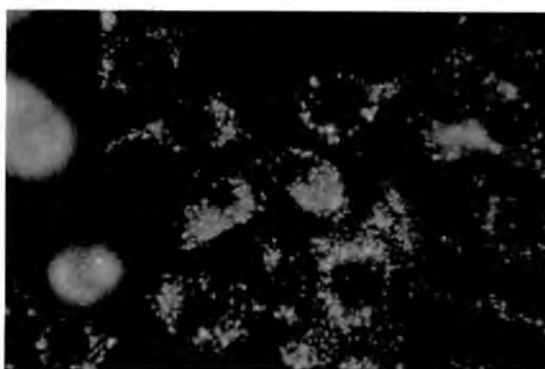
(b)

Figure 4.1: Fluorescence photomicrographs of EMT6 cells double stained with EtNBS

(a) and 0.1 μm blue fluorescent carboxylate-modulated microspheres (b) known to

localize in the lysosomes. The similar patterns of intracellular fluorescence indicate that

EtNBS localizes in the lysosomes.

(a)

(b)

(c)

(d)
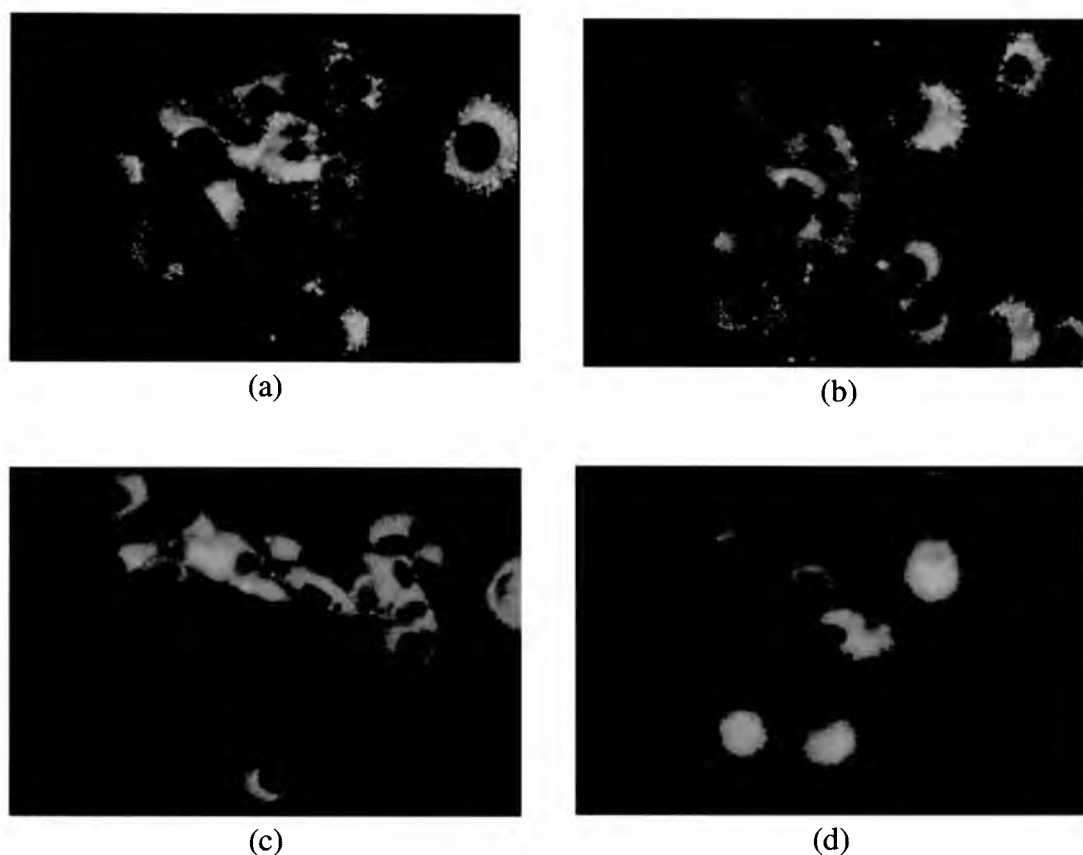
Figure 4.2: Fluorescence photomicrographs demonstrating EtNBS relocalization from cytoplasmic organelles to the cytosol during irradiation with 662 nm light delivered at 50 mW cm^{-2}. A different field of view is photographed at each time point because of appreciable EtNBS photobleaching during every 4 s exposure. The punctate fluorescence pattern in the perinuclear region, characteristic of lysosomes, can be detected before (a) and after 150 s of irradiation (b). Diffuse, rather faint cytoplasmic fluorescence is detected as well. This localization pattern can be contrasted to the strong, mainly diffuse cytoplasmic fluorescence detected at 200 s from the onset of irradiation (c). Faint fluorescence may be observed in the nucleus of some cells after 300 s of light delivery (d).

by 200 s (Figure 4.2c) EtNBS is redistributed into the cytosol with the nucleus remaining

as the only non-fluorescing region. Finally, at 300 s faint fluorescence may be detected

in the nuclear region of some cells (Figure 4.2d).

4.2.2 $^3O_2$ concentration changes observed during irradiation of

EtNBS-sensitized spheroids

To determine the effects of EtNBS localization on photodynamic $^3O_2$ consumption we

recorded the changes in $^3O_2$ concentration that occurred at the edge of EtNBS-sensitized

spheroids during irradiation. The experimental apparatus and the protocol followed for

recording these changes is identical to the protocol described in section 3.4.1. Spheroids

were incubated with 1.5 μM EtNBS for 30 min. Typical time-dependent $^3O_2$ electrode

traces are shown in Figure 4.3 for EtNBS-sensitized spheroids irradiated at 200, 100, and

50 mW cm^{-2}. The initial decrease in $^3O_2$ concentration resulting from photodynamic $^3O_2$

consumption is followed by a plateau as an equilibrium is reached between $^3O_2$ diffusion

and consumption. This equilibrium phase is succeeded consistently by a distinct second,

slower phase of photodynamic $^3O_2$ consumption. The onset of the second step is a fluence

dependent event as it occurs at approximately 200, 100, and 50 s after the beginning of

50, 100, and 200 mW cm^{-2} irradiation, respectively, corresponding to a fluence of 10 J

cm^{-2}. Therefore, for a 50 mW cm^{-2} irradiation the second $^3O_2$ consumption step begins at

the same time that we observe EtNBS relocalization from lysosomes to the cytosol.
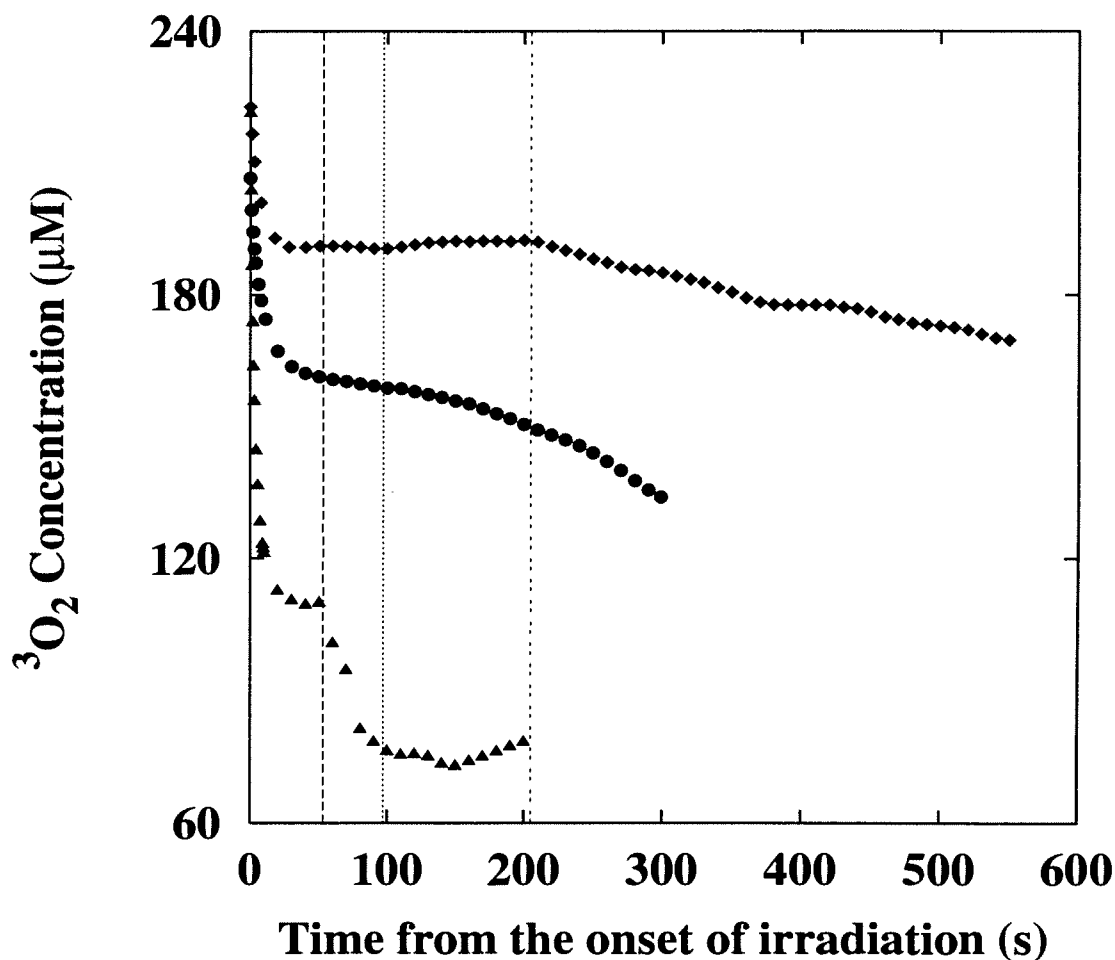
Figure 4.3: Time-dependent $^3O_2$ concentration measurements obtained at the edge of

EtNBS-sensitized spheroids during irradiation with 662 nm light delivered at 200 mW

cm^{-2} (▲), 100 mW cm^{-2} (●), and 50 mW cm^{-2} (◆). Analysis of these measurements using

a model of oxygen diffusion with consumption that accounts for a two-step $^3O_2$

consumption process demonstrates that the second $^3O_2$ consumption phase is triggered

by a fluence dependent event, since it begins at approximately 53 (- - -), 97 (······) and 205

(-- --) s from the onset of 200, 100 , and 50 mW cm^{-2} irradiation, respectively (pages 141-

142 and Table 4.1).

4.2.3 Sensitizer uptake studies with spheroids and monolayer

cultures

Different sensitizer incubation protocols were followed for the experiments performed

with cells in monolayer culture and with spheroids. We performed dye extraction

experiments to test whether similar amounts of sensitizer are taken up by the cells for the

two cases, and, thus whether the same number of photons is required to trigger EtNBS

relocalization in monolayer cultures and the onset of the second $^3O_2$ consumption phase

observed during irradiation of sensitized spheroids. For these studies, a group of 130-160

spheroids (approximately 500 µm in diameter) is selected and treated for 30 min in a 100

mm suspension tissue culture dish with 25 mL of HBSS containing 1.5 µM sensitizer at

37°C in a humidified 5% CO_2—95% air atmosphere. Along with this group, a sample of

13-16 spheroids is chosen for the determination of the mean diameter of the spheroids

used for the particular experiment. Spheroid disaggregation experiments performed

previously (15) allow us to associate the mean spheroid diameter with the number of cells

within such a spheroid. Therefore, given the number of spheroids in the sensitized group

and the average diameter, we can determine the total number of cells treated with

sensitizer. Following incubation, spheroids are washed three times with HBSS and

transferred to a 15 mL tube. The spheroids are centrifuged for 5 min at 1,000 rev/min,

and the resultant pellet is diluted in 1 mL of methanol:chloroform (1:1) containing 5 µL

of acetic acid/mL to extract the EtNBS or the EtNBSe contained in the cells (16). To

avoid reaction of the extraction solution with the container, we transfer the spheroids to a glass vial, where they remain for approximately 24 h to ensure that all of the sensitizer is extracted from the spheroid cells. Finally, the sensitizer content of the specific number of spheroid cells is determined *via* absorption spectrophotometry. These studies indicate that there are on average 0.39 ± 0.04 nmol EtNBS per million spheroid cells treated with 1.5 μM EtNBS for 30 min (n=3). This cellular concentration would be representative of cells throughout the spheroid if the sensitizer were taken up by the spheroid cells uniformly. In the previous chapter, we presented fluorescence images of thin EtNBS-sensitized frozen spheroid sections which demonstrated that the drug concentration falls off exponentially with distance from the spheroid edge. Therefore, most of the drug is taken up by the outer spheroid cell layers. However, considering that these outer cell layers occupy most of the spheroid volume (for example, the outer eight cell layers comprise 70% of the volume of a 500 μm diameter spheroid), the average EtNBS cellular concentration that we obtain from these studies is a good indicator of the amount of drug present in the spheroid region that affects the observed $^3O_2$ concentration changes the most.

To study EtNBS uptake by monolayer cultures, subconfluent EMT6 cells (approximately 19,000 cells/cm^2) are treated with 25 mL HBSS containing 0.1 μM EtNBS at 37°C in a humidified 5% CO_2—95% air atmosphere for 30 min. The cells are washed three times with HBSS, incubated for 2 min with 3 mL 0.25% trypsin, and transferred to a 15 mL centrifuge tube. Following centrifugation for 5 min at 1,000

rev/min, we extract EtNBS from the resultant pellet by exposing it to 2 mL methanol:chloroform (1:1) containing 5 μL acetic acid/mL for approximately 24 h in a glass vial to maintain consistency with the spheroid cell extraction studies. The amount of sensitizer in the cell/extract-solution mixture is quantified spectrophotometrically as above. From these experiments, we find that 0.5 ± 0.08 nmol EtNBS are contained per million cells for the specific incubation protocol (n=8). This is similar (P < 0.05, determined by equal tails Student's t-test (17)) to the average amount of EtNBS taken up by EtNBS-sensitized spheroids, supporting the hypothesis that the onset of the second $^3O_2$ consumption phase in spheroids is the result of EtNBS relocalization.

4.2.4 $^3O_2$ concentration measurements performed with EtNBSe-sensitized spheroids

Oxygen concentration measurements are performed also with spheroids sensitized with 1.5 μM EtNBSe for 30 min. A similar two-step pattern of $^3O_2$ consumption is observed. However, the second $^3O_2$ consumption phase is triggered by approximately eight times fewer absorbed photons than with EtNBS, occurring at 27, 50, and 81 s after the onset of 50, 25, and 15 mW cm^{-2} irradiation, respectively, or at a fluence of approximately 1.25 J cm^{-2} (Figure 4.4). Sensitizer extraction studies, performed as described in section 4.2.3, with EtNBSe-sensitized spheroids reveal that 0.38 ± 0.04 nmoles EtNBSe are taken up for every million spheroid cells, an amount similar to that obtained for EtNBS-sensitized

spheroids (n=3). Thus, differences in the fluence dependence of the second $^3O_2$

consumption phase for EtNBSe and EtNBS cannot be explained by differential uptake of

the sensitizers by EMT6 spheroid cells. Small differences in the extinction coefficients of

the two sensitizers at 662 nm ($\varepsilon_{NBSe} = 79,824$; $\varepsilon_{NBS} = 65,130$) cannot explain the eight-fold

difference in the timing of the second $^3O_2$ consumption phase.

4.2.5 Analysis of oxygen microelectrode measurements

For analysis of the $^3O_2$ concentration measurements recorded at the edge of EtNBS- and

EtNBSe-sensitized spheroids, our model of oxygen diffusion with consumption is

modified slightly to incorporate: a) non-uniform sensitizer distribution, and b) $^3O_2$

consumption occurring in two well defined phases. As described in detail in the previous

chapter, fluorescence intensity images of thin EtNBS-sensitized spheroid sections indicate

that the drug is not distributed uniformly throughout the spheroid for the incubation

protocol that we use. The non-uniformities in drug uptake can be described using a

monoexponentional decay function, which is used to modify the expression for the

maximum rate of photodynamic $^3O_2$ consumption, Γ_0, and, thus, to account for this non-

uniformity in our analysis. Specifically, Γ_0 is now written

$$\Gamma_0^{mod}(r) = \Gamma_0' \exp\left(-(r-R_s)/\theta\right), \tag{4.1}$$

where Γ_0' is the maximum rate of photodynamic oxygen consumption achieved in the case

of uniform drug distribution,
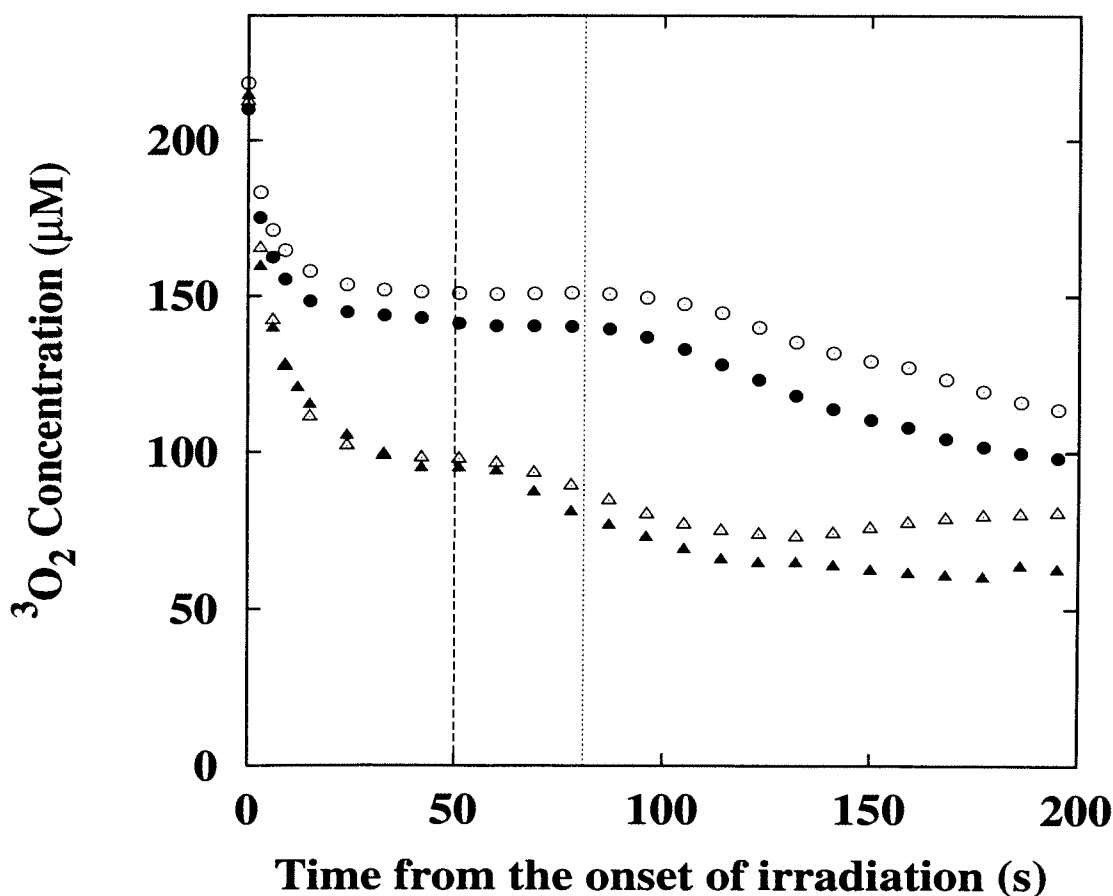
Figure 4.4: Time-dependent $^3O_2$ concentration measurements obtained at the edge of

EtNBSe-sensitized spheroids during irradiation with 662 nm light delivered at 25 mW

cm^{-2} (▲ and △) and 15 mW cm^{-2} (● and ○). Open and closed symbols represent two

separate experiments. As in the case of EtNBS, the onset of the second $^3O_2$ consumption

step is a fluence dependent event that is triggered by approximately eight times fewer

absorbed photons for EtNBSe than for EtNBS: it occurs at approximately 50 (- - -) and

81(·····) s after the onset of 25 and 15 mW cm^{-2} irradiation, respectively (Table 4.2).

$$\Gamma_0' = S_\Delta\, \varphi_t I_a \left(\frac{k_{oa}[A]}{k_d + k_{oa}[A]} \right), \tag{4.2}$$

and r is radial distance from the center of the spheroid. The value of the constant θ is determined from analysis of EtNBS-sensitized frozen spheroid sections and is assumed to be the same for EtNBS- and EtNBSe-sensitized spheroids.

The maximum rate of photodynamic $^3O_2$ consumption is modified further by a sigmoid function to account for the second $^3O_2$ consumption phase observed during irradiation of Nile Blue-sensitized spheroids. Therefore, the final form of Γ_0 is written as:

$$\Gamma_0(r) = \Gamma_0^{mod}(r) \left(1 + C \frac{(t - t_i)^n}{(t_{50} - t_i)^n + (t - t_i)^n} \right) \tag{4.3}$$

where $\Gamma_0^{mod}(r)$ is the maximum rate of photodynamic $^3O_2$ consumption achieved during the first $^3O_2$ consumption phase at a given radial distance r from the center of the spheroid given by Eq. 4.1, C is a scaling factor describing the relative magnitude of the second $^3O_2$ consumption step, t is time from the onset of irradiation, t_i is the time at which the second $^3O_2$ consumption phase begins, t_{50} is the time at which Γ_0 achieves a value that is half way between $\Gamma_0^{mod}(r)$ and its maximum, and n is a parameter that describes, along with t_{50}, how fast Γ_0 changes.

During analysis, t_{50} and n are used as fitting parameters. Each time-dependent $^3O_2$ distribution is fit several times with C and t_i fixed at specific values. The first value at which t_i is fixed is determined by observing the time at which the second $^3O_2$ consumption phase appears to start in the recorded $^3O_2$ concentration. Different fits with t_i varying in

2.5 s increments from this initial value are attempted, until the optimal value is determined. C is used as a fitting parameter only during the first fit of each recorded $^3O_2$ distribution. The mean value of C thus obtained is used as the initial value to which C is fixed during subsequent fitting sessions. Different values of C, varying in increments of five, are tested, until the best fit to the data is achieved. It is necessary to fix C and t_i in this fashion so that meaningful estimates of t_{50} and n can be obtained.

A fit to an $^3O_2$ distribution obtained during a 25 mW cm^{-2} irradiation of an EtNBSe-sensitized spheroid is shown in Figure 4.5 to demonstrate the ability of our model to describe the two-step $^3O_2$ consumption process. The best values obtained for C, t_i, t_{50}, and n are shown in Tables 4.1 and 4.2 for experiments performed at 200, 100, and 50 mW cm^{-2} for EtNBS-sensitized spheroids (Table 4.1) and at 50, 25, and 15 mW cm^{-2} for EtNBSe-sensitized spheroids (Table 4.2). Note that the onset of the second $^3O_2$ consumption phase as described by t_i is indeed a fluence dependent event. Moreover, the values obtained for t_{50} and C indicate that as the irradiation fluence rate decreases sensitizer relocalization leads to slower changes and an increasingly larger effect on the magnitude of the maximum rate of photodynamic $^3O_2$ consumption, Γ_0.
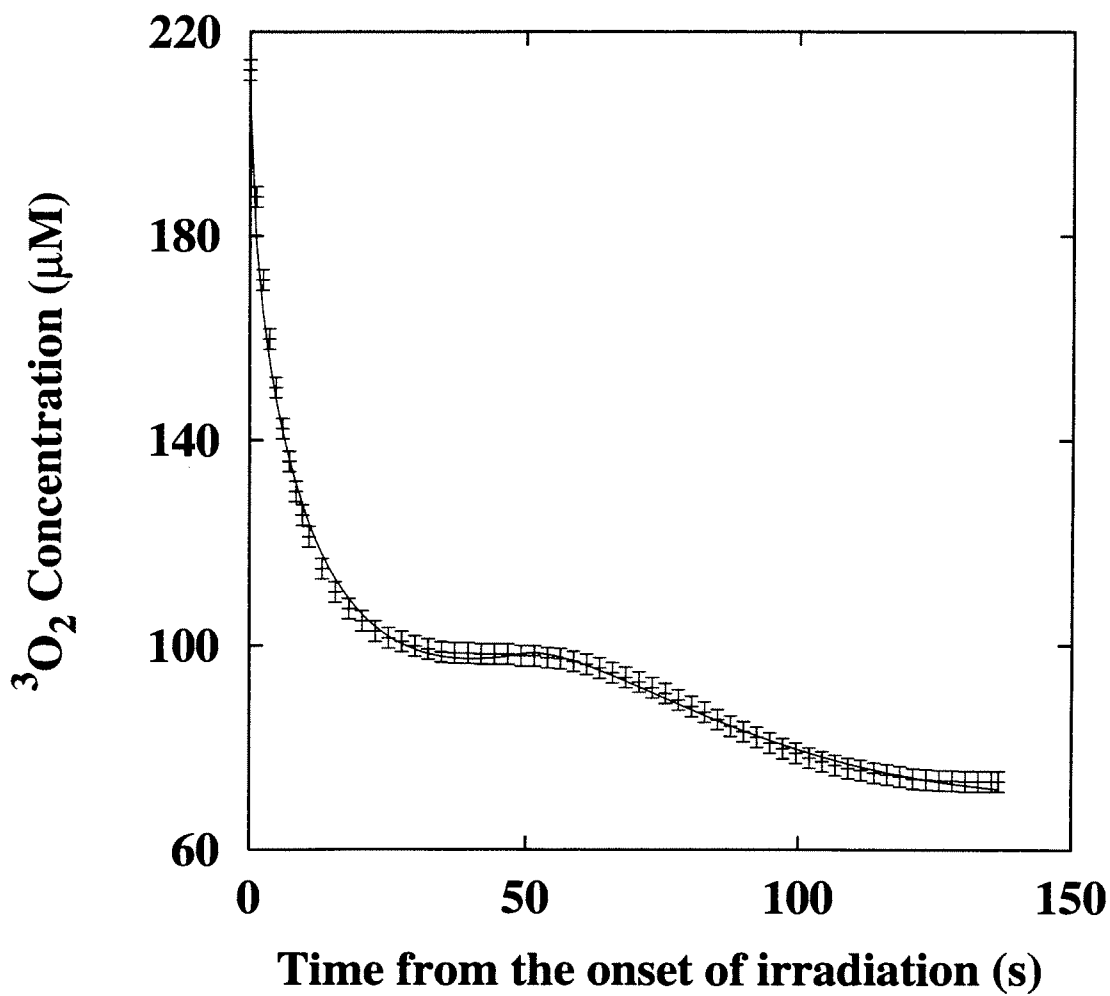
Figure 4.5: Typical fit obtained using our theoretical model of $^3O_2$ diffusion with

consumption, shown as the solid line, to $^3O_2$ concentration measurements recorded at the

edge of an EtNBSe-sensitized spheroid during irradiation with 662 nm light delivered at

25 mW cm^{-2}. From similar fits to $^3O_2$ measurements recorded during 15, 25 and 50 mW

cm^{-2} irradiations, we can obtain information about the characteristics of the observed

second $^3O_2$ consumption phase.

Table 4.1: Best fit values for the parameters describing the second $^3O_2$ consumption phase observed during irradiation of EtNBS-sensitized spheroids

Fluence rate	t_i	t_{50}	C	n
50 mW cm^{-2}	205 ± 7 s	38,325 ± 8,125 s	170 ± 56	1.0 ± 0.1
100 mW cm^{-2}	98 ± 4 s	4,894 ± 363 s	69 ± 9	1.3 ± 0.2
200 mW cm^{-2}	54 ± 5 s	633 ± 111 s	24 ± 6	1.2 ± 0.2

Shown is the mean ± SD of the value that resulted in the best fit for two experiments for every fluence rate group. C is a scaling factor describing the relative magnitude of the second $^3O_2$ consumption step; t_i is the time at which the second $^3O_2$ consumption phase begins; t_{50} is the time at which the maximum rate of photodynamic $^3O_2$ consumption, Γ_0, is half way between its initial and final values; n is a parameter that describes, along with t_{50}, how fast Γ_0 changes.

Table 4.2: Best fit values for the parameters describing the second $^3O_2$ consumption

phase observed during irradiation of EtNBSe-sensitized spheroids

Fluence rate	t_i	t_{50}	C	n
15 mW cm^{-2}	81 ± 3 s	1,864 ± 88 s	50	1.1 ± 0.04
25 mW cm^{-2}	53 ± 4 s	1,241 ± 121 s	32.5 ± 3.5	1.1 ± 0.04
50 mW cm^{-2}	27.5 s	744 ± 69 s	8	0.9 ± 0.1

Shown is the mean ± SD of the value that resulted in the best fit for two

experiments for every fluence rate group. If the same parameter value resulted in the best

fit for both experiments, only this value is reported. C is a scaling factor describing the

relative magnitude of the second $^3O_2$ consumption step; t_i is the time at which the second

$^3O_2$ consumption phase begins; t_{50} is the time at which the maximum rate of

photodynamic $^3O_2$ consumption, Γ_0, is half way between its initial and final values; n is

a parameter that describes, along with t_{50}, how fast Γ_0 changes.

4.3 Discussion

4.3.1 EtNBS localization and redistribution in monolayer cultures

The punctate fluorescence pattern observed before irradiation of EtNBS monolayer cultures, shown in Figures 4.1a and 4.2a, is similar to patterns of punctate localization observed by Cincotta et al. (16) with EtNBA-sensitized EMT6 cells. The results of our colocalization experiments with carboxylate-modified microspheres, indicating that the intracellular sites of EtNBS localization are lysosomes, are in agreement with detailed localization studies performed by Lin et al. (9-12) for several Nile Blue derivatives with the MGH-U1 human bladder carcinoma cell line. Specifically, histochemical staining with acid phosphatase, a standard lysosomal marker enzyme, demonstrates that the punctate fluorescence observed as a result of Nile Blue sensitization originates primarily from lysosomes (10, 11). Several other PDT sensitizers that exhibit similar punctate fluorescence have been found to localize in lysosomes (5-8, 18).

As shown in Figure 4.2, EtNBS is redistributed from the lysosomes into the cytosol after the delivery of approximately 10 J cm^{-2} of 662 nm light (200 s of 50 mW cm^{-2} irradiation). By the time 15 J cm^{-2} are deposited some fluorescence is detected in the nucleus of some cells; however, the possibility that out-of-focus fluorescence may appear as fluorescence emanating from the nucleus cannot be eliminated. Similar redistribution events have been observed previously with other lysosomal sensitizers, such as tetra(4-sulfonatophenyl)porphine, TPPS$_4$, (5, 6, 19, 20), the sulfonated aluminum

phthalocyanines Al-PcS$_2$, Al-PcS$_3$ and Al-PcS$_4$ (8, 18), and the tetrasulfonated and

pyridinium Zn (II) phthalocyanines (20).

4.3.2 Effects of EtNBS and EtNBSe redistribution on photodynamic

$^3O_2$ consumption

While sensitizer localization and redistribution during PDT have been studied mainly in

the context of their effects on the viability of specific enzymes and cells, our work reports

on the direct effects of sensitizer localization on photodynamic $^3O_2$ consumption in the

multicell tumor spheroid model. In Figure 4.3 we observe that $^3O_2$ consumption during

PDT of EtNBS-sensitized spheroids occurs in two well-defined phases. The onset of the

second $^3O_2$ consumption phase occurs when 10 J cm^{-2} are delivered to the spheroids,

irrespective of fluence rate. Thus, for a 50 mW cm^{-2} irradiation, the second $^3O_2$

consumption phase begins after approximately 200 s, $i.e.$ at the same time that sensitizer

relocalization is observed during PDT of monolayer cultures. Sensitizer uptake studies

indicate that the average amount of sensitizer retained per spheroid cell (0.39 x 10^{-6} ±

0.04x10^{-6} nmoles) is similar to the EtNBS cellular concentration of the monolayer

cultures we used for the microscopic observations of the drug's localization patterns

(0.5x10^{-6} ± 0.08x10^{-6} nmoles per cell). However, from fluorescence images of thin frozen

sections obtained from EtNBS-sensitized spheroids we know that the uptake of EtNBS

is not uniform throughout the spheroid. Rather, an exponentially decaying sensitizer

concentration gradient exists from the outer to the central spheroid regions. This non-uniformity in drug uptake makes comparison between spheroids and single cells difficult. Nevertheless, two considerations suggest that the sensitizer uptake information can be used at least in a qualitative manner. First, we note that the largest fraction of the spheroid volume is contained within its outermost cell layers. As mentioned in section 4.2.3, approximately 70% of the volume of a 500 μm diameter spheroid is occupied by its eight outer cell layers. Thus, the spheroid region that contains most of the sensitizer represents a large fraction of the total spheroid volume. Secondly, the $^3O_2$ concentration changes that we record at the edge of the spheroid are influenced by the entire spheroid volume, not just the cell layer in contact with the oxygen microelectrode. Therefore, the sensitizer uptake data is at least in qualitative agreement with the argument that the onset of the second phase of photodynamic $^3O_2$ consumption is probably associated with EtNBS redistribution from the lysosomal to the cytosolic milieu.

Oxygen electrode experiments performed with EtNBSe-sensitized spheroids demonstrate that $^3O_2$ consumption occurs in two phases also. However, for similar sensitizer incubation and irradiation protocols, the onset of the second $^3O_2$ consumption phase is triggered by approximately eight times fewer absorbed photons than in the case of EtNBS. This eight fold difference is not a result of differential sensitizer uptake or light absorption; however, it is qualitatively consistent with previously reported significantly higher $^1O_2$ yields for EtNBSe as compared to EtNBS (0.650 and 0.025, respectively) (16). Although the triplet yields for the two sensitizers have not been reported, it is

reasonable to assume that the $^1O_2$ yield differences for EtNBS and EtNBSe are due to

equivalent differences in triplet sensitizer yield. Therefore, it is hypothesized that $^1O_2$

and/or triplet sensitizer induced lysosomal damage could lead to sensitizer relocalization.

4.3.3 Implications of two-step $^3O_2$ consumption for sensitizer's efficiency as a photodynamic agent

The existence of two well-defined $^3O_2$ consumption phases shows that at least part of the

sensitizer initially localized in lysosomes is not photodynamically active, *i.e.* it is not

involved in photodynamic $^3O_2$ consumption, possibly because it exists in a highly

aggregated form. Indeed, the overall fluorescence intensity appears to increase upon

EtNBS redistribution into the cytosol, consistent with the hypothesis that the sensitizer

exists in a less aggregated state in the cytosol than in the lysosomes. Studies performed

with several PDT sensitizers, such as meso-tetra-hydroxyphenyl-chlorin (mTHPC) (21),

hematoporphyrin dibutyl ester (22), and several AlPcS$_n$s (23) indicate that the aggregated

forms of these dyes, as well, do not contribute significantly to photodynamic effects.

Specifically, comparisons among the absorption, fluorescence-excitation and action

spectra for mTHPC-treated cells suggest that it is primarily the monomeric, highly-

fluorescing form of the dye that contributes to the action spectrum of photodynamic

inactivation (21). Similarly, low fluorescence yields and aggregation can be correlated

with inefficient photosensitization for cells incubated with hematoporphyrin dibutyl ester

(22), and the most aggregated of four $AlPcS_ns$, $AlPcS_1$, possesses the lowest efficiency of V79 cell inactivation (23).

4.3.4 Concluding remarks

In summary, we demonstrate that sensitizer redistribution, as observed during irradiation of treated monolayer cultured cells, possibly leads to the onset of a second $^3O_2$ consumption phase in a fluence dependent manner. The appearance of the second phase indicates that the initially aggregated form of the dye is less efficient in photodynamic $^3O_2$ consumption, since only upon its release into the cytosol is $^3O_2$ consumption optimized. Finally, it is worth noting that these measurements demonstrate that photodynamic $^3O_2$ consumption is a very sensitive indicator not only of the changes in $^3O_2$ concentration that occur during treatment, but also of the changes in the effective concentration of photodynamically active sensitizer.

References

1. Gomer, C.J. (1991) Preclinical examination of first and second generation photosensitizers used in photodynamic therapy. *Photochem. Photobiol.* **54**, 1093-1107.

2. Boyle, R.W. and D. Dolphin (1996) Structure and biodistribution relationships of photodynamic sensitizers. *Photochem. Photobiol.* **64**, 469-485.

3. Berg., K. and J. Moan (1997) Lysosomes and microtubules as targets for photochemotherapy of cancer. *Photochem. Photobiol.* **65**, 403-409.

4. Santus., R., C. Kohen, E. Kohen, J.P. Reyftmann, P. Morliere, L. Dubertret and P.M. Tocci (1983) Permeation of lysosomal membranes in the course of photosensitization with methylene blue and hematoporphyrin: study by cellular microspectrofluorometry. *Photochem. Photobiol.* **38**, 71-77.

5. Berg, K., K. Madslien, J.C. Bommer, R. Oftebro, J.W. Winkelman and J. Moan (1991) Light induced relocalization of sulfonated meso-tetraphenylporphines in NHIK 3025 cells and effects of dose fractionation. *Photochem. Photobiol.* **53**, 203-210.

6. Berg, K., K. Prydz and J. Moan (1993) Photochemical treatment with the lysosomally localized dye tetra(4-sulfonatophenyl)porphine reults in lysosomal release of the dye but not of β-N-acetyl-D-glucosaminidase activity. *Biochim. Biophys. Acta* **1158**, 300-306.

7. Berg, K. and J. Moan (1994) Lysosomes as photochemical targets. *Int. J. Cancer* **59**, 814-822.

8. Moan, J., K. Berg, H. Anholt and K. Madslien (1994) Sulfonated aluminium phthalocyanines as sensitizers for photochemotherapy. Effects of small light doses on localization, dye fluorescence and photosensitivity in V79 cells. *Int. J. Cancer* **58**, 865-870.

9. Lin, C., J.R. Shulok, Y. Wong, C.F. Schanbacher, L. Cincotta and J.W. Foley (1991)

    Photosensitization, uptake, and retention of phenoxazine nile blue derivatives in

    human bladder carcinoma cells. *Cancer Res.* **51**, 1109-1116.

10. Lin, C., J.R. Shulok, S.D. Kirley, L. Cincotta and J.W. Foley (1991) Lysosomal

    localization and mechanism of uptake of nile blue photosensitizers in tumor cells.

    Cancer Res. **51**, 2710-2719.

11. Lin, C., J.R. Shulok, S.D. Kirley, C.M. Bachelder, T.J. Flotte, M.E. Sherwood, L.

    Cincotta and J.W. Foley (1993) Photodynamic destruction of lysosomes mediated

    by nile blue photosensitizers. *Photochem. Photobiol.* **58**, 81-91.

12. Lin, C. and J.R. Shulok (1994) Enhancement of nile blue derivative-induced

    photocytotoxicity by nigericin and low cytoplasmic pH. *Photochem. Photobiol.* **60**,

    143-146.

13. Desjardins, M., L.A. Huber, R.G. Parton and G. Griffiths (1992) Biogenesis of

    phagolysosomes proceeds through a sequential series of interactions with the

    endocytic apparatus. *J. Cell Biology* **124**, 677-688.

14. Ince, C., J.T. van Dissel and M.M.C. Diesselhoff (1985) A teflon culture dish for

    high-magnification microscopy and measurements in single cells. *Pflügers Archiv.*

    403, 240-244.

15. Georgakoudi, I. and T.H. Foster. (1998) Singlet oxygen- versus nonsinglet oxygen-

    mediated mechanisms of sensitizer photobleaching and their effects on photodynamic

dosimetry. *Photochem. Photobiol.* In Press.

16. Cincotta, L., J.W. Foley and A.H. Cinotta (1993) Phototoxicity, redox behavior, and pharmacokinetics of benzophenoxazine analogues in EMT-6 murine sarcoma cells. *Cancer Res.* **53**, 2571-2580.

17. Crow, E.L., F.A. Davis and M.W. Maxfield (1960) *Statistics Manual.* Dover Publications, Inc. New York, NY.

18. Peng, Q., G.W. Farrants, K. Madslien, J.C. Bommer, J. Moan, H.E. Danielsen and J.M. Nesland (1991) Subcellular localization, redistribution and photobleaching of sulfonated aluminum phthalocyanines in a human melanoma cell line. *Int. J. Cancer* **49**, 290-295.

19. Rück, A., T. Köllner, A. Dietrich, W. Strauss and H. Schneckenburger (1992) Fluorescence formation during photodynamic therapy in the nucleus of cells incubated with cationic and anionic water-soluble photosensitizers. *J. Photochem. Photobiol. B: Biol.* **12**, 403-412.

20. Malik, Z., I. Amit and C. Rothmann (1997) Subcellular localization of sulfonated tetraphenyl porphines in colon carcinoma cells by spectrally resolved imaging. *Photochem. Photobiol.* **65**, 389-396.

20. Wood, S.R, J.A. Holroyd and S.B. Brown (1997) The subcellular localization of Zn(II) phthalocyanines and their redistribution on exposure to light. *Photochem. Photobiol.* **65**, 397-402.

21. Ma, L., J. Moan and K. Berg (1994) Evaluation of a new photosensitizer, meso-

tetra-hydroxyphenyl-chlorin, for use in photodynamic therapy: a comparison of its photobiological properties with those of two other photosensitizers. *Int. J. Cancer* **57**, 883-888.

22. Berg, K., H. Anholt, J. Moan, A. Rønnestad and C. Rimington (1993) Photobiological properties of hematoporphyrin diesters: evaluation for possible application in photochemotherapy of cancer. *J. Photochem. Photobiol. B: Biol.* **20**, 37-45.

23. Berg, K., J. Bommer and J. Moan (1989) Evaluation of sulfonated aluminum phthalocyanines for use in photochemotherapy. A study on the relative efficiencies of photoinactivation. *Photochem. Photobiol.* **49**, 587-594.

Chapter 5

Hypoxia Significantly Reduces Aminolevulinic Acid-Induced Protoporphyrin IX Synthesis in EMT6 Cells

5.1 Introduction

As mentioned in chapter 1, PpIX is an endogenous sensitizer that is synthesized in excess amounts by cells when one of its precursors, ALA, is administered exogenously. As several steps are involved in the biosynthetic pathway of PpIX from ALA, there are various factors that could affect the production of this dye. A number of studies

investigating the role of some of these parameters are mentioned in chapter 1. The main aim of our study was to investigate the role of hypoxia in PpIX production by EMT6 cells.

It has been shown that the mean oxygen tension of several tumors is lower than that of the corresponding normal tissue (1). In addition, the variability of oxygen tension within several types of tumors is well documented (1). Therefore, if oxygen availability affects PpIX synthesis, tumor heterogeneities in oxygen tension could result in corresponding differences in PpIX concentration and in the efficacy of tumor treatment or detection. A recent study by Wyld *et al.* (2) examined the effects of hypoxia on PpIX production by exponentially growing bladder cancer cells. In an attempt to simulate some of the different growth states of cells present in a tumor, we studied the effects of hypoxia on PpIX production for three cell populations: a) low density exponentially growing cells, included for comparison with other *in vitro* studies, b) high density fed-plateau cells, representing populations in close proximity to capillaries and c) high density unfed-plateau cells, simulating the quiescent populations present in regions further away from capillaries. We find that ALA incubation of cells under hypoxia results in a significant decrease in PpIX synthesis, irrespective of cell density or growth phase. However, the magnitude of the effect is not the same for all populations. Specifically, the high density unfed-plateau cells experience the largest decrease in PpIX production, followed by the high density fed-plateau cells, which in turn are affected more than the low density exponential population.

5.2 Experimental procedures

5.2.1 Chemicals and reagents

Aminolevulinic acid hydrochloride was purchased from Porphyrin Products (Logan, UT). Solutions of 1 mM ALA were prepared fresh for each experiment by dissolving 8.7 mg ALA in 50 mL sterile Eagle's basal medium (BME). Cell culture media and antibiotics were purchased from GIBCO (Grand Island, NY); fetal Bovine Serum (FBS) was purchased from Atlanta Biologicals (Atlanta, GA); glucose oxidase and RNase were purchased from Sigma Chemical Co. (St. Louis, MO); and propidium iodide was purchased from Molecular Probes (Eugene, OR).

5.2.2 Cell maintenance and culture

EMT6 cells were maintained in passage culture in 100 mm diameter polystyrene dishes (Becton Dickinson, Franklin Lakes, NJ) in 10 mL BME supplemented with 10% FBS, 50 units/mL penicillin g, 50 μg/mL streptomycin and 1.0 mg/mL Fungizone® (complete BME). Cultures were maintained at 37°C in a 95% air-5% CO_2 humidified atmosphere. Three different cell populations were used: a) low density exponentially growing cells, b) high density fed-plateau cells, and c) high density unfed-plateau cells. To establish the low density exponential cells, 3×10^5 cells from passage culture were seeded on 100 mm diameter polystyrene culture dishes. Two days later, 1×10^5 cells from the subsequent population were transferred to 60 mm glass Pyrex brand petri dishes (VWR Scientific

Products, Rochester, NY) containing 5 mL complete BME. Glass dishes ensured that

oxygen could not diffuse into the cells from the plate walls when cells were incubated

under hypoxic conditions. The experiment was performed two days after the final seeding,

and the medium was replaced once for these cells on the intervening day. The high density

populations were established by seeding 3.6×10^6 cells from passage culture on 60 mm

glass petri dishes containing 5 mL complete BME seven days before the experiment. For

the fed-plateau population, the medium was changed for the first time three days

following the seeding and every subsequent day until the experiment. The medium of the

high density unfed-plateau cells was changed only once three days following the seeding.

5.2.3 DNA staining assay

The assay performed to determine the growth phase of the cell populations has been

described previously (3). Briefly, on the day of the experiment two or four dishes were

selected randomly from each one of the cell populations studied. The cells were removed

from the plates by trypsinization (0.25% lyophilized trypsin in sterile distilled water),

transferred to a 15 mL tube and centrifuged for 5 min at 1,000 rev/min. The supernatant

was aspirated and the pellet was dissolved in 1 mL complete BME. A 30 μL sample was

used for cell counting with a particle counter (Model ZM, Coulter Electronics, Hialeah,

FL). Two million cells were fixed in 6 mL 75% ethyl alcohol and stored at 4°C for at least

24 hours. Following fixation, the cells were treated with 1 mL RNase (1 mg/mL in 1X

phosphate buffered saline) for 30 min at room temperature and centrifuged for 7 min at

1,000 rev/min. After the addition of 750 μL propidium iodide (10 μg/mL in 1X phosphate

buffered saline), each sample was filtered through a 37 μm mesh and its cellular DNA

content was analyzed using an EPICS Profile flow cytometer (Coulter Electronics). The

percentage of cells in each of the cell cycle phases was determined by using the Multicycle

AV commercial software package (Phoenix Flow System, San Diego, CA).

5.2.4 ALA administration under hypoxic conditions

Initially, the media of all samples were replaced by 3 mL fresh BME. We decreased the

oxygen tension in the medium by introducing 270 μL glucose oxidase (20 units/mL

dissolved in distilled water) and placing the dishes in an evacuation chamber that was

sparged every 20 min with 95% N_2-5% CO_2. The chamber was in a warm room with the

temperature maintained at 37°C. The oxygen tension, monitored for one sample with an

oxygen sensitive microelectrode (Microelectrodes, Inc., Londonderry, NH) calibrated in

BME and BME with glucose oxidase, decreased to a value smaller than 0.4% within 40

min of incubation in the chamber. Following exposure to hypoxia for 1 h, the evacuation

chamber was opened, and the medium of the samples was replaced by either 3 mL fresh

BME and 270 μL glucose oxidase (controls) or by 3 mL fresh BME containing 1 mM

ALA and 270 μL glucose oxidase. The plates were placed again in the evacuation

chamber and intermittent sparging with 95% N_2-5% CO_2 was performed every 20 min for

2 hours. Following a total ALA incubation time of 4 h in the dark, the cells were removed

from the evacuation chamber and treated in the same manner as those sensitized with

ALA under normoxic conditions.

5.2.5 ALA administration under normoxic conditions

To maintain consistency with the protocol followed for ALA administration under

hypoxic conditions, the samples' media were replaced initially by 3 mL BME. After an

hour, they were replaced again by either 3 mL BME (controls) or 3 mL BME containing

1 mM ALA and 270 μL BME without ALA to ensure that the cells were treated with

equal concentrations of ALA under normoxic and hypoxic conditions. These samples

were incubated in a 95% air-5% CO_2 atmosphere at 37°C for 4 h in the dark.

5.2.6 Quantification of cellular PpIX content

Following incubation either in BME or in ALA, each sample was washed once with 1 mL

minimal essential medium without phenol red (MEM) and treated with 0.5 mL 0.25%

trypsin until the cells started detaching from the plates. The trypsinization process was

halted by the addition of 2.5 mL MEM containing 10% FBS and the cells were transferred

to a 15 mL tube. After centrifugation for 5 min at 1,000 rev/min, the supernatant was

aspirated and different amounts of MEM were added to the low density exponential (0.5

mL), high density fed-plateau (4.5 mL), and high density unfed-plateau (3.5 mL) cell

populations so that the resulting cell suspensions would have approximately equal cellular

concentrations (about 7.5×10^5 cells/mL). A 100 μL sample from each tube was diluted

in 20 mL saline and used to count the exact number of cells corresponding to each one

of the dishes that were treated with BME or ALA. 350 μL from each cell sample were

pipetted into a microcell (SPEX Industries, Edison, NJ) and the front face fluorescence

spectrum was recorded by a spectrofluorometer (Fluorolog 2, SPEX Industries). The

excitation wavelength was set at 405 nm, the integration time was 0.5 s, the resolution

was 1 nm and fluorescence was detected from 550 to 730 nm. It should be noted that

following trypsinization, the cell samples remained in ice during the time they were not

handled. The PpIX content of the incubation medium was not measured because it did not

contain serum; a previous study has shown that only a minimal amount of PpIX leaks out

of the cells when ALA incubation occurs in the absence of serum (4).

Individual experiments were performed either with low density exponential and

high density unfed-plateau cells or with high density fed-plateau cells. Half of the samples

from each population were treated under normoxic conditions, while the other half were

treated under hypoxic conditions. For each of the three experiments with the low density

exponential and high density plateau cells, we had four dishes for each treatment group:

two of the them served as controls (incubated with BME) and the other two were

incubated with ALA. During the experiment performed with the high density exponential

cells, eight dishes were incubated under normoxic conditions and eight were incubated

under hypoxic conditions. Two samples in each group were treated with BME (controls)

while the other six were treated with ALA.

5.2.7 Statistical analysis

The equal tails Student's t test (5) was used to determine statistical differences in the mean values of the normalized peak PpIX fluorescence signal (634 nm) corresponding to each one of the cell populations studied.

5.3 Results

Shown in Figure 5.1 are representative DNA content histograms obtained from flow cytometric analysis of propidium iodide stained cells from the three cell populations considered. The percentage of cells in the S phase of the cell cycle, *i.e.* the phase during which DNA is synthesized, was used as an indicator of the proliferating status of the population. These percentages are 42.15 ± 6.7 (n=6), 34.9 ± 2.4 (n=4), and 11.9 ± 2.3 (n=6) for the low density exponential (Figure 5.1a), high density fed-plateau (Figure 5.1b), and high density unfed-plateau cells (Figure 5.1c), respectively (mean $\pm$ standard deviation reported).

PpIX spectra corresponding to the three cell populations treated with 1 mM ALA for 4 h under normoxic (Figure 5.2a) and hypoxic (Figure 5.2b) conditions are displayed in Figure 5.2. The background fluorescence, *i.e.* the fluorescence not associated with ALA-induced fluorophores, is considered to be the same as the spectrum obtained from the control samples. Thus, we subtract the spectrum of a control sample from the spectrum of the corresponding ALA-treated group and divide it by the number of cells
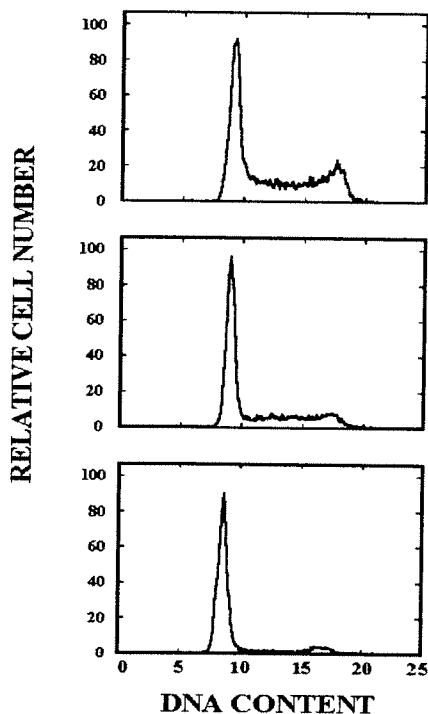
Figure 5.1: Representative DNA content histograms obtained by flow cytometric analysis of propidium iodide stained cells from: A) the low density exponential population, B) the high density fed-plateau population, and C) the high density unfed-plateau population. The percentage of cells in the S phase as determined by a curve fitting algorithm is 42.15 ± 6.7, 34.9 ± 2.4, and 11.9 ± 2.3 for (A), (B), and (C), respectively (mean ± standard deviation from at least four different measurements is reported in each case). The coefficient of variance for the G1 peaks was less than 5% for all cases.

in the sample to obtain each one the spectra shown in Figure 5.2. We should note that the

autofluorescence spectra from all of the control samples were very similar, regardless of

incubation conditions, cell density or proliferation rate (data not shown). The characteris-

tic PpIX peak at approximately 634 nm is present in all spectra, while the lower intensity

peak at 705 nm is not clearly visible for the high density unfed-plateau cells treated with

ALA under hypoxia due to the low overall PpIX fluorescence intensity detected in this

case. We observe that the intensity of PpIX fluorescence is dependent on cell density and

proliferation rate. More importantly, we find that hypoxia affects PpIX production in very

significant ways.

These trends are displayed in a more quantitative manner in Figure 5.3. For each

experiment, the background subtracted peak PpIX fluorescence per cell from each sample

is normalized to that of one of the low density exponential populations treated with ALA

under normoxic conditions. Thus, the normalized peak PpIX fluorescence per cell of the

normoxic low density exponential group approaches unity. When cells are treated with

ALA under normoxic conditions, we find that the normalized peak PpIX fluorescence of

the high density fed-plateau population (3.1 ± 0.4) is not statistically different from that

of the high density unfed-plateau population (2.5 ± 0.9) for $P < 0.05$. The peak PpIX

fluorescence of both high density plateau populations is higher than that of the low density

exponential group (0.98 ± 0.03; $P < 0.01$). However, when cells are treated with ALA

under hypoxia, we find that the normalized peak PpIX fluorescence per cell produced by

the low density exponential cells (0.7 ± 0.2) is statistically higher than that of the high
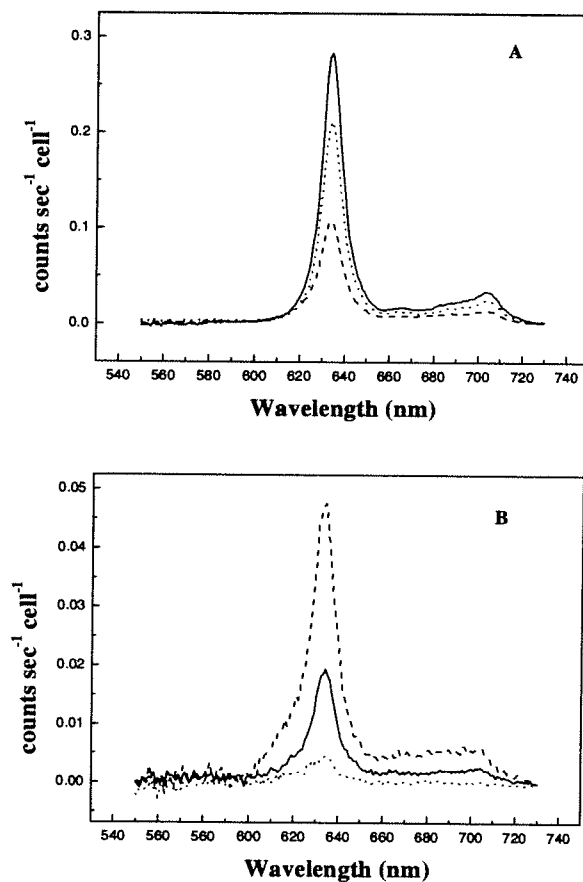
Figure 5.2: Representative background subtracted PpIX spectra obtained from whole cell

samples treated with 1 mM ALA for 4 hours under (A) normoxic or (B) hypoxic

conditions. Spectra from the high density fed-plateau (——————), high density unfed-plateau

(·········), and low density exponential (- - - - -) populations are shown in each panel. The

characteristic PpIX peak at 634 nm is present in all spectra, but the 705 nm peak is not

detectable for the hypoxic high density plateau population due to the overall decrease in

the fluorescence.
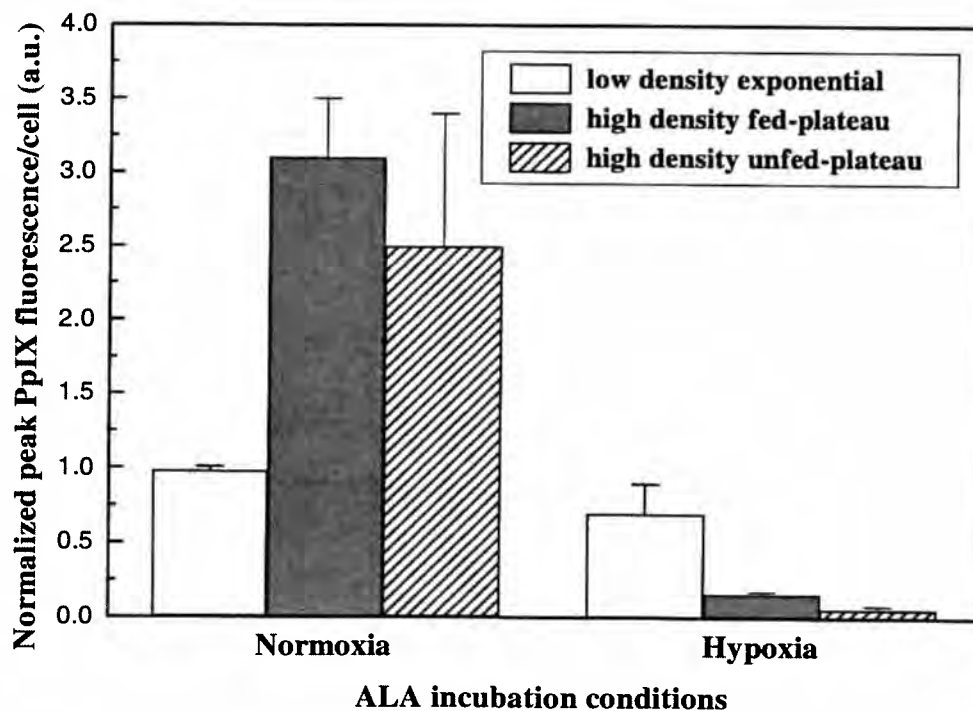
Figure 5.3: Hypoxia significantly affects PpIX synthesis for all populations considered. The magnitude of this effect is dependent on cell density and proliferation rate. The normalized peak PpIX fluorescence/cell is 2.5 ± 0.9, 3.1 ± 0.4, and 0.98 ± 0.03 for the normoxic high density unfed-plateau, high density fed-plateau, and low density exponential cells, respectively. The normalized peak PpIX fluorescence for these populations, in the same order, treated with ALA under hypoxic conditions is 0.06 ± 0.02, 0.16 ± 0.015, and 0.7 ± 0.2, respectively (mean ± standard deviations reported; n=6).

density fed-plateau population (0.16 ± 0.015; $P < 0.01$), which in turn is higher than that

of the high density unfed-plateau group (0.06 ± 0.02; $P < 0.01$). (In each case, the mean

$\pm$ standard deviation is reported; $n=6$.) The units reported are arbitrary as the purpose of

this study was to examine in a qualitative manner the effects of hypoxia. Therefore, a

calibration curve that could possibly allow us to quantitate the absolute intracellular PpIX

concentrations was not obtained.

5.4 Discussion

5.4.1 The dependence of PpIX synthesis on the population cell density and proliferation status under normoxic ALA incubation conditions

Our whole cell fluorescence spectroscopy studies indicate that under normoxic ALA

incubation conditions cell density is a factor that affects PpIX synthesis. Specifically, we

find that the high density populations produce substantially higher amounts of PpIX per

cell than the low density population. These results agree with fluorescence microscopy

and flow cytometry studies performed by Moan et al. (6) with human colon adenocarci-

noma cells and Chinese hamster lung fibroblasts. Steinbach et al. (7) observed an

increasing amount of PpIX fluorescence with increasing cell density for two malignant and

a normal urothelial cell line. However, cell density had no effect on PpIX production by

N1 normal fibroblasts. Moreover, cell confluency was not an important determinant of

PpIX production in human skin fibroblasts (8). Therefore, it appears that the effects of cell density on PpIX production could be cell line dependent. However, it is interesting to note that all of the malignant cell lines studied exhibit a similar cell confluency dependence.

When we compare PpIX synthesis by the two high density populations under normoxic ALA incubation conditions we find that there are not any significant differences between the fed-plateau and the unfed-plateau cells, even though their corresponding proliferation rates are very different as indicated by the percentage of cells in the S phase for each group. These results are in agreement with studies performed by Fukuda *et al.* (9) showing that there is little obvious cell cycle dependence on PpIX generation by CNCM-I-221 mammalian epithelial cells. Moan *et al.* (6) have reported that the only cell cycle dependence of PpIX synthesis appears to be a simple volume dependence, with cells in the G2+M phases producing 1.9 times more PpIX than cells in the G1 phase. The higher mean PpIX fluorescence for the fed-plateau population could be explained by cell size-dependent PpIX production; however, our experiments suggest that the differences in the number of cells corresponding to each cell cycle phase for the high density fed-plateau and unfed-plateau cells are not significant enough to result in statistically different PpIX fluorescence measurements. Iinuma *et al.* (10) and Momma *et al.* (11) have found also that the PpIX content of several malignant cell lines did not correlate with their different growth rates. Wyld *et al.* (12) reported similar results with six different cell lines that included fibroblasts, smooth muscle, endothelial and malignant cells. However, they

noted that the plateau populations of three non-malignant cell lines contained a reduced intracellular amount of PpIX as compared to the exponential populations, while the reverse was true for the two malignant cell lines that were included. As the confluency levels were different for the exponential and plateau populations it is not clear whether the observed differences are a result of variation in cell densities or cell proliferation rates. The effects of cell stimulation by different factors on PpIX synthesis have been investigated as well. Schick *et al.* (13) found that while stimulation of normal human keratinocytes with EGF-alpha, a cytokine stimulating the proliferation of epidermal and epithelial cells, resulted in higher cytotoxicities with ALA-PDT, activation of two skin squamous cell carcinoma lines did not have any effects. Rebeiz *et al.* (14) observed a significant increase in PpIX accumulation when resting splenocytes were activated with the mitogenic lectin concavalin A. A similar effect was reported by Rittenhouse-Diakun *et al.* (15) when human peripheral blood lymphocytes were stimulated with three different mitogens. Thus, it appears that cell proliferation rate could affect PpIX synthesis, depending on the cell line.

It is possible that the slight decrease in PpIX production by the unfed-plateau cells as compared to that of the fed-plateau cells is due to small pH differences between the two populations induced by the different tissue culture protocols that were followed to establish them. However, we did not observe any significant color changes of the cells' media at the time they were harvested for the experiment. Studies reported by Bech *et al.* (16) and Wyld *et al.* (2) demonstrating that pH can affect PpIX synthesis were performed

with cells that were exposed to different pH values *during* incubation with ALA. As

mentioned in sections 5.2.4 and 5.2.5, in our experiments the cells were incubated with

fresh media an hour prior to and during ALA incubation. Therefore, we do not suspect

that any pH differences resulting from our tissue culture methods had a significant effect

on PpIX production during this study.

5.4.2 Effects of hypoxia on PpIX synthesis and the role of cell density and proliferation status in determining the magnitude of the effect

Both cell confluency and proliferation state are important determinants of the magnitude

of the effect of hypoxic ALA incubation on PpIX synthesis. Specifically, we find that

while PpIX production under hypoxic conditions decreases by a factor of 1.4 for low

density exponential cells, it decreases by approximately 20-fold for high density fed-

plateau cells and 42-fold for high density unfed-plateau cells. It was shown by Falk *et al.*

(17) that variations in oxygen tension significantly affect the production of heme,

protoporphyrin and coproporphyrin in whole blood cells from normal chickens. Recently,

Wyld *et al.* (2) reported that PpIX production by exponentially growing bladder cancer

cells was reduced significantly when ALA incubation was performed at 0%, 2.5%, and

5% oxygen conditions when compared to that at 21% oxygen. However, to our

knowledge the work presented in this report is the first systematic study of the effects of

hypoxia on ALA-induced PpIX production by cells at different proliferating states. The mechanisms that lead to decreased PpIX synthesis under hypoxic ALA incubation conditions remain to be studied. It is possible that ALA uptake is affected. It has been reported by Bermudez-Moretti *et al.* (18) that an active mechanism is involved in ALA transport in saccharomyces cerevisiae. However, no temperature dependence was found in ^{14}C-ALA uptake by malignant human mammary and mesothelioma cells or by rat mammary adenocarcinoma cells suggesting that an energy-dependent carrier is not involved (19). Hypoxia could lead to decreased synthesis or activity of the enzymes that are involved in the heme biosynthetic pathway. The absence of any detectable changes in the shape of the recorded fluorescence spectra prevents us from suggesting any enzymes that could be affected in particular by limited oxygen availability. However, Sano and Granick (20) have reported that coproporphyrinogen oxidase requires oxygen to act upon coproporphyrinogen. Moreover, Poulson and Polglase (21) and Poulson (22) have shown that oxygen is essential for protoporphyrinogen oxidase activity, the enzyme catalyzing the oxidation of protoporphyrinogen IX to protoporphyrin IX. If excess protoporphyri-nogen IX produced as a result of decreased protoporphyrinogen oxidase activity leaked from the mitochondria into the cytosol, it could be converted to PpIX when the cells were reoxidized during preparation for the spectrofluorometry studies (23). Thus, the actual decrease in PpIX synthesis under hypoxia could be even more dramatic than our current estimates. Changes in the cellular glucose content could also be a factor, as glucose concentration has been reported by Dietel *et al.* (24) to affect PpIX synthesis. We should

note that the addition of glucose oxidase in the medium to induce a rapid decrease in oxygen concentration should not affect the glucose concentration of the medium (5.5 mM) because only approximately 240 µM glucose would be consumed in the process.

It is not clear why different cell densities and proliferation rates result in different hypoxic effects on PpIX production. A cell density-dependent modulation of genes that encode rate limiting enzymes such as porphobilinogen deaminase and ferrochelatase has been suggested by Moan et al. (6). This modulation could lead to increased PpIX synthesis with increasing cell density under normoxic ALA incubation conditions, but have the opposite effect under hypoxic conditions. It is possible that a decreased iron content in exponentially growing cells could explain why they produce more PpIX than the plateau cells under hypoxia, since decreased cellular iron content has been correlated with increased PpIX accumulation (4, 15, 25). However, this hypothesis is not consistent with the level of PpIX synthesis that we observe for the different cell populations under normoxic ALA incubation conditions.

5.4.3 Concluding remarks

In conclusion, this report demonstrates that hypoxia significantly affects PpIX production in EMT6 monolayer cultures. The effects of hypoxia appear to be dependent on cell density and proliferation status. If the trends observed with our monolayer cultures are relevant to the in vivo situation, then our results would suggest that the efficacy of PpIX

as a photodynamic and fluorescence detection agent might be compromised in tumor regions that are hypoxic. Such effects should be considered when designing efficient tumor treatment or diagnostic protocols.

References

1. Vaupel, P., F. Kallinowski and P. Okunieff (1989) Blood flow, oxygen and nutrient supply, and metabolic microenvironment of human tumors: a review. *Cancer Res.* **49**, 6449-6465.

2. Wyld, L., M.W.R. Reed and N.J. Brown (1998) The influence of hypoxia and pH on aminolaevulinic acid-induced photodynamic therapy in bladder cancer cells in vitro. *Br. J. Cancer* **77**, 1621-1627.

3. Tsai, M.A., R.E. Waugh and P.C. Keng (1996) Cell cycle-dependence of HL-60 cell deformability. *Biophys. J.* **70**, 2023-2029.

4. Hanania, J. and Z. Malik (1992) The effect of EDTA and serum on endogenous porphyrin accumulation and photodynamic sensitization of human K562 leukemic cells. *Cancer Letters* **65**, 127-131.

5. Crow, E.L., F.A. Davis and M.W. Maxfield (1960). *Statistics Manual.* Dover Publications, Inc.: New York, NY.

6. Moan, J., Ø. Bech, J.-M. Gaullier, T. Stokke, H.B. Steen, L.W. Ma and K. Berg (1998) Protoporphyrin IX accumulation in cells treated with 5-aminolevulinic

acid: dependence on cell density, cell size and cell cycle. *Int. J. Cancer* **75**, 134-139.

7.   Steinbach, P., H. Weingandt, R. Baumgartner, M. Kriegmair, F. Hofstädter and R. Knüchel (1995) Cellular fluorescence of the endogenous photosensitizer protoporphyrin IX following exposure to 5-aminolevulinic acid. *Photochem. Photobiol.* **62**, 887-895.

8.   Krammer, B. and K. Überriegler (1996) In-vitro investigation of ALA-induced protoporphyrin IX. *J. Photochem. Photobiol. B: Biol.* **36**, 121-126.

9.   Fukuda, H., A.M.C. Batlle and P.A. Riley (1993) Kinetics of porphyrin accumulation in cultured epithelial cells exposed to ALA. *Int. J. Biochem.* **25**, 1407-1410.

10. Iinuma, S., S.S. Farshi, B. Ortel and T. Hasan (1994) A mechanistic study of cellular photodestruction with 5-aminolevulinic acid-induced porphyrin. *Br. J. Cancer* **70**, 21-28.

11. Momma, T., M.R. Hamblin and T. Hasan (1997) Hormonal modulation of the accumulation of 5-aminolevulinic acid-induced protoporphyrin and phototoxicity in prostate cancer cells. *Int. J. Cancer* **72**, 1062-1069.

12. Wyld, L., J.L. Burn, M.W.R. Reed and N.J. Brown (1997) Factors affecting aminolaevulinic acid-induced generation of protoporphyrin IX. *Br. J. Cancer* **76**, 705-712.

13. Schick, E., R. Kaufmann, A. Rück, A. Hainzl and W.-H. Boehncke (1995) Influence of activation and differentiation of cells on the effectiveness of photodynamic therapy. *Acta Derm. Venereol.* **75**, 276-279.

14. Rebeiz, N., C.C. Rebeiz, S. Arkins, K.W. Kelley and C.A. Rebeiz (1992) Photodestruction of tumor cells by induction of endogenous accumulation of protoporphyrin IX: enhancement by 1,10-phenanthroline. *Photochem. Photobiol.* **55**, 431-435.

15. Rittenhouse-Diakun, K., H. van Leengoed, J. Morgan, E. Hryhorenko, G. Paszkiewicz, J.E. Whitaker and A.R. Oseroff (1995) The role of transferrin receptor (CD71) in photodynamic therapy of activated and malignant lymphocytes using the heme precursor δ-aminolevulinic acid (ALA). *Photochem. Photobiol.* **61**, 523-528.

16. Bech, Ø., K. Berg and J. Moan (1997) The pH dependency of protoporphyrin IX formation in cells incubated with 5-aminolevulinic acid. *Cancer Letters* **113**, 25-29.

17. Falk, J.E., R.J. Porra, A. Brown, F. Moss and H.E. Larminie (1959) Effect of oxygen tension on hæm and porphyrin biosynthesis. *Nature* **184**, 1217-1219.

18. Bermúdez Moretti, M., S. Correa García, C. Stella, E. Ramos and A.M.C. Del C. Batlle (1993) δ-aminolevulinic acid transport in saccharomyces cerevisiae. *Int. J. Biochem.* **25**, 1917-1924.

19. Gibson, S.L., J.J. Havens, T.H. Foster and R. Hilf (1997) Time-dependent intracellular accumulation of δ-aminolevulinic acid, induction of porphyrin synthesis and subsequent phototoxicity. *Photochem. Photobiol.* **65**, 416-421.

20. Sano, S. and S. Granick (1961) Mitochondrial coproporphyrinogen oxidase and protoporphyrin formation. *J. Biol. Chem.* **236**,1173-1180.

21. Poulson, R. and W.J. Polglase (1975) The enzymic conversion of protoporphyrinogen IX to protoporphyrin IX. *J. Biol. Chem.* **250**, 1269-1274.

22. Poulson, R. (1976) The enzymic conversion of protoporphyrinogen IX to protoporphyrin IX in mammalian mitochondria. *J. Biol. Chem.* **251**, 3730-3733.

23. Fingar, V.H., T.J. Wieman, K.S. McMahon, P.S. Haydon, B.P. Halling, D.A. Yuhas and J.W. Winkelman (1997) Photodynamic therapy using a protoporphyrinogen oxidase inhibitor. *Cancer Res.* **57**, 4551-4556.

24. Dietel, W., K. Bolsen, E. Dickson, C. Fritsch, R. Pottier and R. Wendenburg (1996) Formation of water-soluble porphyrins and protoporphyrin IX in 5-aminolevulinic-acid-incubated carcinoma cells. *J. Photochem. Photobiol. B: Biol.* **33**, 225-231.

25. Tan, W.C., N. Krasner, P. O'Toole and M. Lombard (1997) Enhancement of photodynamic therapy in gastric cancer cells by removal of iron. *Gut* **41**, 14-18.

Chapter 6

Design and Characterization of a Laser Beam Scanning Confocal Microscope

6.1 Confocal microscopy: basic principles and applications

Confocal microscopy is a technique that leads to superior lateral and axial resolution over conventional microscopy as out-of-focus light is rejected by a small aperture (pinhole) placed typically in front of the detector (Figure 6.1). In the lateral direction the resolution depends on the product of the point spread functions of the condenser and objective lenses, not on the point spread function of the objective only, allowing for an improvement in resolution of up to a factor of 1.4 (1). However, confocal microscopy is mainly used for its ability to provide superior resolution in the axial direction (2). It is
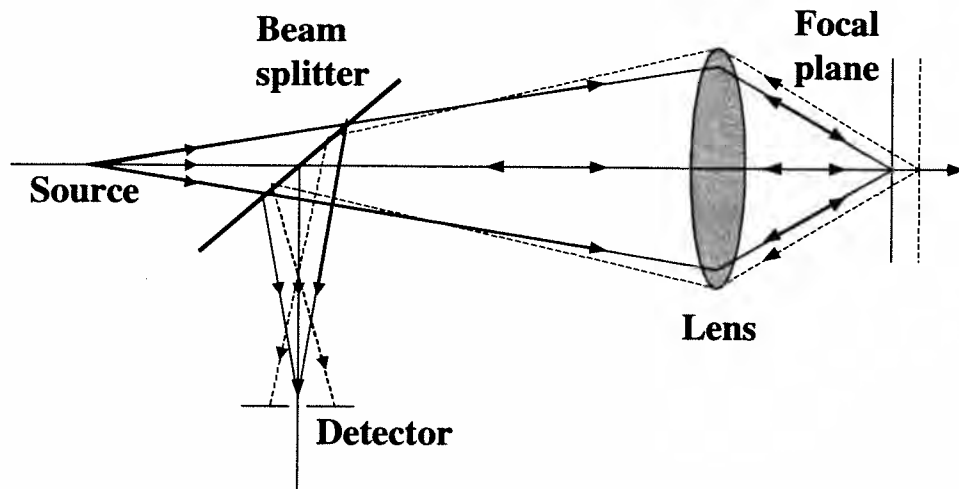
Figure 6.1: Schematic explanation of the depth discrimination property of the confocal

scanning optical microscope. Reproduced from Wilson and Carlini (2).

this optical sectioning ability of confocal microscopy that makes it ideal for imaging through thick specimens such as spheroids (3).

The main disadvantage of confocal microscopy is that only a very limited region of the sample can be imaged at a time. Therefore, scanning is necessary to obtain an image of the full specimen. Tandem scanning, stage scanning, and beam scanning are the three most popular techniques used to scan a sample (4). Beam scanning is the technique that is used most frequently for confocal imaging of biological samples as, unlike stage scanning, it is fast and allows the specimen to remain stationary during scanning, and it is not limited by the low light transmission efficiency problems of tandem scanning. A beam scanning confocal microscope has been constructed in our laboratory for the purpose of imaging optical sections of sensitized multicell tumor spheroids. Unfortunately, beam scanning is not a cure all for confocal microscopy of biological specimens, and some of the problems that must be resolved before quantitative imaging is achieved are discussed later in this section.

Confocal imaging is performed either in reflectance or in fluorescence mode. Even though the confocal attachment that we constructed in our laboratory was designed for fluorescence measurements, our system can be modified easily to perform reflectance measurements. We should note that the performance of a confocal system in fluorescence is slightly worse than in reflectance, mainly because of the chromatic aberrations that arise from the differences in the wavelengths of the excitation and fluorescence light (5).

One of the main problems encountered in fluorescence confocal microscopy of

thick specimens is related to light attenuation. The excitation light intensity is attenuated with depth as some of the light becomes absorbed by fluorophores between the surface and the focal plane in the specimen, while the fluorescent light is attenuated as it becomes reabsorbed by fluorophores in the specimen, since in most cases the excitation and fluorescence spectra of the fluorophore partially overlap. Another serious issue that has to be considered in confocal microscopy of thick biological samples is the effect of light scattering on the intensity of excited and emitted light as well as on the resolution achieved as one attempts to image layers that lie deeper in the sample.

Confocal microscopy studies have been performed successfully with thick biological specimens by several investigators to study, for example, neuronal functions (6-8), nuclear DNA distributions (9-10), and antibody (11) and drug (12-13) penetration. Typically, these studies are performed either with thick tissue sections or multicell spheroids. However, *in vivo* confocal microscopy studies of the microcirculation of the rat brain (14-16) and transplanted pancreatic islets (17), the human skin (18-20) and cornea (21) have been reported also. Images with a resolution on the cellular level have been presented for depths of up to 350 μm (22). While in some studies empirical corrections for the effects of reabsorption, scattering and absorption are implemented, a few more rigorous, albeit more time-consuming, methods for modeling these processes are presented also.

In this chapter, we describe a laser scanning confocal microscope attachment to an inverted Nikon diaphot microscope, and we report on the resolution performance of

such a microscope for three different pinhole diameters. Images through EtNBS-sensitized spheroids demonstrate the optical sectioning capabilities of the instrument. Some of the issues that have to be resolved before we can obtain images that will allow us to study in a quantitative manner the processes of sensitizer photobleaching and localization are discussed.

6.2   Description of a laser scanning confocal microscope attachment

A schematic description of the system is shown in Figure 6.2, while part numbers of the various components are listed in Table 6.1. The beam of a He-Ne laser (Melles Griot Inc., Irvine, CA) is directed through an interference filter (Newport Corp., Irvine, CA) so that only the 632.8 nm line is transmitted. Once the beam is expanded to a diameter of approximately 3 mm using a Keplerian telescope lens arrangement (lenses L1 and L2), it goes through a dichroic mirror (DM) designed to have high transmittance at the excitation light wavelength and high reflectance at the longer fluorescence light wavelengths (for experiments performed with the Nile Blue sensitizers a dichroic with 50% transmission at 650 nm (Chroma Corp., Brattleboro, VT) is used). The beam is then directed to the fast scanning mirror (M1, General Scanning, Watertown MA) so that the axis of rotation of the mirror forms a 90 degree angle with the incoming beam to ensure that a straight line is scanned as the mirror moves. The beam is then focused by a
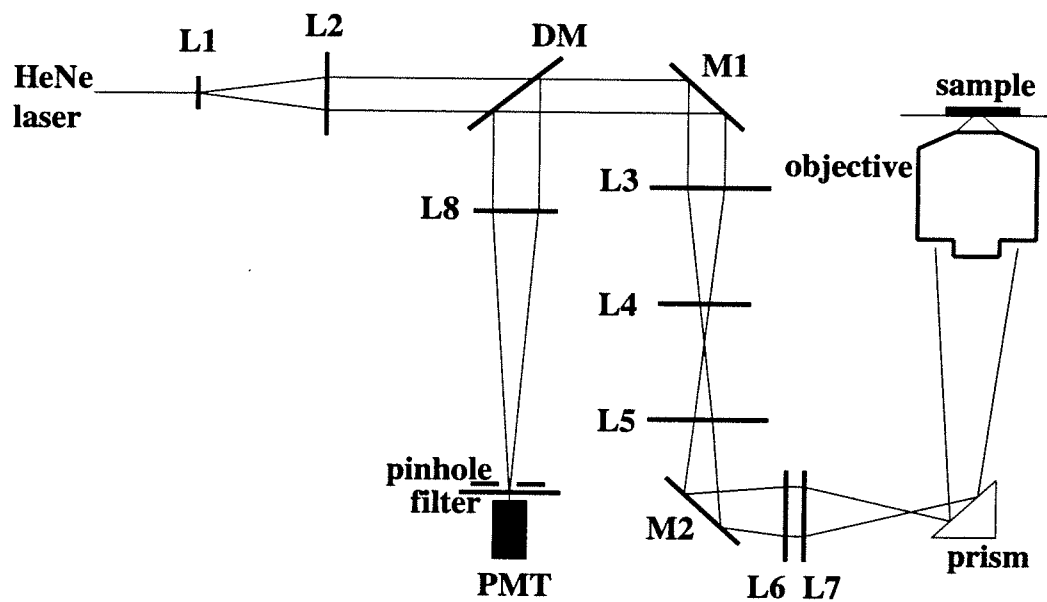
Figure 6.2: Schematic layout of laser beam scanning confocal attachment to an inverted

fluorescence microscope. For a description of the components refer to section 6.2 and

Table 6.1.

Table 6.1: Description of optical components for the confocal attachment

Component	Description	Focal length (mm)	Diameter (mm)	Manufacturer	Part number
L1	symmetric bi-convex lens	10	10	Melles Griot	01LDX009
L2	symmetric bi-convex lens	25	22.4	Melles Griot	01LDX035
DM	dichroic mirror	NA	NA	Chroma	650DCSP for Nile Blue studies
M1	scanning mirror	NA	NA	General Scanning	E10-082694
L3	plano-convex achromat	60	30	Melles Griot	01LAO079
L4	symmetric bi-concave lens	-200	30	Melles Griot	01LDK034
L5	plano-convex achromat	60	30	Melles Griot	01LAO079
M2	scanning mirror	NA	NA	General Scanning	E10-082714
L6, L7	plano-convex achromat	60	30	Melles Griot	01LAO079
L8	plano-convex achromat	250	30	Melles Griot	01LAO229
F	long pass filter	NA	38	Schott	RG665, 3 mm thick
PMT	photomulti-plier tube	NA	NA	Hamamatsu	HC120-05 module with R6357 tube

plano-convex achromat (L3) and re-expanded by an identical lens (L5) before it reaches

the second scanning mirror (M2, General Scanning). A symmetrical bi-concave lens (L4)

is positioned so that it intersects the light beam a few millimeters before it is focused

down to a spot by L3. The purpose of this lens is to correct partially for field curvature

errors introduced by lenses L3 and L5. This error refers to the fact that the plane that is

scanned at the focus of the objective is slightly curved in the direction of the optical axis

(*i.e.* the z direction). However, to achieve this correction to the field curvature by

introducing lens L4 we are no longer able to obtain a very well collimated beam from L5.

Lenses L3 and L5 direct the beam to exactly the same spot on the second scanning mirror

(M2), even when the first scanning mirror is scanning a line. In this manner, we can scan

an appreciable field (1mm x 1mm) without requiring that the two mirrors be

prohibitively close to each other. Besides, raster plane scanning systems that consist of

just the two scanning mirrors are known to suffer from significant pincushion effects

(23). After the beam is deflected from the second scanning mirror, it goes through two

achromats (L6 and L7) that are identical to L3 and L5. Thus, the excitation beam is

expanded to overfill the objective's aperture by approximately 50%. This essentially

flattens the Gaussian profile of the beam (*i.e.* the beam appears more like a plane wave)

improving the ability of the objective to focus the light to a diffraction limited spot. For

our measurements, a Nikon 10X Fluor objective with a numerical aperture (NA) of 0.5

and a working distance of 0.88 mm is used.

When the excitation light is focused onto a sample that contains fluorophores,

fluorescence is emitted isotropically. Part of this fluorescence is collected by the objective and directed back through the same set of lenses and mirrors as the incoming excitation beam to the dichroic mirror. There, the fluorescence light is reflected towards lens L8, which focuses the beam to a mounted pinhole. Only light excited at the focus of the objective will be focused onto the pinhole, while most of the out-of-focus light will be rejected. A pinhole holder (Melles Griot) allows fine adjustment of the pinhole in the x and y directions with a resolution of 10 µm, while its position in the z direction is adjusted by a fine translator (M-UMR3.5, resolution = 0.1 µm, Newport Corp.). Finally, the light that is transmitted though the pinhole is detected by a photomultiplier module with a 200 KHz bandwidth (Hamamatsu Corp., Bridgewater, NJ). The photomultiplier tube (PMT) output is directed to a PC *via* a 300 KHz, 12-bit data acquisition board that has digital to analog and analog to digital conversion capabilities (DT31E-Z, Data Translation, Marlboro, MA). An optical filter (F) is typically inserted between the pinhole and the PMT to further discriminate against back reflected excitation light.

The scanning mirrors are silver coated, mass balanced mirrors with a specified flatness of $\lambda/4$ (where λ is the wavelength of incident light). They are mounted on galvanometers (G120DT, General Scanning), and their position is controlled by two electronic boards (one for each mirror; AE1000, General Scanning) that are in turn connected to a PC through the same data acquisition board as the PMT.

Scanning in the axial (z) direction is controlled electronically *via* a z-axis

controller (990062, Ludl Electronic Products Ltd., Hawthorne, NY) with a focus drive motor attached to the fine focus of the microscope and a resolution of up to 100 nm. The software that controls scanning in x, y, and z and data acquisition from the PMT was developed by Andrey Mezhiba, a master's graduate student in our laboratory, using Labview 4.1 (National Instruments Corp., Austin, TX) as a platform. However, since addressing the data acquisition board with the Labview programming language was prohibitively slow, the code controlling mirror scanning and data acquisition from the PMT was written in Visual C++ and imported into the Labview program.

All the lenses were purchased from Melles Griot. All the elements of the confocal attachment are mounted on an optical table with the exception of lenses L6 and L7 which are inserted in the video port of the microscope. A black box made out of delrin encloses the pinhole and the PMT to minimize detection of background light by the detector. A small aperture, approximately 1 cm in diameter, allows the fluorescence light to reach the pinhole.

6.3   Resolution measurements

6.3.1 Axial resolution measurements in reflectance mode

The results of these measurements are summarized in Table 6.2. A mirror is placed at the microscope stage, and there is no filter present between the pinhole and the PMT for the reflectance experiments. The beam is directed at the center of the field of view (FOV)

**Table 6.2**: Summary of resolution measurements with three pinhole sizes

| Pinhole diameter	Axial resolution			Lateral resolution
	Reflectance	Fluorescence		Fluorescence
	FWHM	20%-80%	10%-90%	FWHM
200 µm	8.8 µm	10.3 µm	19.5 µm	≤ 1 µm
100 µm	6.8 µm	7.2 µm	14.8 µm	≤ 1 µm
50 µm	6.1 µm	6.2 µm	11.2 µm	≤ 1 µm

and the focus of the objective is scanned in the z direction in 0.5 μm increments. Initially,

the objective is focused below the surface of the mirror, and we detect no back reflected

light at the PMT. As the focus is moved closer to the mirror surface the detected signal

increases until it reaches a maximum. Then, as the objective starts to focus above the

plane of the mirror surface the signal decreases. The results of such measurements are

shown in Figure 6.3 for three pinhole diameters: 200, 100, and 50 μm. Note that the

shape of the back reflected signal intensity is not symmetrical. This asymmetry is

probably due to aberrations introduced by the optical elements of the system and has

been reported by others (24). The axial resolution in this case is determined by the full

width at half maximum (FWHM) of the normalized signal intensity profile (24) and it

is 8.8 μm, 6.8 μm, and 6.1 μm for the 200, 100, and 50 μm pinholes, respectively. The

axial resolution of the system improves as the size of the pinhole decreases, and an

increasingly larger fraction of out-of-focus light is rejected. However, since the intensity

profiles are recorded in 0.5 μm increments, the resolutions corresponding to the 100 and

50 μm pinholes are not significantly different. It has been shown theoretically (4, 25) and

experimentally (4) that the depth discrimination properties of a confocal microscope do

not improve any further when the normalized pinhole radius is less than approximately

2.5 units. The normalized pinhole radius, v_p, is defined as

$$v_p = \frac{2\pi}{\lambda}\frac{r}{M}NA,$$

where r is the pinhole radius, NA is the objective numerical aperture, λ is the wavelength

of the detected light and M is the magnification of the system from the specimen to the

pinhole. The values of v_p for the three pinholes that we used are included in Table 6.3
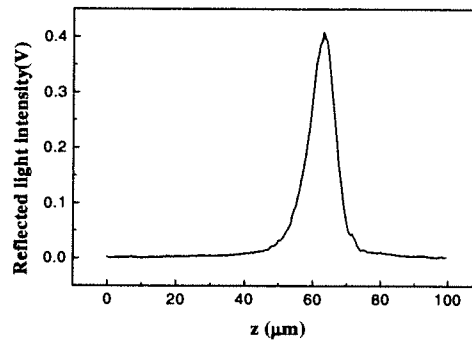
(a)
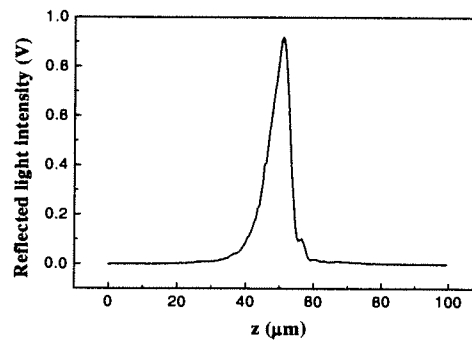
(b)
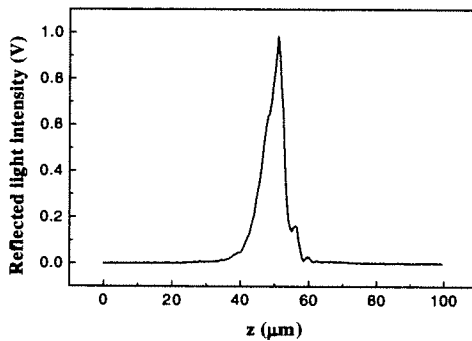
(c)

Figure 6.3: Axial resolution measurements performed in reflectance mode by scanning a mirror through the focal plane with the (a) 200 μm, (b) 100 μm, and (c) 50 μm pinhole in place. The resolution in each case is defined as the full width at half maximum distance, and it is equal to 8.8, 6.8, and 6.1 μm for the 200,100, and 50 μm pinholes, respectively.

Table 6.3: Normalized pinhole radii corresponding to the pinhole diameters that we used

Pinhole diameter	v_p (632 nm)	v_p (680 nm)
200 μm	6.1	5.6
100 μm	3.0	2.8
50 μm	1.5	1.4

for 632 and 680 nm. The normalized pinhole radius corresponding to a 100 μm pinhole

in our set-up is approximately 3. Therefore, it is expected that the axial resolution of the

system will not improve significantly by using a smaller size pinhole.

6.3.2 Axial resolution measurements in fluorescence mode

To determine the axial resolution of the confocal microscope in fluorescence mode we

perform edge response measurements (3, 5). A fluorescence edge was provided by

placing at the microscope stage a Leiden coverslip dish (Medical Systems; described in

detail in chapter 4) filled with a non-scattering Nile Blue A (EtNBA) solution. The

normalized fluorescence intensity profiles that we obtain when we image this

fluorescence edge with a 200, a 100, and a 50 μm pinhole are shown in Figure 6.4. As

in the previous measurements, we start by focusing the objective below the coverslip, so

that we do not excite or detect any fluorescence. As we focus in 1 μm increments closer

to the coverslip surface that is in contact with the EtNBA solution we detect an

increasingly stronger fluorescence signal until the entire focal spot lies within the

fluorescing solution, beyond which the signal reaches a plateau. Two distances have been

reported in the literature as a measure of the axial resolution from edge response

measurements: a) the axial distance over which the signal intensity changes from 20%

to 80% of its maximum (3), and b) the axial distance over which the signal intensity

changes from 10% to 90% of its maximum (5). Both distances are reported in Table 6.2

(a)

(b)

(c)
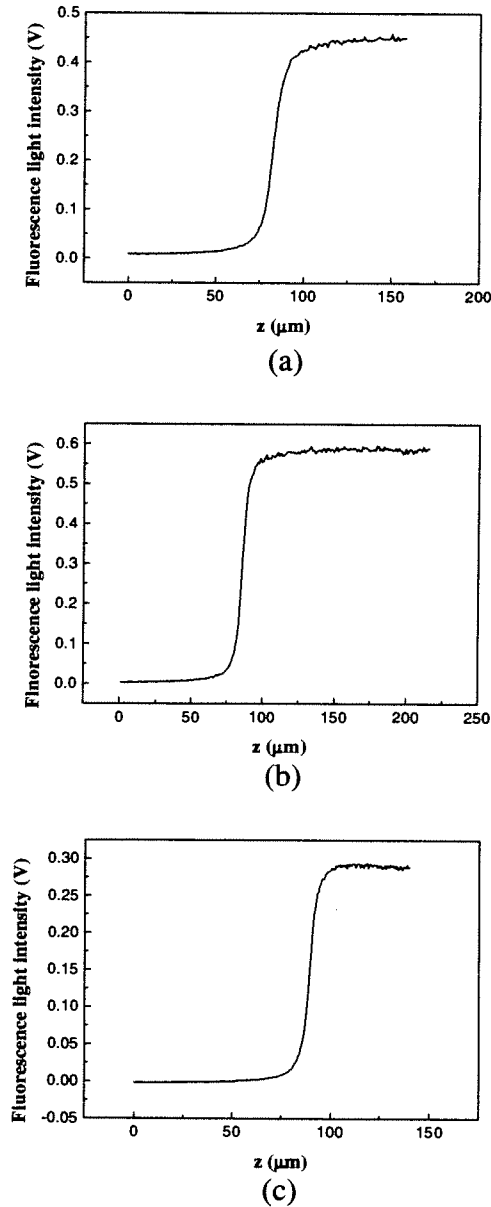
Figure 6.4: Axial resolution measurements performed in fluorescence mode by scanning a fluorescent edge through the focal plane with the (a) 200 μm, (b) 100 μm, and (c) 50 μm pinhole in place. The axial distance over which the signal intensity changes from 10% to 90% of its maximum is 19.5, 14.8, and 11.2 μm for the 200, 100, and 50 μm pinholes, respectively. The axial distance over which the signal intensity changes from 20% to 80% of its maximum is 10.3, 7.2, and 6.2 μm for the 200, 100, and 50 μm pinholes, respectively.

for the three sizes of pinholes that we used. As expected, the axial resolution of the system improves significantly as the pinhole diameter decreases from 200 to 100 μm, while a smaller improvement is observed when comparing the 100 and 50 μm pinholes. Moreover, note that the axial resolution in reflectance is always better than that in fluorescence, in agreement with previous reports (5).

With the current set-up, the axial resolution that we achieve is on the order of a cell diameter. This resolution is adequate to study the progression of sensitizer photobleaching during PDT and any differences in the synthesis of ALA-induced PpIX as a function of oxygenation status within a spheroid. Subcellular resolutions can be achieved with our system by replacing the current objective with an objective of higher NA (diffraction limited axial resolution is inversely proportional to the square of NA) and by using a smaller size pinhole.

6.3.3 Lateral resolution measurements in fluorescence mode

To obtain a measure of the resolution of the confocal microscope in the lateral direction we performed scans at a constant z position of a 44 μm x 46 μm FOV which contained fluorescent carboxylate modified microspheres. The diffraction limited lateral resolution is given by the expression: $d = 1.22 \times \lambda /(2* NA)$, and for a wavelength of 680 nm it is approximately 0.83 μm. Ideally, we should perform our resolution measurements with spheres that are slightly smaller than this resolution limit. Unfortunately, the

commercially available spheres fluorescing around 640-680 nm that are smaller than 0.8

μm in diameter are either too small (PS-Speck microspheres, 0.175 μm diameter,

Molecular Probes, Eugene, OR) or do not absorb light efficiently at 632.8 nm

(Tetraspeck microspheres, 0.5 μm diameter, Molecular Probes), and we were unable to

detect them with the 10X objective. Therefore, we decided to use the 1.0 μm diameter

carboxylate modified fluospheres (Molecular Probes) with maximum fluorescence

excitation and emission wavelengths at 625 and 645 nm, respectively. A small amount

of the initial stock solution of microspheres in distilled water is diluted 200 times in

HBSS and sonicated for about one hour to ensure that the spheres are not aggregated. A

drop of this sonicated solution (approximately 30 μL) is placed on top of a coverslip that

is mounted on a Leiden dish, and the water is allowed to air dry. The spheres that remain

on the coverslip are used to make lateral resolution measurements for our system.

Initially, the fluorescent spheres are visualized by using the Nikon microscope in

conventional fluorescence mode and the appropriate set of filters. Thus, the objective is

focused approximately at the plane of the spheres. Following, the filter set is removed

and the microscope is used in confocal mode. Images of a 44 μm x 46 μm FOV are

obtained at several z positions differing by 1 μm, until the optimal focal plane is found.

Such an image obtained with the 200 μm pinhole in place is depicted in Figure 6.5a.

Images of similar quality and resolution were obtained with the 100 and 50 μm pinholes.

The image consists of 220 pixels in the horizontal (x) direction and 200 pixels in the

vertical (y) direction. The intensity profile in the x and y directions through the middle

(a)

(b)

(c)
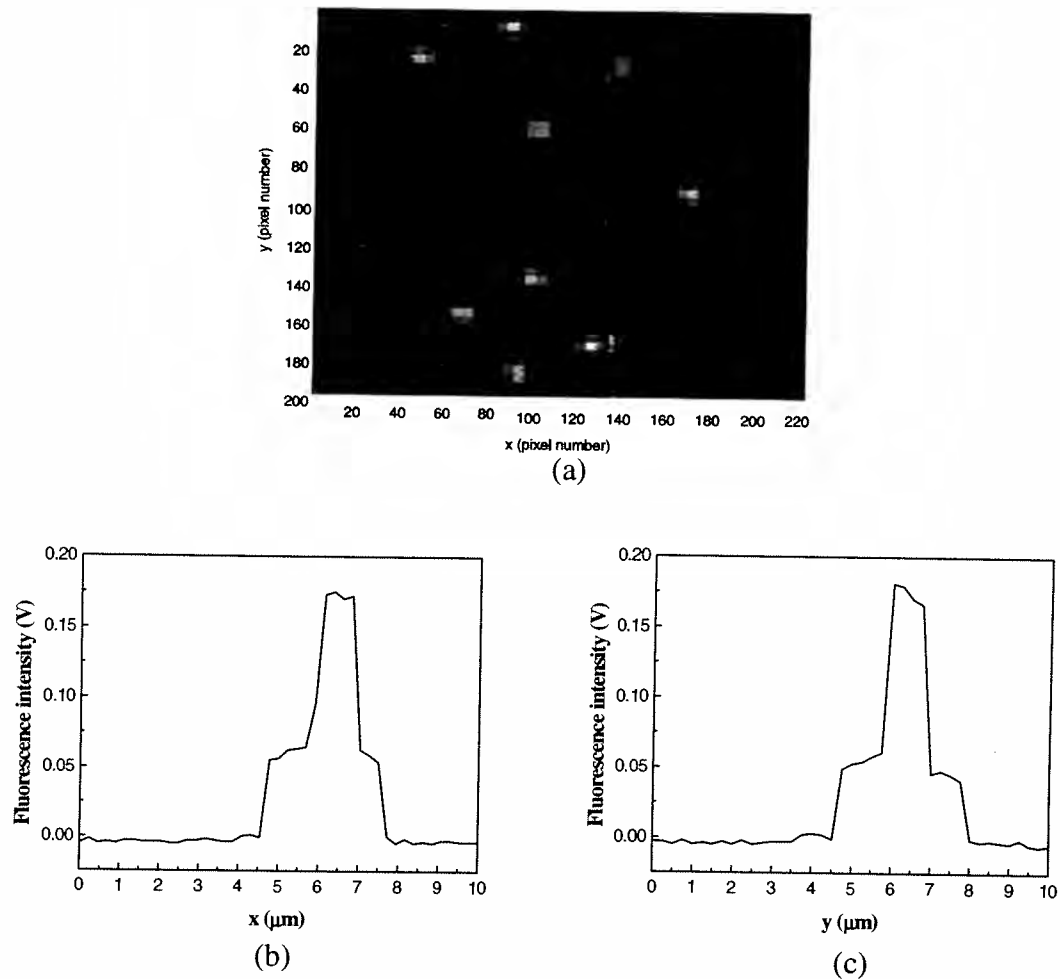
Figure 6.5: Lateral resolution measurements performed by imaging a 44 μm x 46 μm

FOV (220 x 200 pixels) containing 1 μm diameter red fluorescent microspheres. The

image of such a FOV recorded with the 200 μm pinhole in place is shown in panel (a).

The intensity profile in the x and y directions through the middle of one of the spheres

is shown in panels (b) and (c), respectively. The FWHM of these profiles is 1.0 μm (b)

and 1.1 μm (c). The spheres appear square because we are limited by the resolution of

the board used for digital to analog conversion. However, these measurements indicate

that the resolution in the lateral direction is at the most on the order of 1 μm.

of one of the spheres is shown in Figures 6.5b and 6.5c, respectively. The square appearance of the spheres is immediately noticeable. Increasing the resolution of the image does not improve the pixelated appearance of the spheres. We realized that in this case we are limited by the resolution capabilities of the electronic board that we use for digital to analog conversion. Specifically, the board can resolve voltages in the $\pm$ 10 V range with 12-bit accuracy, corresponding to a resolution of 4.88 mV. When a 4.88 mV signal is sent to one of the mirrors, the focal spot moves by approximately 1 μm on the FOV. Therefore, even though each pixel corresponds to a distance of approximately 0.2 μm, the mirror does not move as data is acquired for 4-5 pixels rendering the square appearance to the sphere images. Indeed, note that the FWHM of the intensity profiles in Figues 6.5b and 6.5c are 1.0 and 1.1 μm, respectively. Obviously, to obtain a more accurate estimate of the lateral resolution of the confocal attachment we need a controller board with higher resolution and smaller diameter microspheres. However, these measurements demonstrate that the performance of the system in the lateral direction is approaching the diffraction limit.

6.4   Imaging optical sections through EtNBS-sensitized spheroids

To demonstrate the optical sectioning capabilities of the confocal microscope and the feasibility of sensitizer photobleaching and localization studies during PDT of multicell

tumor spheroids we obtain images of optical sections through EtNBS-sensitized spheroids. The spheroids are incubated for 30 min in the dark with 1.5 μM EtNBS in a 95% air-5% CO_2 atmosphere at 37°C. Following incubation, a spheroid is transferred atop the coverslip of a Leiden dish containing 1 mL of HBSS. The dish is placed at the microscope stage and using minimal illumination the spheroid is centered with respect to the FOV. Three to five images of sections at different depths are obtained until we are able to determine the z position at which we can observe the first spheroid cell layer, *i.e.* the layer closest to the objective. Then, a series of optical sections are taken from the surface to the middle of the spheroid in 5 μm increments. After a set of such images is recorded, we move the stage to its initial position and we repeat the measurement.

Spheroids between 215 and 300 μm in diameter are used for these preliminary studies. The FOV is 350 μm x 350 μm. The intensity of each pixel is the average of ten fluorescence intensity readings obtained at a frequency of 150 KHz. A 200 x 200 pixel image is obtained in approximately 2.7 s. In Figure 6.6, sections through a sensitized spheroid with a diameter of approximately 245 μm are shown at four different depths: a) 0 μm (*i.e.* spheroid layer closest to the coverslip), b) 20 μm, c) 50 μm, and d) 90 μm. These images are obtained with a 100 μm pinhole in place, but very similar images have been recorded with the 200 and 50 μm pinholes. Note that, especially within the images of the shallower layers, we can easily distinguish individual cells and even cell nuclei. A prominent feature of these images is the non-uniform distribution of fluorescence intensity in the sections typically representing cell layers deeper than 40-50 μm within

(a)   (b)

(c)   (d)
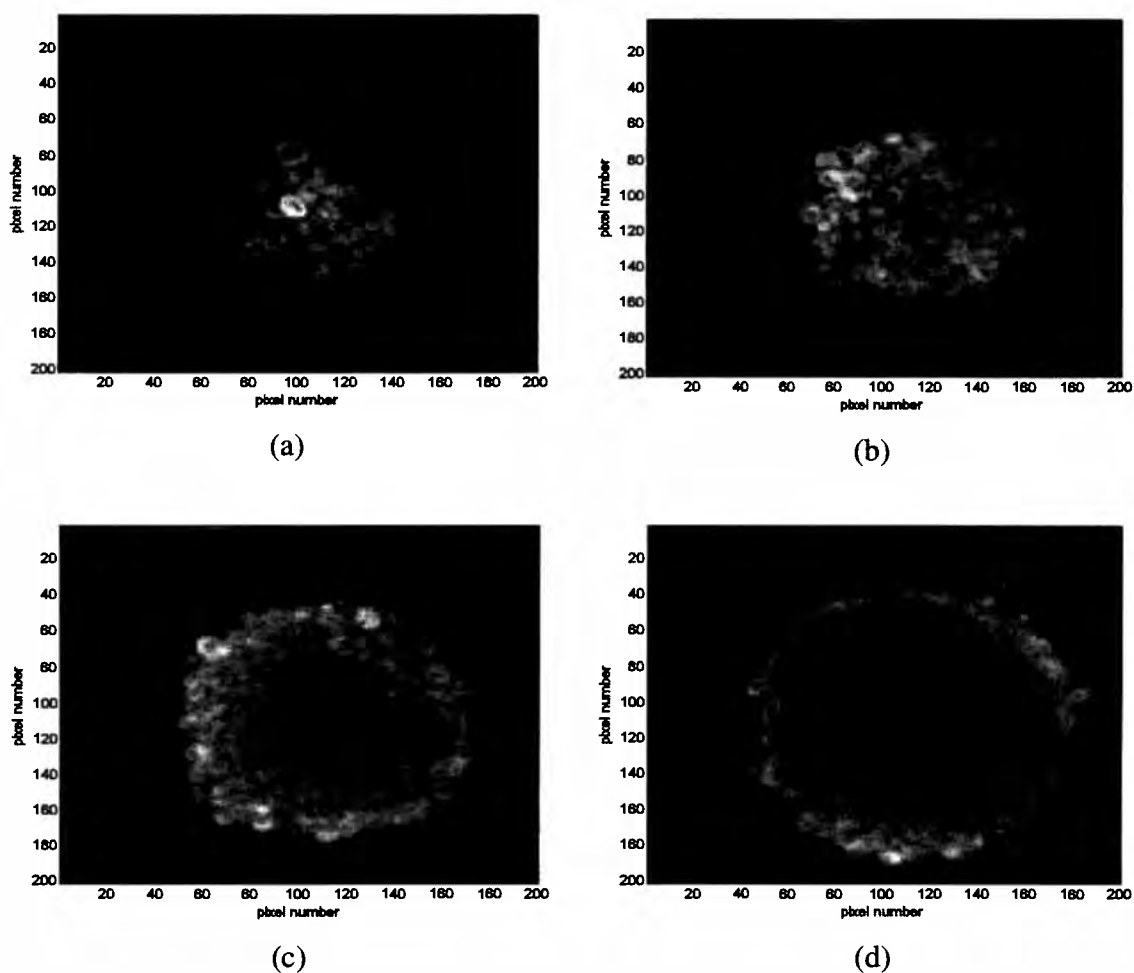
Figure 6.6: Fluorescence confocal images of optical sections at different depths through an EtNBS-sensitized multicell tumor spheroid approximately 245 μm in diameter. In (a) we show an image of the cell layer closest to the objective, while images of cell layers 20, 50, and 90 μm deeper into the spheroid are included in panels (b), (c), and (d), respectively. Individual cell contours are easily distinguishable. However, the fluorescence intensity decreases significantly from the outer cell layers to the center of the spheroid for sections deeper than 40-50 μm within the spheroid.

the spheroid. Specifically, we observe that the fluorescence intensity decreases significantly from the outer cell layers to the center of the spheroid. As we obtain sections closer to the center of the spheroid, fluorescence is detected mainly from the two or three outer cells layers with the inner layers appearing almost completely dark.

However, as shown in Figure 6.7, when the same spheroid is imaged more than once we find that as the fluorescence intensity from the outer layers decreases, probably due to sensitizer photobleaching, some fluorescence at the center of the spheroid becomes visible as a smaller range of intensities corresponds to the 256 levels of the display colormap. These sections are taken at 90 μm from the surface of a spheroid approximately 230 μm in diameter. Cross-sections through the center of these spheroid images (Figure 6.8) demonstrate that the more uniform distributions observed with repeated imaging are indeed due to the decrease in fluorescence of the outer layer, not an increase in fluorescence at the center of the spheroid.

In Figure 6.9 we show a set of images from the fourth set of optical sections of the same spheroid as that shown in Figure 6.7. Figure 6.7d includes the image from the same set obtained at a depth of 90 μm, while Figures 6.9a and 6.9b display the images taken at 120 and 140 μm from the first spheroid cell layer. Some degradation in the quality of the image is observed at 120 μm as compared to that at 90 μm, but individual cells can still be distinguished at the center of the spheroid. Unfortunately, at a depth of 140 μm cell contours cannot be discerned. However, given that the system is not optimized for imaging at the best signal to noise and signal to background ratios, these images are promising.
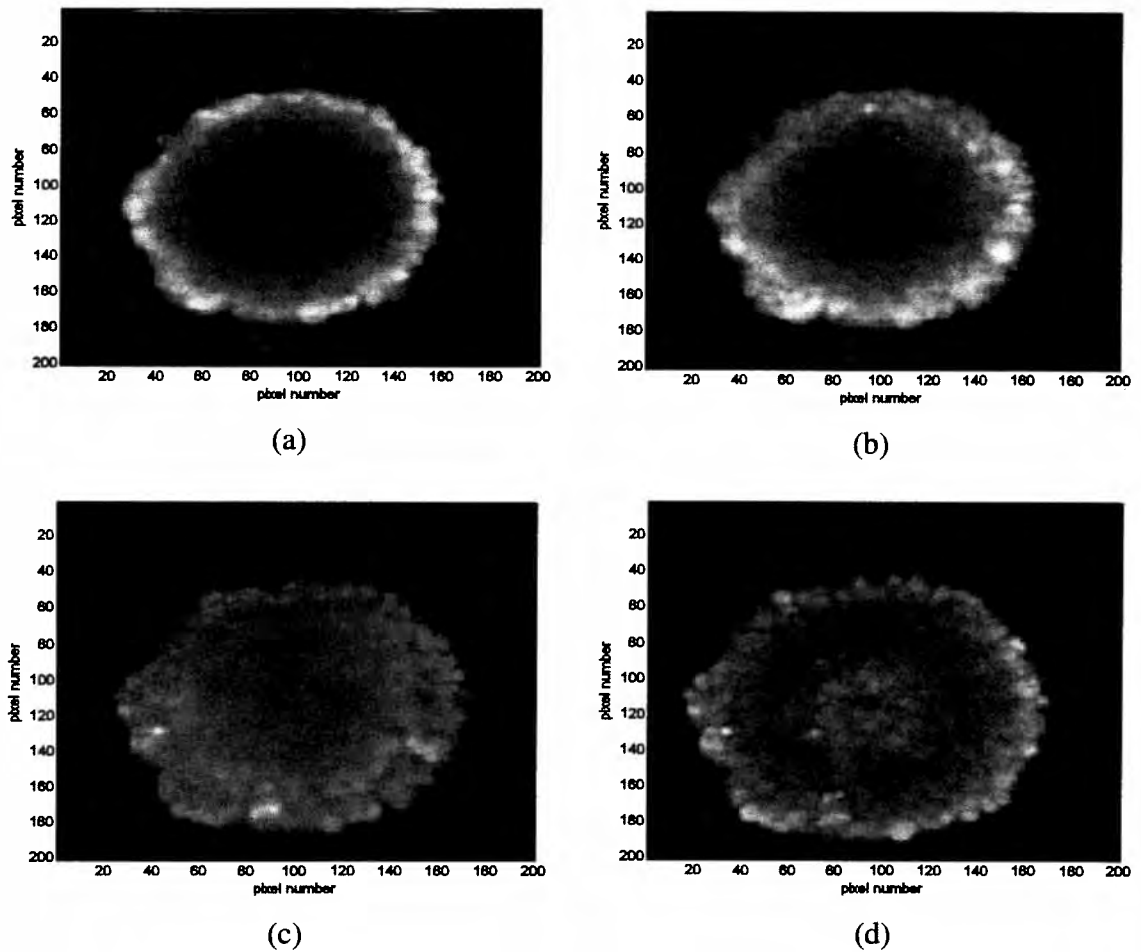
Figure 6.7: Fluorescence confocal images of the same EtNBS-sensitized spheroid section scanned four times consecutively. The spheroid is approximately 230 μm in diameter. The section lies 90 μm within the spheroid. As the fluorescence intensity of the outer spheroid layers decreases with repeated scanning, probably as a result of photobleaching, we can visualize the low intensity fluorescence present in the middle of the spheroid. Note that in panel (d) individual cell contours can be distinguished at the center of the spheroid.
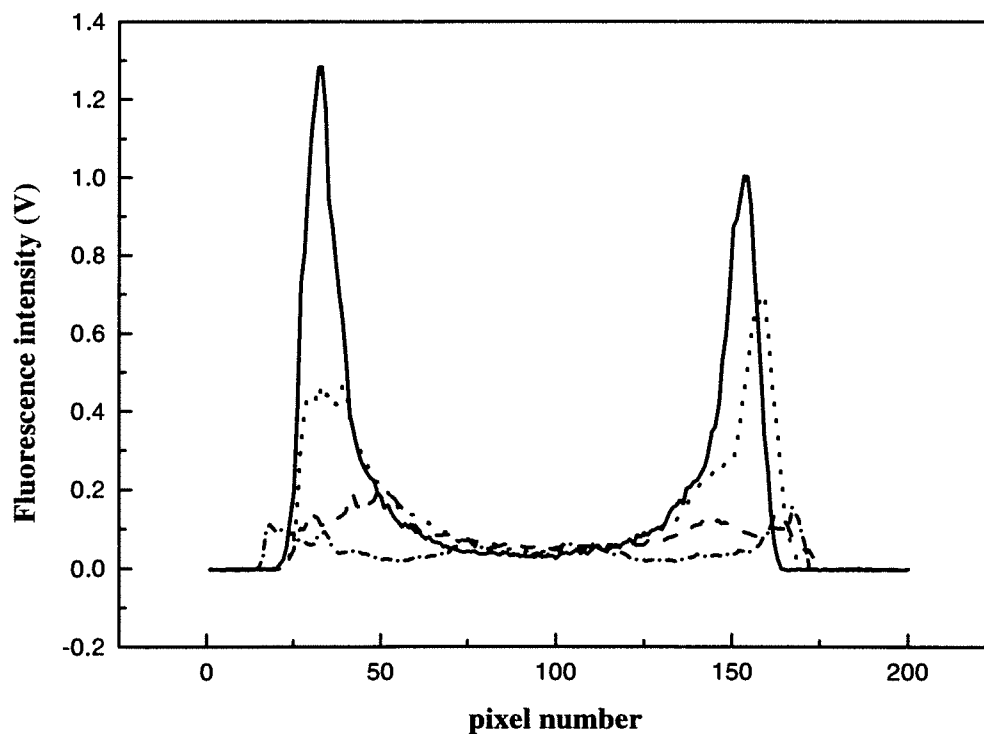
Figure 6.8: Fluorescence intensity cross-sections through the center of the spheroid

images included in Figures 6.7a (————), 6.7b (· · · ·), 6.7c (- - - -), and 6.7d (- · - · -).

The fluorescence intensity of the outer cell layers decreases significantly with repeated

scanning, allowing us to visualize the low intensity fluorescence of the central spheroid

regions.
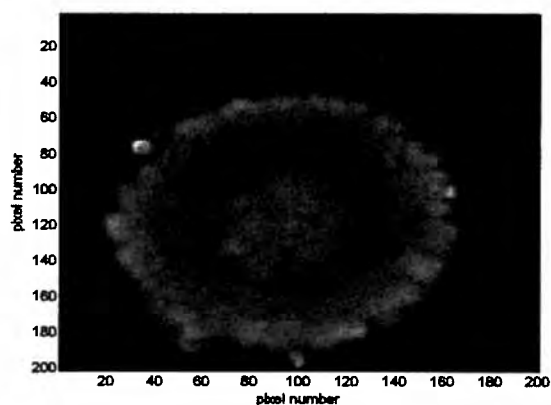
(a)
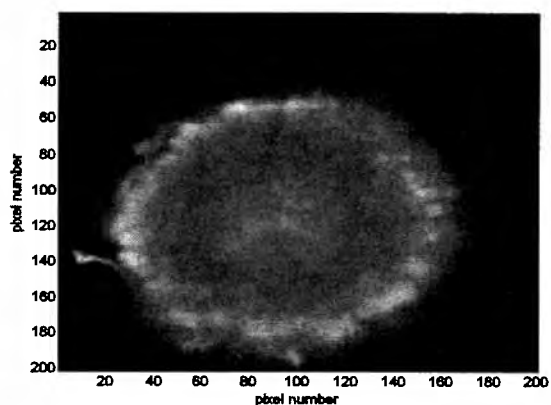
(b)

Figure 6.9: Fluorescence confocal images from the fourth set of optical sections of the same EtNBS-sensitized spheroid as that shown in Figure 6.7. Shown are images of the cell layer residing 120 µm (a) and 140 µm (b) within the spheroid. Comparison of the images obtained at 90 µm (Figure 6.7d), 120 µm, and 140 µm into the spheroid demonstrates that the quality of the recorded signal is degraded with depth. Individual cell contours cannot be discerned at a depth of 140 µm.

6.5   Discussion

In this chapter we describe the design of a laser scanning confocal microscope attachment to an inverted microscope and we demonstrate that it can be used to obtain optical sections through thick specimens such as multicell tumor spheroids. One of the main purposes for building a confocal microscope in our laboratory is the direct observation of sensitizer photobleaching during photodynamic therapy of tumor spheroids. With confocal microscopy we will be able to follow the progression of sensitizer degradation within an individual cell layer through the central section of a spheroid by analyzing the observed changes in detected fluorescence from that layer. As the models for the different photobleaching mechanisms that we have developed predict distinct patterns for the progression of sensitizer degradation within a spheroid during irradiation, our hope is that we will be able to confirm the results that we have obtained indirectly from measurements of dynamic oxygen concentration changes during PDT of sensitized spheroids. For these photobleaching studies resolution on the order of a cell diameter, achievable by the current confocal set up, is desired. Additionally, as spheroids represent an excellent model for the different cell populations and oxygen concentration gradients encountered in real tumors, we should be able to study the dependence of PpIX synthesis on such parameters in a more relevant, dynamic system than monolayer cultures. Once more, resolution at the cellular level is required for such studies.

A beam scanning system was designed, as such a system allows efficient

excitation light transmission and fast scanning while the specimen remains stationary, which is important when images of biological specimens are acquired. However, there are some problems associated with beam scanning. Probably the most serious one is the introduction of aberrations related to the fact that as the beam is scanned, it traverses through peripheral regions of the lenses, not just through the optical axis. Such aberrations include coma, astigmatism, field curvature and distortion. Coma and astigmatism result in the degradation of the focal spot on the specimen, while field curvature and distortion result in a curved field of view about the optical axis and the plane of focus, respectively. An additional problem that we have observed is that the light throughput of the objective is not constant throughout the field of view. Specifically, the amount of light going through the objective decreases gradually as we scan the excitation beam towards the edges of the field of view. This artifact, in combination with the gradual loss of our ability to focus the beam to a tight spot as we move off the optical axis, leads to significant non-uniformities in the detected signal across a uniform field of view. Such non-uniformities have been reported by other investigators as well (26). In our system, we have characterized these artifacts by imaging a plane through a homogeneous EtNBA solution. They can lead to a signal loss of up to 100% at the edges of a 1000 μm x 1000 μm FOV, while for a 350 μm x 350 μm FOV the signal at the edge is typically 5-35% weaker than at the center. The magnitude of this signal loss is dependent on the pinhole size, with smaller pinholes leading to more significant errors. However, this effect is very reproducible and easy to characterize. Therefore, the images can be corrected using a simple algorithm.

The axial resolution measurements reported in Figure 6.5 demonstrate that the combination of the objective and pinhole sizes that we have used so far correspond to resolutions on the order of a cell diameter in a non-scattering medium. Such resolution should be adequate for the studies of sensitizer photobleaching and localization for which this system was designed. Unfortunately, our ability to determine precisely the lateral resolution of the system is limited by the resolution of the electronic board used for digital to analog conversion. However, the measurements that we have made show that this resolution is at most 1 µm and very close to the diffraction limit.

The images of optical sections through EtNBS-sensitized spheroids included in this chapter display the ability of the system to provide information on the cellular level for spheroid cell layers that lie up to approximately 120 µm deeper than the first spheroid cell layer that we can observe. The appearance of a dark center within sections that lie approximately 50 µm from the first observed spheroid layer is mainly due to non-uniform drug distribution. Such non-uniformities have been observed by imaging thin frozen sections of EtNBS-sensitized spheroids with a CCD camera and were described in detail in chapter 3. Light attenuation as a result of scattering and absorption affects the detected fluorescence intensity as well. As expected, the quality of the images of sections that lie deeper within the spheroid degrades. There are two main reasons for this degradation. First, the detected cellular fluorescence intensity decreases as a function of depth into the spheroid because both the excitation and the emitted light are attenuated as they get partially absorbed by fluorophores within cells underneath the focal plane. Secondly,

scattering of the excitation and fluorescence light will result in gradual degradation of the axial resolution of the microscope as its ability to reject out-of-focus light will be compromised. The detected signal levels will be affected by scattering as well since part of the excitation light will be scattered away from the focal plane and some of the fluorescence light will be scattered away from the cone of light collected by the objective.

These effects have been considered by several groups that have attempted imaging sections though thick, highly scattering, biological specimens. Rigaut and Vassy (9) and Rigaut et al. (10) used an empirical equation of log-logistic form to correct for chromomycin A3 bleaching and the attenuation of fluorescence emission intensity with depth in their images of nuclear DNA from normal rat liver and human esophageal tissue sections. This simple correction allowed them to obtain quantitative results on the nuclear DNA content of 1 μm thick optical sections obtained at depths of up to 100 μm from the surface of their tissue blocks. Wartenberg and Acker (22) assumed that the attenuation of the excitation and emitted light due to scattering and absorption within a homogeneously stained tissue can be approximated by a monoexponential decay law if the numerical aperture of the objective is low (0.3 in this case). Attenuation coefficients were determined from calibration experiments for vital and lethal stained tissue. These coefficients were used to correct the fluorescence intensity of stains assaying for cell viability through the center of human malignant glioma cell spheroids up to 700 μm in diameter. The axial resolution of their confocal system was 15 μm. Confocal

fluorescence images of doxorubicin stained prostate cancer spheroids up to 360 μm in diameter were corrected for absorption and scattering as a function of depth into the spheroid using a similar approach (13). An attenuation coefficient was determined by analyzing fluorescence recordings from homogeneously stained densely packed cell pellets. This coefficient along with a calibration intensity were used to correct the mean fluorescence intensity from 600 μm^2 spheroid fields from different depths. It was found that the decrease in fluorescence at increasing depths observed in the confocal images for one of the staining protocols used was an artifact, since a different type of experiment demonstrated that the drug stained the spheroid cells homogeneously. When the data was corrected for the effects of light scattering and absorption, this artifact was eliminated.

Some more rigorous, but time and CPU-intensive algorithms that account for the effects of light attenuation by scattering and absorption have been reported. These techniques are based on section by section processing, using the information from the layer processed last to update the extinction information and correct the next image section. It is assumed that the scattering and absorption are governed by an exponential decay law, as previously. The extinction coefficient of the first layer is considered to be proportional to its fluorescence intensity, an assumption that is valid for small extinction coefficients. Further, the extinction coefficient within each layer is assumed to be uniform in the z direction. Visser *et al.* (27) use a model in discrete space to describe light attenuation. Their algorithm provides accurate restorations of images through scattering media, but it is very time and CPU consuming. Roerdink and Bakker (28)

formulate the problem in continuous three-dimensional space and develop a fast fourrier transform (FFT)-based solution which is much more efficient but not as accurate as the layer stripping method of Visser et al.(27). However, the quality of the two approaches becomes comparable at deeper layers. The continuous model of Roerdink and Bakker (28) is further simplified by Strasters et al.(29), requiring two dimensional, as opposed to three dimensional, convolutions and decreasing even further the complexity and time inefficiency of the algorithm. Their approach is based on the observation that a large fraction of the light cone focused on the layer of interest has been traced already during the processing of the previous layer. Further assumptions need to be made to justify the simplifications, and the accuracy of the algorithm is slightly worse than that of Roerdink and Bakker (28). However, depending on the application, the inferior performance of the latter algorithms could be acceptable, given that the processing time for a particular three-dimensional specimen can decrease from several hours for the Visser algorithm (27) to a few seconds for the Strasters algorithm (29).

Calculations and measurements of the penetration depth limits of confocal microscopy in highly scattering media such as tissue have been presented. Schmitt et al. (30) have developed a model that combines Monte Carlo simulations of light transport in a highly scattering medium with ray tracing through the optics of a reflectance confocal microscope. The predictions of the model with respect to the effects of scattering on the axial resolution of a confocal microscope are typically in good agreement with experimental results. It is pointed out that the ability of the pinhole to

reject light scattered outside the focal zone is compromised at increasing optical depths by multiply scattered light (optical depth = number of mean free paths over which photons scatter in the medium to reach depth z). Moreover, it is shown that even though the signal intensity increases with an increasing pinhole size, most of the additional signal consists of scattered light from the regions close to the surface of the specimen. Therefore, depth discrimination is achieved at the expense of light loss, and a trade-off exists between background rejection and detected signal levels. From such trade-off considerations it is estimated that a reflectance confocal microscope can probe a tissue with a typical scattering anisotropy and coefficient to a depth of approximately 300-400 µm. Importance sampling can be applied to Monte Carlo simulations of reflectance confocal microscopy to increase the efficiency of such calculations (31). Such a model is used to demonstrate the superior ability of smaller size pinholes to reject multiply scattered light. From considerations of background rejection and signal detection the authors arrive at the conclusion that depths on the order of 200-300 µm can be probed with a reflectance confocal microscope. Trade-offs between signal-to-background and signal-to-noise ratios are considered by Smithpeter *et al.* (32) to determine the depth limits of confocal reflectance imaging in tissue like specimens. The experimental results presented in this paper with respect to background rejection and signal detection for different pinhole sizes are in agreement with the previous studies mentioned. The authors conclude that the signal-to-noise ratio limits the penetration depth of a confocal microscope either when the scattering coefficient or the effective pinhole size is small,

while the signal-to-background ratio plays a determining role when either the scattering coefficient or the effective pinhole size is large.

Unfortunately, detailed studies of the effects of scattering on the resolution and the depth probing limitations have not been reported for fluorescence confocal microscopy. In fact, such studies are being conducted in our laboratory currently. We hope that such studies will help us determine the optimal effective pinhole size for imaging optical sections through multicell tumor spheroids. Such measurements, along with application of algorithms to correct for the effects of light attenuation with depth, should allow us to obtain images with improved resolution at increased depths from the spheroid surface than the images presented in this chapter. Nevertheless, we have demonstrated that even without such optimizations, the confocal microscope that we built is capable of achieving the axial resolution required to study directly sensitizer photobleaching and localization with sensitized spheroids approximately 240 μm in diameter.

References

1.	White, J.G. and W.B. Amos (1987) Confocal microscopy comes of age. *Nature* **328**, 183-184.

2.	Wilson, T. and A.R. Carlini (1987) Depth discrimination criteria in confocal optical systems. *Optik* **76**, 164-166.

3. Wijnaendts van Resandt, R.W., H.J.B. Marsman, R. Kaplan, J. Davoust, E.H.K. Stelzer and R. Stricker (1984) Optical fluorescence microscopy in three dimensions: microtomoscopy. *J. Microscopy* **138**, 29-34.

4. Pawley, J. (1989) *The handbook of biological confocal microscopy.* IMR Press, Madison, WI.

5. Wilson, T. (1990) *Confocal microscopy.* Academic Press Inc., San Diego, CA.

6. Fine, A., W.B. Amos, R.M. Durbin and P.A. McNaughton (1988) Confocal microscopy: applications in neurobiology. *TINS* **11**, 346-351.

7. Turner, J.N., D.H. Szarowski, K.L. Smith, M. Marko, A. Leith and J.W. Swann (1991) Confocal microscopy and three-dimensional reconstruction of electrophysiologically identified neurons in thick brain slices. *J. Electron Microsc. Tech.* **18**, 11-23.

8. Nygaard, S.J.T. and O.-B. Tysnes (1996) Quantification of glioma cell invasion by confocal laser scanning microscopy in an in vitro co-culture system. *Cancer Lett.* **105**, 45-49.

9. Rigaut, J.P. and J. Vassy (1991) High-resolution three-dimensional images from confocal scanning laser microscopy. *Anal. Quant. Cyt. Hist.* **13**, 223-232.

10. Rigaut, J.P., J. Vassy, P. Herlin, F. Duigou, E. Masson, D. Briane, J. Foucrier, S. Carvajal-Gonzalez, A. Downs and A.-M. Mandard (1991) Three-dimensional DNA image cytometry by confocal scanning laser microscopy in thick tissue blocks. *Cytometry* **12**, 511-524.

11. Hjelstuen, M.H., K. Rasch-Halvorsen, C. Brekken, Ø. Bruland and C. de L. Davies (1996) Penetration and binding of monoclonal antibody in human osteosarcoma multicell spheroids. *Acta Oncol.* **35**, 273-279.

12. Porwol, T., E. Merten, N. Opitz and H. Acker (1996) Three-dimensional imaging of rhodamine 123 fluorescence distribution in human melanoma cells by means of confocal laser scanning microscopy. *Acta Anat.* **157**, 116-125.

13. Wartenberg, M., J. Hescheler, H. Acker, H. Diedershagen and H. Sauer (1998) Doxorubicin distribution in multicellular prostate cancer spheroids evaluated by confocal laser scanning microscopy and the "optical probe technique". *Cytometry* **31**, 137-145.

14. Villringer, A., R.L. Haberl, U. Dirnagl, F. Anneser, M. Verst and K.M. Einhäupl (1989) Confocal laser microscopy to study microcirculation of the rat brain surface *in vivo. Brain Res.* **504**, 159-160.

15. Dirnagl, U., A. Villringer and K.M. Einhäupl (1991) *In-vivo* confocal scanning laser microscopy of the cerebral microcirculation. *J. Microscopy* **165**, 147-157.

16. Villringer, A., A. Them, U. Lindauer, K. Einhäupl and U. Dirnagl (1994) Capillary perfusion of the rat brain cortex. An *in vivo* confocal microscopy study. *Circ. Res.* **75**, 55-62.

17. Merchant, F.A., S.J. Aggarwal, K.R. Diller and A.C. Bovik (1994) *In-vivo* analysis of angiogenesis and revascularization of transplanted pancreatic islets

using confocal microscopy. *J. Microscopy* **176**, 262-275.

18.   Corcuff, P., C. Bertrand and J.L. Leveque (1993) Morphometry of human epidermis *in vivo* by real-time confocal microscopy. *Arch. Dermatol. Res.* **285**, 475-481.

19.   Piérard, G.E. (1993) *In vivo* confocal microscopy: a new paradigm in dermatology. *Dermatol.* **186**, 4-5.

20.   Rajadhyaksha, M., M. Grossman, D. Esterowitz, H. Webb and R.R. Anderson (1995) *In vivo* confocal scanning laser microscopy of human skin: melanin provides strong contrast. *J. Invest. Dermatol.* **104**, 946-952.

21.   Møller-Pedersen, T., M. Vogel, H.F. Li, W.M. Petroll, H.D. Cavanagh and J.V. Vester (1997) Quantification of stromal thinning, epithelial thickness, and corneal haze after photorefractive keratectomy using *in vivo* confocal microscopy. *Opthalmology* **104**, 360-368.

22.   Wartenberg, M. and H. Acker (1995) Quantitative recording of vitality patterns in living multicellular spheroids by confocal microscopy. *Micron* **26**, 395-404.

23.   Pelsue, K. (1983) Precision, post-objective, two-axis, galvanometer scanning. *Proceed. SPIE* **390**, 70-78.

24.   Wilson, T. and A.R. Carlini (1988) Three-dimensional imaging in confocal imaging systems with finite sized detectors. *J. Microscopy* **149**, 51-66.

25.   Wilson, T. and A.R. Carlini (1987) Size of the detector in confocal imaging

systems. *Opt. Letters* **4**, 227-229.

26.   Oldmixon, E.H. and K. Carlsson (1993) Methods for large data volumes from confocal scanning laser microscopy of lung. *J. Microscopy* **170**, 221-228.

27.   Visser, T.D., F.C.A. Groen and G.J. Brakenhoff (1991) Absorption and scattering correction in fluorescence confocal microscopy. *J. Microscopy* **163**, 189-200.

28.   Roerdink, J.B.T.M. and M. Bakker (1993) An FFT-based method for attenuation correction in fluorescence confocal microscopy. *J. Microscopy* **169**, 3-14.

29.   Strasters, K.C., H.T.M. van der Voort, J.M. Geusebroek and A.W.M. Smeulders (1994) Fast attenuation correction in fluorescence confocal imaging: a recursive approach. *Bioimaging* **2**, 78-92.

30.   Schmitt, J.M., A. Knüttel and M. Yadlowsky (1994) Confocal microscopy in turbid media. *J. Opt. Soc. Am. A* **11**, 2226-2235.

31.   Schmitt, J.M. and K. Ben-Letaief (1996) Efficient Monte Carlo simulation of confocal microscopy in biological tissue. *J. Opt. Soc. Am. A* **13**, 952-961.

32.   Smithpeter, C.L., A.K. Dunn, A.J. Welch and R. Richards-Kortum (1998) Penetration depth limits of *in vivo* confocal reflectance imaging. *Appl. Optics* **37**, 2749-2754.

Chapter 7

Conclusions and future directions

7.1 Sensitizer photobleaching and photodynamic dosimetry

A main focus of this thesis has been the study of the mechanisms of photosensitizer degradation and their effects on photodynamic $^3O_2$ consumption and $^1O_2$ deposition. We developed expressions based on two non-$^1O_2$-mediated photobleaching mechanisms which, along with the previously derived $^1O_2$-mediated sensitizer degradation model, represent a reasonable set of possible schemes to consider when designing a photodynamic dosimetry protocol. Our expressions were incorporated in a model of oxygen diffusion with consumption used to describe the kinetics of photodynamic $^3O_2$ consumption during irradiation of sensitized multicell tumor spheroids. The avascular tumor spheroid provided an excellent model for performing quantitative $^3O_2$ concentration

measurements and observing the effects of sensitizer photobleaching on $^3O_2$ consumption during PDT.

We were able to determine whether a particular sensitizer is degraded *via* a $^1O_2$- or a non-$^1O_2$-mediated mechanism by using a model of oxygen diffusion with consumption that incorporated the effects of these different photobleaching schemes to analyze $^3O_2$ concentration measurements obtained during irradiation of Photofrin®-, ALA-induced PpIX-, EtNBS- and EtNBSe-sensitized spheroids. We found that while the time-dependent $^3O_2$ concentration distributions recorded at the edge of Photofrin®- and PpIX-sensitized spheroids were consistent with $^1O_2$-mediated photobleaching, those obtained during irradiation of EtNBS- and EtNBSe-sensitized spheroids were in agreement with non-$^1O_2$-mediated sensitizer degradation. Based on the analysis of these $^3O_2$ concentration measurements we presented simulations of net photochemical $^3O_2$ consumption within sensitized spheroids to show the significant ways in which sensitizer degradation affects $^1O_2$ deposition, and, thus, the outcome of a particular therapeutic protocol. Such simulations demonstrated also the importance of distinguishing between $^1O_2$- and non-$^1O_2$-mediated photobleaching, since they resulted in very different patterns of $^1O_2$ deposition within a multicellular system like a spheroid.

Finally, we found that the empirically-derived fluence dependent simple exponential decay description of sensitizer degradation is not consistent with any of the photobleaching mechanisms that we considered. Nevertheless, we should mention that, recently, an expression has been derived for the photobleaching mechanism involving the

excited sensitizer singlets that is consistent with a fluence dependent simple exponential decay model (Michael S. Patterson, personal communication). Therefore, this is an issue that should be investigated further.

While the indirect observations of sensitizer photobleaching *via* the $^3O_2$ microelectrode measurements have allowed us to draw some very important conclusions concerning the effects of sensitizer degradation on photodynamic dosimetry, the next step is the direct observation of these processes. For this purpose, we built a laser beam scanning confocal attachment to an inverted microscope, since conventional microscopy does not provide adequate rejection of background signal for imaging through thick biological specimens such as spheroids. We demonstrated that the axial resolution of this confocal system in a non-scattering medium is on the order of a cell diameter when operating in fluorescence mode with a 100 μm or smaller pinhole in place. Moreover, we presented some preliminary images with a resolution on the cellular level through the center of EtNBS-sensitized spheroids, approximately 240 μm in diameter.

Once the system is optimized to achieve the best signal-to-background and signal-to-noise ratios, we expect that we should be able to image through the center of bigger diameter spheroids. Additionally, corrections for the effects of light attenuation as a result of scattering and absorption events will have to be implemented for quantitative interpretation of these images. Since analysis of the time-dependent $^3O_2$ concentration distributions indicated that EtNBS photobleaches *via* a non-$^1O_2$-mediated mechanism, we expect that the fluorescence intensity of a section through an EtNBS-sensitized spheroid
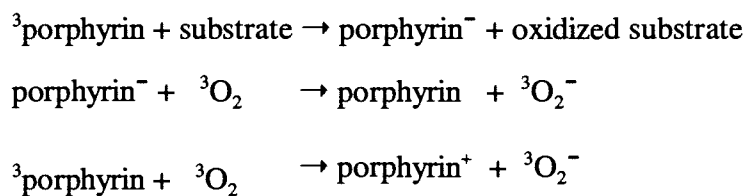
will decrease either uniformly throughout the spheroid if the excited singlets are involved or in a slightly non-uniform manner with more photobleaching occurring at the center of the spheroid than at the outer rim if the excited triplets are involved. Of course, these predictions assume that the sensitizer is uniformly distributed throughout the spheroid. This is not the case for the sensitizer incubation protocol that we have used for the studies presented in this thesis. It will probably be very useful to investigate whether a more uniform EtNBS distribution can be achieved by modifying the current protocol. For example, incubating the spheroid with a lower drug concentration but for a longer time period might result in more uniform uptake by the spheroid cells.

Simply by changing the dichroic filter and using a different laser (the 514 nm line of an argon ion laser) we should be able to obtain images through Photofrin®-sensitized spheroids. Imaging Photofrin® fluorescence will probably be more challenging than imaging EtNBS fluorescence, since Photofrin® has a rather low fluorescence yield. Therefore, the pinhole size might have to be modified to optimize the signal-to-background and signal-to-noise ratios in this case as well. As our $^3O_2$ concentration measurements indicate that Photofrin® photobleaches *via* a $^1O_2$-mediated mechanism, we expect the front of fluorescence photobleaching to progress from the outer, $^3O_2$-rich spheroid regions to the central, hypoxic core.

Improvements in the design of the confocal attachment could make transitions for imaging with different sensitizers much easier. For example, instead of aligning the confocal optics with respect to the beam from a specific a laser, we could perform the

alignment with respect to the light emanating from a single mode fiber. The other end of the fiber could be aligned with any number of lasers that we might use as excitation sources. Thus, switching from one excitation source to the other would not require realignment of the entire confocal system. Furthermore, the quality of a beam from a single mode fiber is much better than that of a beam directly out of a laser. We could use a spatial filter to improve the uniformity of the beam from the HeNe laser, for example, but that would not be necessary if we used a single mode fiber.

From a theoretical perspective, it might be necessary to consider more complicated photobleaching schemes than the ones that we have described already. For example, we could consider an $^3O_2$-dependent non-$^1O_2$-mediated mechanism. Specifically, it is known that the excited triplets of certain porphyrins can participate in the following processes (1):

$$^3\text{porphyrin} + \text{substrate} \rightarrow \text{porphyrin}^- + \text{oxidized substrate}$$

$$\text{porphyrin}^- + \ ^3O_2 \quad \rightarrow \text{porphyrin} \ + \ ^3O_2^-$$

$$^3\text{porphyrin} + \ ^3O_2 \quad \rightarrow \text{porphyrin}^+ + \ ^3O_2^-$$

It would be interesting to describe the progression of such photobleaching mechanisms in an oxygen limited environment and determine any differences or similarities with the schemes that we have considered already.

Ultimately, our aim is to extend the models and the experimental results that we have obtained with sensitized spheroids to the *in vivo* situation. The model of oxygen diffusion with consumption, now developed to correspond to the spherical symmetry of

the spheroid, would have to be modified to represent the tumor geometry. To a first approximation, we could probably model the tumor capillaries as Krogh cylinders and recast the oxygen diffusion with consumption problem into cylindrical coordinates. Moreover, unless we are considering very small tumors (the size of a spheroid, for example), we should take into account the attenuation of the excitation and the fluorescence light with depth from the surface of a tumor as a result of the absorption and scattering properties of tissue. Having a solid understanding of the possible sensitizer degradation mechanisms that could be involved we could draw conclusions on whether sensitizer photobleaching can be used as a "dose metric", *i.e.* an indicator of the photodynamically induced damage for a particular protocol. If the agent resulting in sensitizer degradation and cell death is the same, as in the case of $^1O_2$-mediated photobleaching, associations between the progression of photobleaching and the deposition of the cytotoxic agent could be possible. However, if the sensitizer is degraded *via* a non-$^1O_2$-mediated mechanism it will probably be rather difficult to employ sensitizer photobleaching as a measure of the deposited photodynamic dose.

7.2   Sensitizer localization and photodynamic dosimetry

A second area of focus of this thesis has been the relationship between sensitizer localization and photodynamic $^3O_2$ consumption. We showed that during irradiation of EtNBS- and EtNBSe-sensitized spheroids $^3O_2$ consumption occurred in two well-defined

phases. The onset of the second phase was a fluence dependent event, but it required eight times fewer photons for EtNBSe than for EtNBS. We presented the results of fluorescence microscopy studies performed with EtNBS-sensitized monolayer cultures indicating that during irradiation EtNBS redistributed from the lysosomes, where it localized mainly initially, to the cytosol. The fluence resulting in this relocalization event coincided with the fluence at which the onset of the second $^3O_2$ consumption phase was observed during irradiation of EtNBS-sensitized spheroids. Studies of sensitizer uptake by spheroid cells and cells in monolayer culture were in agreement with the hypothesis that the second $^3O_2$ consumption phase is the result of sensitizer redistribution. If this association is valid, then the observed enhancement in $^3O_2$ consumption indicates that the efficiency of the sensitizer as a photodynamic agent is increased once it relocalizes into the cytosol, possibly because it becomes less aggregated.

The association between the onset of the second $^3O_2$ consumption phase and sensitizer redistribution could be strengthened by performing $^3O_2$ concentration measurements with spheroids that contain EtNBS uniformly throughout their volume. In that case, we would also be able to draw some conclusions concerning the importance of sensitizer redistribution in terms of cytotoxicity. Specifically, since we know the threshold dose of $^1O_2$ for EtNBSe-sensitized spheroids, we could estimate whether a cytotoxic concentration of $^1O_2$ is deposited throughout the spheroid at the time of relocalization. These estimates could serve as an indicator of the consequences of lysosomal damage for cell viability.

Simultaneous measurements of $^3O_2$ consumption and sensitizer localization would provide direct evidence for the correlation of these two events. By using a higher numerical aperture objective and a smaller pinhole aperture, we should achieve subcellular axial resolution with the confocal microscope that we have built. Therefore, we should be able to observe simultaneously the patterns of sensitizer localization and the changes in $^3O_2$ concentration recorded by an $^3O_2$ electrode during irradiation of an EtNBS-sensitized spheroid. In fact, we have already purchased a stage adapter and a prism that will allow us to mount the $^3O_2$ microelectrode on the microscope stage and control its positioning with respect to a spheroid.

Non-uniformities in the localization of sensitizer on the tumor level have been considered indirectly for ALA-induced PpIX. Specifically, we studied the relationship between PpIX synthesis and the presence of hypoxia for three different cell populations in monolayer cultures: a) low density exponential cells, b) high density fed-plateau cells, and c) high density unfed-plateau cells. PpIX synthesis was assayed by fluorescence spectroscopy. We found that hypoxia significantly reduced PpIX synthesis in EMT6 monolayer cultures. The magnitude of this effect was dependent on the cell density and proliferation status of the cell population. The high density unfed-plateau population experienced the highest decrease (42-fold) in PpIX synthesis in the presence of hypoxia, while the low density exponential cells were affected the least (1.4-fold decrease) and the high density fed plateau population had an intermediate response (20-fold decrease). Since the high density unfed plateau cells were selected to represent the tumor populations

further away from capillaries that have limited access to oxygen and nutrients, this study indicated that the ability of such tumor populations to synthesize PpIX could be impaired. Therefore, for PpIX-PDT our ability to produce $^1O_2$ in hypoxic tumor areas could be hindered not only by the limited availability of $^3O_2$ but also by decreased concentrations of photosensitizer. This combination of problems could significantly affect the efficacy of the therapy.

Multicell tumor spheroids provide a good model system for the study of this problem in a more dynamic environment, since the outer, highly proliferating spheroid cell layers are similar to tumor populations surrounding a capillary, while the central, more quiescent populations are equivalent to cells in tumor regions further away from capillaries. Variations in the amount of PpIX synthesized across different spheroid regions could be detected *via* confocal fluorescence microscopy. Resolution on the cellular level would be required for such studies. A range of spheroid sizes could be used to investigate the effects of different oxygen gradients on PpIX synthesis. The minimum $^3O_2$ concentration at the center of the spheroid could be manipulated by adjusting the $^3O_2$ tension in the medium surrounding the spheroid. Perfusion systems that could achieve such control are available commercially for use with coverslip dishes such as the ones that we use already to perform our confocal experiments.

7.3 Concluding remarks

In conclusion, we have shown that sensitizer photobleaching and localization can affect in very significant ways photodynamic $^3O_2$ consumption and dosimetry. We have demonstrated the importance of considering the details and mechanisms associated with these processes when designing efficient photodynamic treatment protocols. While the measurements of photodynamically induced $^3O_2$ concentration changes in sensitized multicell tumor spheroids have allowed us to observe indirectly the events associated with sensitizer photobleaching and relocalization, we are confident that our results will be confirmed by direct observation of these phenomena using fluorescence confocal microscopy. Finally, we hope that this work will provide the basis for expanding our models and experiments to describe sensitizer photobleaching and localization during photodynamic therapy *in vivo*.

References

1.   Foote, C.S. (1984) Mechanisms of photooxygenation. In Porphyrin Localization and Treatment of Tumors. *Prog. Clin. Biol Res.* **170**, 3-18.

Appendix A

Derivation of the Oxygen Consumption-Dependent Variation of the Depletion Zone Radius

The radius of the depletion zone, R_d, is the radial distance from the center of the spheroid at which the oxygen concentration is equal to that of the bulk medium. This distance is finite because the spheroid is placed in an open dish and, consequently, convection currents exist in the medium. Near the spheroid, the oxygen flux is dominated by diffusion towards the spheroid, where oxygen is consumed by metabolic and, during PDT, by

photochemical processes. This diffusive flux is proportional to $1/r^2$, where r is the distance from the center of the spheroid. The balance between the convective and diffusive fluxes establishes the depletion radius.

The rate of oxygen consumption in the spheroid, $\Gamma(r,t)$, determines the diffusive flux into the depletion zone, $\vec{J}(r,t)$. Fick's laws dictate that the diffusive flux and the change in oxygen concentration are given by

$$\vec{J}(r,t) = -D_d \vec{\nabla}[^3O_2](r,t) \tag{A1}$$

and

$$-\vec{\nabla} \cdot \vec{J}(r,t) = \frac{\partial [^3O_2](r,t)}{\partial t} + \Gamma(r,t), \tag{A2}$$

respectively. A volume integral over all space of Eq. A2 and the use of Gauss's theorem lead to the following expression for the time-dependent radial diffusive flux at the depletion radius as a function of the average oxygen consumption rate per unit volume in the spheroid at time t, $\bar{\Gamma}(t)$:

$$\vec{J}(R_d,t) = -\frac{\bar{\Gamma}(t)R_s^3}{3R_d^2}\hat{r}, \tag{A3}$$

where R_s is the spheroid radius, and $\hat{r}$ is the outwardly directed radial unit vector. The volume integral of the change in oxygen concentration with time is zero, since there is no bulk depletion of oxygen in the medium under our experimental conditions. During PDT the rate of oxygen consumption in the spheroid increases. Consequently, the magnitude of the diffusive flux will increase proportionately, and a new balance between diffusive and convective flux will be achieved further away from the spheroid.

To incorporate a dynamic depletion zone boundary, it is necessary to derive an

expression for the depletion radius as a function of $\bar{\Gamma}(t)$. Thus, in the numerical algorithm

used to solve Eqs. 2.1 and 2.2, we wish to calculate the value of the depletion radius at

each time-step, t, as a function of the spatially averaged oxygen consumption rate of the

previous time-step, t-Δt. First, we note that the flux entering the boundary is altered as a

result of convection in the following way:

$$\vec{J}(R_d,t) = -D_d\vec{\nabla}[^3O_2](R_d,t) - \vec{\upsilon}[^3O_2]_{R_d} \tag{A4}$$

where $\vec{\upsilon}$ is the rate of change of the depletion radius, and $[^3O_2]_{R_d}$ is the oxygen

concentration at the depletion radius, and, thus, throughout the air-saturated medium.

Then, combining Eqs. A3 and A4 we obtain

$$\left(-D_d\frac{\partial[^3O_2](R_d,t)}{\partial r} - \frac{dR_d}{dt}[^3O_2]_{R_d} \right) R_d^2 = -\frac{1}{3}\bar{\Gamma}(t)R_s^3. \tag{A5}$$

We descretize the velocity,

$$\upsilon = \frac{dR_d}{dt} = \frac{R_d(t)-R_d(t-\Delta t)}{\Delta t}, \tag{A6}$$

and the oxygen gradient at the depletion radius to obtain a cubic equation with respect to

R_d:

$$R_d^3(t) - \left(-D_d\frac{[^3O_2](R_d,t) - [^3O_2](R_d - \Delta r,t)}{\Delta r} + \frac{R_d(t-\Delta t)}{\Delta t}[^3O_2]_{R_d} \right) \frac{\Delta t}{[^3O_2]_{R_d}}R_d^2(t) -$$

$$\frac{\bar{\Gamma}(t)R_s^3\Delta t}{3[^3O_2]_{R_d}} = 0. \tag{A7}$$

This equation has only one root and can be solved using standard techniques. Using the

solution of Eq. A7 we calculate the radius of the depletion zone numerically at every time

point t.

By allowing the depletion zone radius to vary with time, we change the boundary

condition at that radial position. Specifically, we have a moving boundary and the flux at

this boundary is given by Eq. A4. Change in the depletion zone radius implies change in

the spacing of the radial grid of the model, since the total number of radial steps remains

the same. To make the incorporation of this variation into the model easier, we change

the radial increments outside the spheroid only.

In the region between the edge of the spheroid and the depletion zone radius the

diffusion equation is still:

$$\frac{\partial [^3O_2](r,t)}{\partial t} = D_d \frac{\partial^2 [^3O_2](r,t)}{\partial r^2}. \tag{A8}$$

In this region, we can express the time derivative of the oxygen concentration at each

spatial grid point i as:

$$\frac{d[^3O_2](r,t)}{dt}\bigg|_i = \frac{\partial [^3O_2](r,t)}{\partial r}\bigg|_i \frac{dr'}{dt} + \frac{\partial [^3O_2](r,t)}{\partial t}\bigg|_i \tag{A9}$$

where r' is r-R_s (1). The rate at which each point travels is related to the velocity of the

depletion zone radius front:

$$\frac{dr'/dt}{r'}\bigg|_i = \frac{d\varepsilon/dt}{\varepsilon} \tag{A10}$$

where ε is R_d-R_s. Combining Eqs. A8-A10 we arrive at an expression for the time

derivative of the oxygen concentration that incorporates the movement of the radial grid

elements:

$$\frac{d[^3O_2](r,t)}{dt}\bigg|_i = \frac{\partial [^3O_2](i,t)}{\partial r} \frac{r_i'}{\varepsilon} \frac{d\varepsilon}{dt} + D_d \frac{\partial^2 [^3O_2](r,t)}{\partial r^2}. \tag{A11}$$

References

1.   Murray, W.D. and F. Landis (1959) Numerical and machine solutions of transient heat-conduction problems involving melting or freezing. *J. Heat Transfer* **81**, 106-112.

Appendix B

Time-Step Variation for Analyzing Oxygen Concentration Distributions Containing Photobleaching Information

The algorithm for the analysis of the time-dependent oxygen concentration distributions obtained during irradiation of sensitized spheroids was developed initially for oxygen concentration profiles that were short in duration (~ 40 s). In the numerical solutions of the oxygen diffusion with consumption equations (Eqs. 2.1 and 2.2), the oxygen concentration at a specific radial position at time t is used to predict the oxygen concentration at the same position at time $t+\Delta t$, where Δt is the time-step duration. To follow the rapid changes in oxygen concentration throughout the spheroid during the first 40 to

60 seconds of irradiation, depending on the fluence rate, it is necessary to use time-steps on the order of tens of milliseconds. However, as the photobleaching studies require analysis of oxygen concentration distributions that are recorded over several minutes of irradiation, time and memory requirements make it impossible to analyze such distributions with such short time-steps. Besides, the changes in $^3O_2$ concentration that occur beyond the first few seconds of irradiation are very gradual and can be analyzed using time-steps that are several hundredths seconds long.

Therefore, the duration of each time-step is modified in an exponential fashion as follows:

$$\Delta t = \exp(b*(x-1) + t0),$$

where x is the number of time-steps from the onset of irradiation, and b and $t0$ are constants. For the first time-step, $i.e$, $x=1$, Δt assumes its minimum value, Δt_{min}, specified by the user. This boundary condition determines the value of the constant $t0$. The constant b is determined from the second boundary condition, which prescribes that during the last time-step Δt assumes its maximum value, Δt_{max}, also defined by the user. Thus, we can simulate a 700 second irradiation, for example, with $\Delta t_{min} = 0.05$ s and $\Delta t_{max} = 1.0$ s using approximately 2,200 time-steps, while 14,000 time-steps would be required if a constant 0.05 s step were used.

Appendix C

Dark Toxicity Studies with EtNBS-Sensitized Spheroids

To ensure that the drug incubation protocol that we would follow with the two Nile Blue derivatives, Nile Blue Sulfur (EtNBS) and Nile Blue Selenium (EtNBSe), for the experiments described in this thesis did not have any toxic effects in the absence of irradiation, we performed a series of spheroid cell survival experiments to investigate the dark toxicity of these compounds. The sensitizer incubation protocols that we tested were based on previously reported dark toxicity studies of EtNBS and EtNBSe with EMT6 monolayer cultures (1). Specifically, Cincotta *et al.* examined the dark toxicity of 30 minute incubations with 0.01, 0.05, 0.1, 0.5, and 1.0 μM of both sensitizers. They found that treatment with 0.5 μM EtNBS or EtNBSe was only slightly toxic, resulting in 90%

and 94% viable cells, respectively, while the 1.0 μM incubations were considerably more toxic, leading to 61% and 78% cell survival for EtNBS and EtNBSe, respectively. Additionally, we relied on Photofrin® uptake studies by WiDr spheroids, which indicated that spheroids, 500 μm in diameter, accumulate approximately three times less drug than cells in monolayer culture when treated with similar sensitizer incubation protocols (2). Therefore, we decided to investigate the toxic effects of 30 minute incubations with 0.3, 1.5, and 3 μM EtNBS.

For each experiment, four groups of 50 spheroids, approximately 500 μm in diameter, were handpicked. One of the groups served as a control and was not incubated with drug, while the remaining three groups were treated with either 0.3, 1.5, or 3 μM EtNBS for 30 minutes. At the end of incubation, the spheroids were washed three times with Hank's Balanced Salt Solution and dissociated into single cells in 0.05% trypsin. Following trypsinization, the number of viable cells was counted using a hemacytometer, and a specific number of cells from each treatment group was seeded in quintuplicate to determine the plating efficiency for each population using a colony formation assay. Combining the initial cell recovery data with the plating efficiency information we obtained the overall cell yield for each group. The average cell yield information from 11 experiments is plotted in Figure C.1. Using the equal tails Student's t-test (3), we found that the sensitizer incubation protocols we tested do not result in any significant toxicity when compared to the control group (P < 0.05). Since dark toxicity studies with monolayer cultures indicated that the EtNBSe compound is less toxic than EtNBS (1), we did not perform similar assays with EtNBSe-sensitized spheroids.
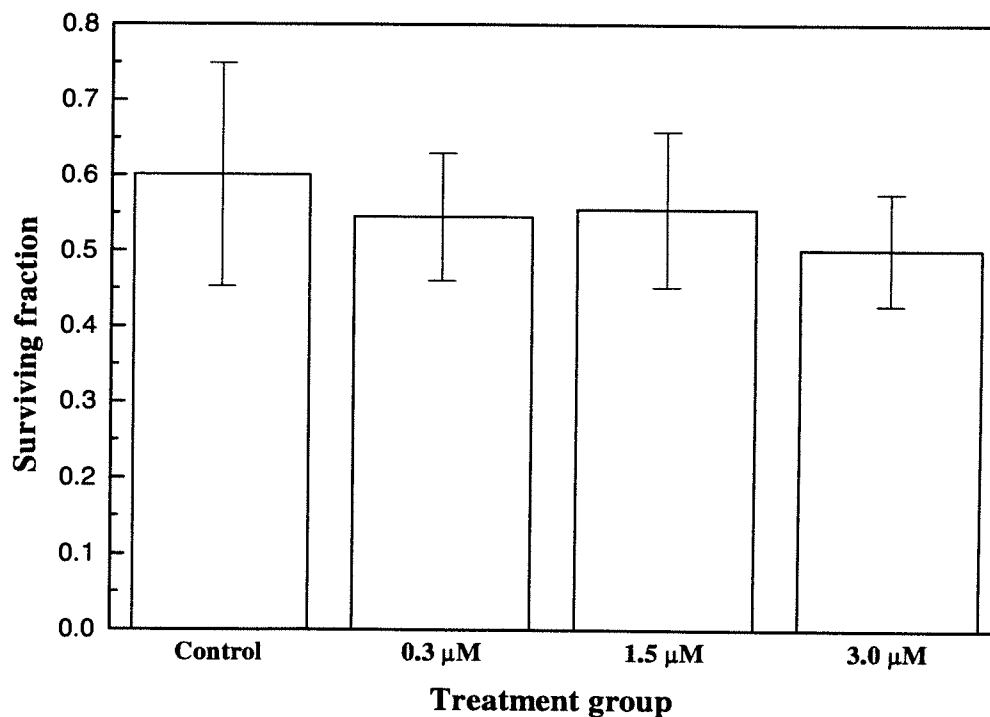
Figure C.1: The overall surviving fractions of spheroid cells treated with 0, 0.3, 1.5, and 3.0 μM EtNBS for 30 min, calculated by multiplying the normalized cell yields and plating efficiencies for each population, are 0.6 ± 0.14, 0.55 ± 0.08, 0.56 ± 0.1, 0.5 ± 0.07, respectively. The sensitizer incubation protocols that we tested do not result in any significant dark toxicity ($P < 0.05$).

References

1.   Cincotta, L., J.W. Foley and A.H. Cincotta (1993) Phototoxicity, redox behavior, and pharmacokinetics of benzophenoxazine analogues in EMT-6 murine sarcoma cells. *Cancer Res.* **53**, 2571-2480.

2.   West, C.M.L. (1989) Size-dependent resistance of human tumour spheroids to photodynamic treatment. *Br. J. Cancer* **59**, 510-514.

3.   Crow, E.L., F.A. Davis and M.W. Maxfield (1960) *Statistics manual.* Dover Publications, Inc., New York, NY.